Bringing classical mechanical resonators towards the quantum regime

A journey on developing integrated optomechanical devices and exploring experiments at high temperature

Guo, J.

DOI
10.4233/uuid:3d240b0f-cf5b-4a63-86a1-c67bc24fe9b5

Publication date
2021

Document Version
Final published version

Citation (APA)
Guo, J. (2021). *Bringing classical mechanical resonators towards the quantum regime: A journey on developing integrated optomechanical devices and exploring experiments at high temperature*. [Dissertation (TU Delft), Delft University of Technology]. https://doi.org/10.4233/uuid:3d240b0f-cf5b-4a63-86a1-c67bc24fe9b5

Bringing classical mechanical resonators towards the quantum regime

A journey on developing integrated optomechanical devices and exploring experiments at high temperature

Bringing classical mechanical resonators towards the quantum regime

A journey on developing integrated optomechanical devices and exploring experiments at high temperature

Dissertation

for the purpose of obtaining the degree of doctor
at Delft University of Technology
by the authority of the Rector Magnificus, Prof.dr.ir. T.H.J.J. van der Hagen,
chair of the Board for Doctorates,
to be defended publicly on
Monday 06 December 2021 at 15:00 o'clock

by

Jingkun GUO

Master of Science in Applied Physics,
Delft University of Technology, the Netherlands,
born in Guangdong, China.

This dissertation has been approved by the promotors.

Composition of the doctoral committee:

Rector Magnificus,	chairperson
Prof.dr. S. Gröblacher,	Delft University of Technology, promotor
Prof.dr.ir. H.S.J. van der Zant	Delft University of Technology, promotor

Independent members:

Prof.dr. Y.M. Blanter	Delft University of Technology
Prof.dr. S. Schmid	Technical University of Vienna
Prof.dr. G.A. Steele	Delft University of Technology
Prof.dr.ir. P.G. Steeneken	Delft University of Technology
Prof.dr. W. Tittel	Delft University of Technology

Keywords: Cavity optomechanics, mechanical resonators, quality factor, feedback cooling, integrated device, coherent feedback

Printed by: Gildeprint

Casimir PhD Series, Delft-Leiden 2021-35
ISBN 978-90-8593-500-1

An electronic version of this dissertation is available at
http://repository.tudelft.nl/.

Contents

Summary

The work in this thesis focuses on potential ways to bring a macroscopic mechanical resonator in a classical environment into the quantum regime with integrated cavity optomechanics.

Chapter 1 introduces the long term goal, bringing a "classical" mechanical resonator into the quantum regime with an integrated optomechanical system. It includes a general overview to cavity optomechanics and integrated structures. It also shows the main challenges (or ways) to achieve the goal, namely, weakening the coupling to the environment and enhancing the interaction between optics and the mechanical resonator. The work in this thesis is focused on tackling these challenges.

Chapter 2 gives a general overview of the related theories. It includes theories in optomechanics, measurements, and the calculation of the mechanical quality factor. It gives a more detailed description of the challenges, and the ways to handle them.

Chapter 3 contains the first attempt on reducing the coupling to the environment while keeping a large optmechanical interaction. A long string with phononic structures and a fishbone-shape geometry is designed and fabricated. Measurement-based feedback cooling is performed to reduce phonon number to around 27 at room temperature.

Chapter 4 describes a novel device fabrication technique that allows a large coupling to the out-of-plane motion of a mechanical resonator. It is used to form on-chip optomechanical system with a mechanical structure having a high-Q out-of-plane fundamental mode. The mechanical mode is cooled to have a phonon number of 22.

Chapter 5 proposes a coherent feedback scheme targeting at the sideband unresolved regime, motivated by realistic integrated devices with macroscopic mechanical resonators. It shows that it is possible to cool the mechanical resonator, and to generate and verify entanglement between the mechanical resonator and photons.

Chapter 6 concludes the thesis. It also includes outlooks, such as potential challenges and solutions, to bring the classical mechanical resonator into the quantum regime.

1

Introduction

1.1. Classical mechanical resonators approaching the quantum regime

The theory of quantum mechanics is one of the most far-reaching developments in physics. It has shown great power in explaining different phenomena of the nature.[1, 2] It also leads to lots of applications, many of which are extremely important in the society today.[3–5] However, though quantum physics is in general a very universal theory, the scale matters in observing and making use of its unique features.[6]

At the same time, mechanical resonators have attracted great interest. They are in general versatile platforms that can be used in many applications, such as acceleration sensing[7–10] which is already in part of our daily life, studying the effect of mass and gravity[11, 12] which is important in understanding the nature, and converting information carrier from one form to another[13–15] which potentially leads to novel future applications. These mechanical resonators and the environment they contact with are usually outside the typical regime where quantum theory is necessarily involved, and thus the "classical" in the title. They are big and heavy, and they consist of innumerable number of atoms. They also have low frequencies, where the characteristic energy scale in quantum mechanics ($\hbar\omega$) is negligible comparing to the thermal energy scale ($k_{\mathrm{B}}T$) in realistic conditions. These issues impose restrictions on their usages.

Bringing a macroscopic mechanical resonators into the quantum regime is thus interesting. Firstly, quantum mechanics gives fundamental limits to the performance of the mechanical resonators, such as the sensitivity[16]. Bringing them into the quantum regime already implies improvements of the performance. Furthermore, the performance limit can sometime be tweaked, such as by introducing squeezing, entanglement or other quantum resources, in a quantum mechanical

way.[17–19][1] Besides sensing, it enables the usage of these mechanical resonators in quantum applications directly, such as in a quantum network[13, 21] and in studying the unknowns in quantum mechanics[11]. In this thesis, much work has been devoted into cooling a mechanical resonator at room temperature. Preparing it very close to the motional quantum ground state where the phonon occupation is below 1, though not achieved within this thesis, marks a first step towards many quantum applications.

1.2. Cavity optomechanics with integrated devices

Having a bare mechanical resonator is not useful without the ability to control and measure. Ideally, the controls and the measurements should be accurate, and the disturbance to the mechanical resonator should be minimized. Coupling the mechanical resonators to photons provides a way to control and measure to a very precise level. A photon carries momentum, which can "kick" the mechanical resonator. Furthermore, photons being used typically have a very high frequency. A widely used frequency in the industry and the laboratory is 200 THz. They are naturally quantum objects due to their energy scale, making them compatible to the goal of exploring quantum mechanics with the "classical" mechanical resonators.

An interesting and widely-used scheme to realize the coupling is to build an optical cavity (cavity optomechanics). With the optical cavity, the interaction is enhanced, and novel phenomena can be introduced by the optical cavity.[22, 23] Ground-breaking experiments have been preformed in such a configuration, including the gravitational wave detection[24]. There are many ways to realize such an optomechanical system,[22] and lots of efforts have been invested on fully integrated structures. They typically allow a very large coupling between photons and a mechanical resonator. They are also easy to operate, a key feature in many practical applications. Thanks to the development of the micro-fabrication techniques, they are also straightforward to be fabricated even at a large scale.

1.3. Challenges

To date, most of the quantum experiments are in a regime where the mass is small, the length scale is small, and the frequency is high. However, a classical mechanical resonator is typically in a different regime with different scales. How to push the macroscopic mechanical resonator towards the quantum regime?

Decoherence is the key.[25] A realistic mechanical resonator cannot be fully isolated. It is an open system and it couples to the environment. However, we have no interest on the environment, it is not possible to take the environment into account either. The crucial part is thus weakening the link between the mechanical resonator and the uninteresting environment. It is then possible to have a "classical" mechanical resonator that is capable to work in the quantum regime. However,

[1] Throughout this thesis, I will in general use "quantum limited" to refer to the applications using only classical methods. The correspondence in optics is, for example, a measurement using the coherent state of light. For "quantum enhanced", I refer to any methods that are tweaked using quantum resources. An example is the use of "N00N state". [18, 20]

no matter how small the interaction with the environment is, decoherence due to the environment eventually happens. We should limit the time of an experiment. Controls and measurements should be finished well before its decoherence. Also, we do not want excess decoherence from the controls and measurements. Therefore, it requires that the controls and measurements to the mechanical resonator should be efficient and precise.

At this point, it worth emphasizing the key requirements of the whole system.

- The coupling to the environment should be weak.
- Controls and measurements should be precise, efficient and fast.

Fulfilling these two requirements is challenging. It makes up a great part of the work in the community[22, 23], including this thesis. Great progress has been made in the recent years. Further improvements, however, are still needed and demanding.

1.4. Outline of this thesis

In this work, I explore ways to tackle the aforementioned challenges, aiming at bringing the "classical" mechanical resonator into the quantum regime with fully integrated optomechanical systems. I acknowledge that it is a big and challenging goal, and continuous efforts are required. Achieving this goal, to any extend, is not the intention of this work. I, however, believe that it is still a step forward.

In chapter 2, I sketch the general theory involved in this work. I address how to quantify the two aforementioned requirements. It also includes the basis of optomechanics, some theories for measurements, and methods in evaluating the dissipation of the mechanical resonator. In chapter 3, I introduce our first generation of devices. They significantly reduce the coupling to the environment. We show a cooling of the mechanical resonator to 27 phonons at room temperature. In chapter 4, I introduce a novel way to fabricate integrated optomechanical device, which potentially allows having a cleaner system while maintaining a low coupling to the environment. We perform cooling again, and achieve a phonon number of 22 at room temperature. This type of system has an issue that many optomechanical protocols are not applicable. In chapter 5, I propose a new experimental scheme which potentially allows using these originally incompatible protocols.

2

Theory and methods

In this chapter I introduce general theories and methods involved in this work. It includes some basis of optomechanics, the ways to evaluate and characterize an optomechanical device, and the calculation of the mechanical dissipation for the structures relevant to this work. The measurement rate and thermal decoherence rate, which are important for enabling an optomechanical system being in a quantum regime, are highlighted. This chapter is intentionally kept concise. For a more detailed discussion, I refer readers to the citations in this chapter. Specific theories and techniques used only in part of the thesis are included in the appendix of the corresponding chapters.

2.1. Cavity optomechanics in the sideband-unresolved regime

In this section, I give a brief introduction to the basis of this work - cavity optomechanics. Especially, I focus on the sideband-unresolved regime, where the mechanical resonance angular frequency (Ω_{M}) is much smaller than the energy decay rate of the optical cavity (κ). More detailed formalism can be found in reference [22, 23]. I follow the two references in this section in general.

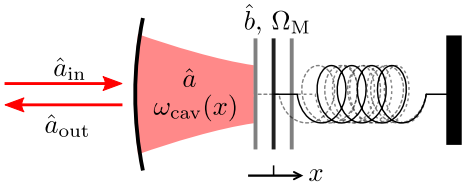

Figure 2.1: A model of cavity optomechanics. It consists of a Fabry-Pérot cavity, with one of the mirror movable. The movable mirror can be modeled as a harmonic oscillator with a resonance frequency Ω_{M}. Its motion modulates the cavity resonance frequency ω_{cav}.

2.1.1. Introduction to optomechanics

An optomechanical system can be modeled as an optical cavity shown 2.1. One of the mirror is movable, with a displacement x. Here, we consider a single-mode cavity, which is a good approximation for this work. The resonance frequency of the optical cavity then depends on the displacement of the movable mirror, $\omega_{\mathrm{cav}}(x)$. Let the creation and annihilation operator for the cavity photon be $\hat{a}^\dagger$ and $\hat{a}$. Also, in this work, it can be more convenient to use the two quadratures of light,

$$\hat{X} = \frac{1}{\sqrt{2}}\left(\hat{a} + \hat{a}^\dagger\right), \qquad \hat{Y} = \frac{1}{\sqrt{2}\mathrm{i}}\left(\hat{a} - \hat{a}^\dagger\right). \tag{2.1}$$

The movable mirror can be treated as a harmonic oscillator in this work since the quality factor of its motion is typically very high. We can formulate the motion in a quantum mechanical way. Denote the mass by m, the resonance frequency by Ω_{M}, and the creation and annihilation operator for the excitation of the mechanical motion (phonon) by $\hat{b}^\dagger$ and $\hat{b}$. It is also possible to write the quadratures for the mechanics

$$\hat{Q} = \frac{1}{\sqrt{2}}\left(\hat{b} + \hat{b}^\dagger\right), \qquad \hat{P} = \frac{1}{\sqrt{2}\mathrm{i}}\left(\hat{b} - \hat{b}^\dagger\right). \tag{2.2}$$

They are related to the displacement ($\hat{x}$) and momentum ($\hat{p}$) through the zero point fluctuation,

$$\hat{x} = \sqrt{2}x_{\mathrm{zpf}}\hat{Q}, \qquad \hat{p} = \sqrt{2}p_{\mathrm{zpf}}\hat{P}, \tag{2.3}$$

where $x_{\mathrm{zpf}} = \sqrt{\frac{\hbar}{2m\Omega_{\mathrm{M}}}}$ and $p_{\mathrm{zpf}} = \sqrt{\frac{\hbar m\Omega_{\mathrm{M}}}{2}}$.

Such an interacting system, neglecting dissipation, has a Hamiltonian

$$\begin{aligned}\hat{H} &= \hbar\omega_{\mathrm{cav}}(\hat{x})\hat{a}^\dagger\hat{a} + \hbar\Omega_{\mathrm{M}}\hat{b}^\dagger\hat{b} \\ &\approx \hbar\omega_{\mathrm{cav}}(x_0)\hat{a}^\dagger\hat{a} + \hbar\Omega_{\mathrm{M}}\hat{b}^\dagger\hat{b} + \hbar G_{\mathrm{OM}}\hat{a}^\dagger\hat{a}\hat{x},\end{aligned} \tag{2.4}$$

where $G_{\mathrm{OM}} = \left.\frac{\partial\omega_{\mathrm{cav}}}{\partial x}\right|_{x_0}$. The last line is from the Taylor expansion of ω_{cav} around the equilibrium position x_0, with only the term linear to $\hat{x}$ kept. Usually, the convention $x_0 = 0$ is chosen. The Hamiltonian highlights the interaction between the optics and the mechanics,

$$H_{\mathrm{int}} = \hbar G_{\mathrm{OM}}\hat{x}\hat{a}^\dagger\hat{a} = \sqrt{2}\hbar g_0\hat{Q}\hat{a}^\dagger\hat{a}. \tag{2.5}$$

Here, a new symbol $g_0 = x_{\mathrm{zpf}}G_{\mathrm{OM}}$ is defined. It has a unit of frequency. For a system where the mechanical oscillator deforms in the oscillation, there are many ways to define the coordinate system. The displacement $\hat{x}$ and the mass m depend on the choice of the coordinate system, and the value of G_{OM} differs in different coordinate systems. However, Q and g_0 are invariant.

Working with the Hamiltonian in equation (2.4) with dissipation is challenging, since it involves nonlinear interaction and very different frequency scales. In the consideration of a practical experiment, the approximations are used.

- The optical frequency is typically very high ($\sim$ 193 THz in this work) comparing to other dynamics in the system. It is thus convenient to move to a frame rotating with the laser frequency ($\omega_{\mathrm{L}}/(2\pi)$). Within this frame, the cavity field oscillates at an angular frequency of $\Delta = \omega_{\mathrm{cav}} - \omega_{\mathrm{L}}$. It is the detuning of the cavity field with respect to the laser field. Within the rotating frame there are counter-rotating terms resonating at $\approx 2\omega_{\mathrm{L}}$, arisen from the coupling between the cavity field and the environment (including the laser drive). These terms are neglected due to their high frequency (rotating wave approximation).[16, 23, 26] Also, we assume that the coupling to the environment is a constant.[16, 23]

- The optical power inside the cavity is typically strong, while the fluctuation of the field is small. For the case in the experiments involved in this thesis, where continuous measurement scheme is used, it is usually a good approximation. It is then possible to separate the constant drive and the fluctuation. Also, any static terms under the continuous optical drive can be neglected since we are only interested in the dynamics. In terms of the interaction Hamiltonian, it becomes

$$\begin{aligned}\hat{H}_{\mathrm{int}} &= \sqrt{2}\hbar g_0\hat{Q}\left(\alpha + \delta\hat{a}^\dagger\right)\left(\alpha + \delta\hat{a}\right) \\ &\to \sqrt{2}\hbar g_0\alpha\hat{Q}\left(\delta\hat{a} + \delta\hat{a}^\dagger\right) = 2\hbar g\hat{Q}\delta\hat{X}.\end{aligned} \tag{2.6}$$

  where $g = \alpha g_0 = \sqrt{n_{\mathrm{cav}}}g_0$ is the interaction enhanced by the cavity photon number (n_{cav}), and α is the classical amplitude of the cavity fields. In this equation, the phase convention is chosen such that α is real and positive. Also, the equilibrium position of the mechanical oscillator is set to 0. Higher order terms of the fluctuations are truncated due to the assumption of small fluctuation.

From these two assumptions plus the dissipation, it is possible to get the linearized Langevin equation in cavity optomechanics. The full derivation is not of the focus in this thesis, but the result forms the basis of this work. Here I present the final result,

$$\begin{aligned}
\delta\dot{\hat{X}} &= -\frac{\kappa}{2}\delta\hat{X} - \Delta\delta\hat{Y} + \sqrt{\kappa_\mathrm{e}}\delta\hat{X}_\mathrm{inc} + \sqrt{\kappa_\mathrm{i}}\hat{X}_\mathrm{in2},\\
\delta\dot{\hat{Y}} &= \Delta\delta\hat{X} - \frac{\kappa}{2}\delta\hat{Y} - 2g\hat{Q} + \sqrt{\kappa_\mathrm{e}}\delta\hat{Y}_\mathrm{inc} + \sqrt{\kappa_\mathrm{i}}\hat{Y}_\mathrm{in2},\\
\dot{\hat{Q}} &= \Omega_\mathrm{M}\hat{P},\\
\dot{\hat{P}} &= -\Gamma_\mathrm{M}\hat{P} - \Omega_\mathrm{M}\hat{Q} - 2g\delta\hat{X} + \sqrt{2\Gamma_\mathrm{M}}\hat{P}_\mathrm{in}.
\end{aligned} \tag{2.7}$$

The subscript inc is for the input coupling. In experiments, it is done by putting a waveguide close to the optical cavity with a coupling rate κ_e. κ_i is the internal energy dissipation rate. This can be due to the scattering or material absorption. This loss channel couples to a vacuum field $\hat{a}_\mathrm{in2}$. They give the total cavity energy decay rate $\kappa = \kappa_\mathrm{i} + \kappa_\mathrm{e}$. The last two equations give the evolution of the mechanical resonator, with Γ_M defined as the mechanical energy dissipation rate. P_in is the thermal input to the mechanical resonator. The treatments for the inputs will be described in section 2.1.3. Note that the two equations for the optical fields $\delta\hat{X}$, $\delta\hat{Y}$ are symmetric asides from the coupling to the mechanics. This is a direct consequence of the rotating wave approximation. It is however not applicable to the mechanical resonator in this work.

In this work, measurement with continuous wave is performed, where the system is typically at a stationary state. It is more convenient to move to the Fourier domain. The Langevin equations can be written as

$$\begin{aligned}
\left(\frac{\kappa}{2} - \mathrm{i}\omega\right)\delta\hat{X}(\omega) + \Delta\delta\hat{Y}(\omega) &= \sqrt{\kappa_\mathrm{e}}\delta\hat{X}_\mathrm{inc}(\omega) + \sqrt{\kappa_\mathrm{i}}\hat{X}_\mathrm{in2}(\omega),\\
-\Delta\delta\hat{X}(\omega) + \left(\frac{\kappa}{2} - \mathrm{i}\omega\right)\delta\hat{Y}(\omega) &= -2g\hat{Q}(\omega) + \sqrt{\kappa_\mathrm{e}}\delta\hat{Y}_\mathrm{inc} + \sqrt{\kappa_\mathrm{i}}\hat{Y}_\mathrm{in2},\\
\hat{Q}(\omega) &= \chi_\mathrm{M}(\omega)(-2g\delta\hat{X}(\omega) + \sqrt{2\Gamma_\mathrm{M}}\hat{P}_\mathrm{in}),
\end{aligned} \tag{2.8}$$

where

$$\chi_\mathrm{M}(\omega) = \Omega_\mathrm{M}/\left((\omega^2 - \Omega_\mathrm{M}^2) - \mathrm{i}\Gamma_\mathrm{M}\omega\right) \tag{2.9}$$

is the mechanical susceptibility.

In the above scheme, the fluctuation of the cavity field should be much smaller than its steady-state amplitude. However, in this work, this does not always satisfy. It is due to the large thermal fluctuation of the mechanical resonator, which introduces a large modulation to the cavity field. It is sufficient to see this in the classical regime. Consider a cavity in the deep sideband-unresolved regime, the cavity field follows the displacement of the mechanics,

$$\langle\hat{a}\rangle = \frac{\sqrt{\kappa_\mathrm{e}}\langle\hat{a}_\mathrm{in}\rangle}{\kappa/2 - \mathrm{i}\left(\Delta + G_\mathrm{OM}\langle\hat{x}\rangle\right)}. \tag{2.10}$$

The equation is nonlinear in $\langle\hat{x}\rangle$. The steady-state amplitude

$$\alpha = \frac{\sqrt{\kappa_e}\alpha_{in}}{\kappa/2 - i\Delta}. \tag{2.11}$$

Clearly, the small fluctuation condition $|\langle\delta\hat{a}\rangle| = |\langle\hat{a}\rangle - \alpha| \ll \alpha$ is satisfied if and only if

$$G_{OM}^2 x^2 \ll (\kappa/2)^2 + \Delta^2. \tag{2.12}$$

In chapter 3, this condition is not strictly satisfied. Nevertheless, it enters this regime with a proper cooling of the mechanical modes, which reduces x.

2.1.2. Input-output formalism and optical loss

Within the rotation wave approximation and assuming that the coupling strength to the environment is a constant (see section 2.1.1), the output optical field from the optical cavity is given by[16, 26]

$$\hat{a}_{out} = \hat{a}_{in} - \sqrt{\kappa_e}\hat{a}. \tag{2.13}$$

In the optical path, the optical photons suffer from losses. Any losses can be formalized by a beam splitter, with another channel coupling to a vacuum field. For a lossy optical channel with transmission efficiency η, input field $\hat{a}_{in}$ and output field $\hat{a}_{out}$[23]

$$\hat{a}_{out} = \sqrt{\eta}\hat{a}_{in} + \sqrt{1-\eta}\hat{a}_{vac}, \tag{2.14}$$

where $\hat{a}_{vac}$ is the vacuum input noise.

2.1.3. Optical vacuum noise and mechanical thermal noise

In this work, optical photons with a frequency of around 193 THz is used. A photon has an energy much higher than the thermal energy. Therefore, the bath (vacuum) is effectively at a coherent state $|0\rangle$. Write $\hat{u}_L = (\hat{X}\ \hat{Y})^T$,

$$\begin{aligned}\left[\hat{u}_L(t), \hat{u}_L^T(t')\right] &:= \hat{u}(t)\hat{u}^T(t') - \left(\hat{u}(t')\hat{u}^T(t)\right)^T = i\Omega\delta(t-t'),\\ \left\langle\left\{\hat{u}_L(t), \hat{u}_L^T(t')\right\}\right\rangle &:= \left\langle\hat{u}(t)\hat{u}^T(t') + \left(\hat{u}(t')\hat{u}^T(t)\right)^T\right\rangle = I\delta(t-t').\end{aligned} \tag{2.15}$$

I is a 2×2 identity matrix and

$$\Omega = \begin{pmatrix} 0 & 1 \\ -1 & 0 \end{pmatrix}. \tag{2.16}$$

For the stationary state, the power spectral density for an arbitrary operator $\hat{O}$ can be written as the Fourier transform of its correlation,

$$S_{\hat{O}\hat{O}}(\omega) = \int d\tilde{t} e^{i\omega\tilde{t}} \left\langle\hat{O}^\dagger(t+\tilde{t})\hat{O}(t)\right\rangle_{t=0}. \tag{2.17}$$

For the optics, it is immediately that

$$S_{\hat{X}_{in}\hat{X}_{in}}(\omega) = S_{\hat{Y}_{in}\hat{Y}_{in}}(\omega) = 1. \tag{2.18}$$

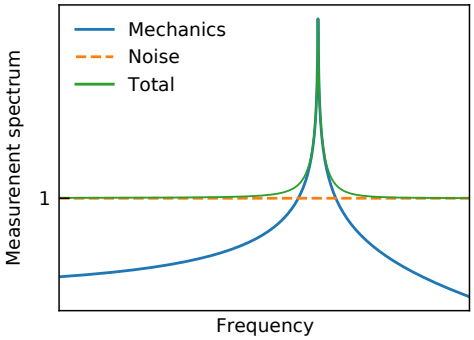

Figure 2.2: A typical spectrum for optomechanics. The measured signal is the signal of the noises and the signal from the mechanical resonator. Ideally, the noise is the optical shot noise and it has a spectrum $S_Y(\omega) = 1$. Any classical noise would lead to a higher noise floor. The axes labels are intentionally since it is a general sketch. The axes are in log scale.

It is more complicated for a mechanical system. As pointed out in equations 2.7, the equations for $\hat{P}$ and $\hat{Q}$ are not symmetric. Especially, the input noise only couples to $\hat{P}$. This term directly relates to the force. For a thermal bath at low frequency, the force, or the input noise P_{in}, is not Markovian, namely, the correlation function is not a delta function. The correlation has a decay time scale $\hbar/(k_{\text{B}}T)$.[23] However, for a typical experimental condition, $\hbar/(k_{\text{B}}T) \sim 10^{-14}$ s (at room temperature) is much smaller than all the dynamics. It can still be treated as a memory-less system,

$$\langle\{\hat{P}_{\text{in}}(t), \hat{P}_{\text{in}}(t')\}\rangle = (2n_{\text{th}} + 1)\delta(t - t'). \tag{2.19}$$

$n_{\text{th}} \approx \frac{k_{\text{B}}T}{\hbar\Omega_{\text{M}}}$ is the thermal phonon occupation of the bath. Another important thing to note is that, in general,

$$[\hat{P}_{\text{in}}(t), \hat{P}_{\text{in}}(t')] \neq 0 \tag{2.20}$$

It can be understood by considering a harmonic oscillator. After $n/2 + 1/4$ ($n = 0, 1, 2, ...$) oscillation periods, the P quadrature becomes Q and it does not commute with the previous Q. Hence, the correlation function of a single quadrature is not a delta function, and the power spectrum density is not flat. A more detailed analysis shows that[23, 27]

$$\begin{aligned} S_{\hat{P}_{\text{in}}\hat{P}_{\text{in}}}(\omega) &\approx n_{\text{th}} + 1 \ (\omega > 0), \\ S_{\hat{P}_{\text{in}}\hat{P}_{\text{in}}}(\omega) &\approx n_{\text{th}} \ (\omega < 0), \end{aligned} \tag{2.21}$$

where $n_{\text{th}} \approx \frac{k_{\text{B}}T}{\hbar\Omega_{\text{M}}}$. In this work, only single-side spectrum of a mechanical resonator contacting a hot thermal bath ($n_{\text{th}} \gg 1$) is measured. Thus, it is in general sufficient to consider a flat, single-side spectral,

$$S_{\hat{P}_{\text{in}}}(\omega) = S_{\hat{P}_{\text{in}}\hat{P}_{\text{in}}}(\omega) + S_{\hat{P}_{\text{in}}\hat{P}_{\text{in}}}(-\omega) = 2n_{\text{th}} + 1. \tag{2.22}$$

Combining the vacuum noise and the mechanical displacement noise, an illustration of the measured optical spectrum is shown in figure 2.2.

2.1.4. Thermal decoherence and the quantum regime

In this part, I introduce an important parameter for the mechanical resonator at high temperature, $Q_{\mathrm{M}} \times f_{\mathrm{M}}$, the mechanical quality factor times the frequency. It concerns the intrinsic property of the mechanical resonator, and thus I neglect the optical cavity in this part.

Consider that a harmonic oscillator interacts with a bath at high temperature, namely, $n_{\mathrm{th}} \gg 1$. It has a thermal decoherence rate

$$\Gamma_{\mathrm{th}} \approx n_{\mathrm{th}} \Gamma_{\mathrm{M}}. \tag{2.23}$$

It characterizes the strength that the mechanical resonator couples to the environment. It defines the time scale adding one extra phonon to the mechanical resonator when it is at the ground state.[23] For a typical optomechanical experiment, the interaction time is long comparing to the oscillation period of the mechanical resonator.[1] It is then especially important for quantum optomechanics experiments that the thermal decoherence rate should be much smaller than the oscillation frequency, $n_{\mathrm{th}} \Gamma_{\mathrm{th}} \ll f_{\mathrm{M}}$. It then follows immediately that

$$Q_{\mathrm{M}} f_{\mathrm{M}} \gg \frac{k_{\mathrm{B}} T}{\hbar} \tag{2.24}$$

is in general required for quantum optomechanics. It highlights the importantness for improving the mechanical quality factor, which is described in section 2.2.

2.1.5. Continuous measurement of mechanical resonator with shot-noise limited detection

In section 2.1.3, shot-noise limited measurement is introduced. With this, it is straight forward to understand another figure of merit in cavity optomechanics, namely the quantum cooperativity $C_{\mathrm{qu}} = 4\frac{g^2}{\kappa \Gamma n_{\mathrm{th}}}$. This value is widely used in this thesis to evaluate the performance of a design. Here, I take a heuristic approach, which is sufficient to understand the idea behind this.

Consider a measurement with zero laser detuning $\Delta = 0$ and a total detection efficiency η. The mechanical resonator has a high quality factor. This is a typical situation for this work, and more general, for the optomechanical system in the deep sideband-unresolved regime. From equation (2.7), the information of the mechanical displacement imprints onto the Y quadrature of the light $\delta\hat{Y} \approx -\frac{4g}{\kappa}\hat{Q}$. Typically, a homodyne measurement is used to measure the Y quadrature of the light. The measured signal is then $\hat{Y}_{\mathrm{meas}} \approx 4\sqrt{\frac{\eta}{\kappa}} g \hat{Q}$. The optical vacuum noise is neglected temporary. Note that the ratio $\kappa_{\mathrm{e}}/\kappa$ is the equivalent to efficiency the light couples back to the input channel. In the scheme in this work, only this part of light will be measured. Hence, it can be absorbed into the total efficiency η. For the

[1] There are proposals and experiments with ultra-short pulses and projection measurements.[28–31] They typically only need a total interaction time around the mechanical resonance period. However, they are not considered in this work.

mechanical resonator at the ground state, the measured signal $\delta Y^2_{\mathrm{meas}}\big|_{\mathrm{zpf}} = 8\frac{\eta}{\kappa}g^2$. Now, take the noise into account. With an ideal detection only limited by the optical shot noise, the power spectrum of the measured Y quadrature has a noise floor $S_Y(\omega) = 1$. With an integration time of $\tau \sim \frac{\kappa}{\eta g^2}$, a unity signal-to-noise ratio (SNR) is achieved. It is then straightforward to define a measurement rate[32], characterizing the rate at which the zero-point fluctuation can be resolved,

$$\Gamma_{\mathrm{det}} = 4\eta\frac{g^2}{\kappa}. \tag{2.25}$$

This can be used to compare with the thermal decoherence rate, $\Gamma_{\mathrm{th}} = n_{\mathrm{th}}\Gamma_{\mathrm{M}}$. The comparison gives a ratio,

$$\frac{\Gamma_{\mathrm{det}}}{\Gamma_{\mathrm{th}}} = 4\eta\frac{g^2}{\kappa\Gamma_{\mathrm{M}}n_{\mathrm{th}}}. \tag{2.26}$$

It is desirable for the ratio to be larger than 1, namely, the zero-point fluctuation can be resolved before the thermal decoherence. By letting $\eta = 1$ it is exactly the quantum cooperativity C_{qu}.

It is important to note that, although the arguments above consider only the situation in the deep sideband-unresolved regime, C_{qu} is important for a general optomechanical system aiming at quantum phenomenon since it compares the strength of the coupling to the losses in the system. For example, the measurement rate in equation (2.25) corresponds to the entanglement generation rate and the state swap rate for an optomechanical system with a properly detuned laser.[33] The thermal decoherence rate is unchanged in different regimes.

2.1.6. Optical spring effect, the determination of optomechanical coupling, and a first step to feedback

An immediate classical effect resulting from the dynamics of optomechanics is the optical spring effect. When the input light is a continuous static light, the resonance frequency and the damping rate is modified to be an effective frequency and damping rate.

For a continuous drive, it is more easy to work in the Fourier domain. Consider equations (2.8) and neglect the quantum fluctuation terms. Plug the second equation to the first to get δX, and then substitute it into Q

$$\begin{aligned}\delta X &= \frac{-2g\Delta Q}{(\kappa/2 - \mathrm{i}\omega)^2 + \Delta^2},\\ Q &= \chi_{\mathrm{M}}(\omega)\left(\frac{-4g^2\Delta Q}{(\kappa/2 - \mathrm{i}\omega)^2 + \Delta^2} + \sqrt{2\Gamma}P_{\mathrm{in}}\right).\end{aligned} \tag{2.27}$$

It is then possible to define an effective susceptibility

$$\chi_{\mathrm{eff}}(\omega) = \left(\frac{1}{\chi_{\mathrm{M}}(\omega)} + \frac{4g^2\Delta}{(\kappa/2 - \mathrm{i}\omega)^2 + \Delta^2}\right)^{-1} \tag{2.28}$$

to highlight that the optical input modifies the dynamics when the detuning is non-zero,

$$Q(\omega) = \chi_{\mathrm{M}}^{\mathrm{eff}}(\omega)\sqrt{2\Gamma}P_{\mathrm{in}}(\omega). \tag{2.29}$$

The effective susceptibility modifies the resonance frequency and the damping. To see this, compare the effective susceptibility to the susceptibility of a bare mechanical system (equation (2.9)),

$$\begin{aligned}\frac{1}{\chi_{\mathrm{M}}^{\mathrm{eff}}} &= \frac{(\Omega_{\mathrm{M}}^2-\omega^2)-\mathrm{i}\Gamma_{\mathrm{M}}\omega}{\Omega_{\mathrm{M}}} + \frac{4g^2\Delta}{(\kappa/2-\mathrm{i}\omega)^2+\Delta^2} \\ &\approx \frac{1}{\Omega_{\mathrm{M}}}\left(\left(\Omega_{\mathrm{M}}+\frac{2g^2\Delta}{(\kappa/2)^2+\Delta^2}\right)^2 - \omega^2 - \mathrm{i}\left(\Gamma_{\mathrm{M}} - \frac{4g^2\Omega_{\mathrm{M}}\kappa\Delta}{((\kappa/2)^2+\Delta^2)^2}\right)\omega\right) \\ &= \frac{1}{\Omega_{\mathrm{M}}}\left(\tilde{\Omega}_{\mathrm{M}}^2-\omega^2-\mathrm{i}\tilde{\Gamma}_{\mathrm{M}}\omega\right).\end{aligned} \tag{2.30}$$

In the last approximation, it is assumed that κ and Δ are much larger than other frequencies. It is a good approximation in this work, where the optomechanical system is in the sideband-unresolved regime. It is clear that the light changes the mechanical frequency and damping rate,

$$\begin{aligned}\delta\Omega_{\mathrm{M}} &= \tilde{\Omega}_{\mathrm{M}} - \Omega_{\mathrm{M}} = \frac{2g^2\Delta}{(\kappa/2)^2+\Delta^2}, \\ \delta\Gamma_{\mathrm{M}} &= \tilde{\Gamma}_{\mathrm{M}} - \Gamma_{\mathrm{M}} = \frac{-4g^2\Omega_{\mathrm{M}}\kappa\Delta}{((\kappa/2)^2+\Delta^2)^2}.\end{aligned} \tag{2.31}$$

It is illustrative to see how large the frequency and the damping rate change. In the experiment condition, κ and Δ is much larger than any other dynamics. To have a biggest effect, $\Delta \sim \kappa$.[2] In a typical experiment condition in this work, $\kappa/(2\pi) \sim 10$ GHz, $g/(2\pi) \sim 1$ MHz, $\Omega/(2\pi) \sim 1$ MHz. Then, $\delta\Omega_{\mathrm{M}}/(2\pi) \sim 10^2$ Hz. Though it is much smaller than the mechanical resonance frequency, this frequency shift is easy to measure in an experiment, and thus it is used to determine the light-enhanced optomechanical coupling g for the device. By a properly calibration of the experimental setup, through which the input power is determined, it is then straight forward to obtain g_0. The shift of the damping rate $\delta\Gamma/(2\pi) \sim 10^{-2}$ Hz is however small. Resolving this small value is in general challenging as it requires a measurement of a large time scale.

This is a typical feature for a sideband-unresolved system, where the optomechanical cooling or heating is weak. Intuitively, the optical spring effect can be understood in a feedback picture. The mechanical displacement Q modulates the resonance frequency of the optical cavity. When the detuning is non-zero, it modulates the light intensity inside the optical cavity, and the modulation feeds back to the mechanical resonator by radiation pressure. For a system in the deep sideband-unresolved regime, the feedback acts almost instantaneously without any phase

[2] For $|\delta\Omega_{\mathrm{M}}|$, the maximum is at $\Delta = \pm\kappa/2$. For $|\delta\Gamma_{\mathrm{M}}|$, it is $\pm\frac{\kappa}{2\sqrt{3}}$.

shift. It effectively modifies the spring constant of the mechancial system and hence it shifts the mechanical frequency. However, the damping force is proportional to $\dot{Q}$ and it should be out-of-phase to the displacement. Since the feedback provided by the optical cavity has almost zero phase shift, the change of the damping is small.

The small extra damping rate provided by the optical cavity eliminates the possibility of cooling the mechanical resonator to a low phonon occupation state, which is the central focus in this work. In chapter 3, a phase shift is provided by a classical controller. In chapter 5, a phase shift is proposed to be provided by some extra linear optical components. Both make it possible to have an efficient cooling of the mechanical resonator.

Although it is impossible to perform significant optical cooling purely with the optical cavity in the sideband-unresolved limit, the change of the damping is still comparable to the intrinsic damping rate of the high-Q mechanical resonator in this work. It is thus still possible that the change of the damping rate brings the system into an unstable regime ($\Gamma_{\mathrm{M}} + \delta\Gamma < 0$). Continuous measurement with a blue-detuned laser, where the optical spring effect heats the mechanical motion, is in general avoided.

2.1.7. Quadrature measurement with homodyne detection

A scheme of homodyne detection is sketched in figure 2.3. The light from the laser is split into two arms. One arm is the signal arm. The light interacts with the device and the output light carries information from the device. Another arm is the local oscillator (LO) arm, with a relative phase shift ϕ to the signal beam. Both arms merge at the second beam splitter. The outputs from both ports of the second beam splitter are measured. Then, the difference between the two measurement outputs is obtained. In the measurement, the first beam splitter typically has a splitting ratio such that the power on the LO arm is much stronger than the power on the signal arm. The splitting ratio of the second beam splitter is 50:50 (balanced homodyne detection).

Consider that the output from the device is $\hat{a}_{\mathrm{sig}}$, and the local oscillator is $\hat{a}_{\mathrm{LO}}$. Without loss of generality, let the relative phase shift introduce by the second beam splitter be 0. Any relative phase shift can be absorbed into ϕ. Let the transmission of the second beam splitter be T, the two outputs [34]

$$\begin{aligned} \hat{a}_1 &= \sqrt{T}\hat{a}_{\mathrm{sig}} + \sqrt{1-T}\hat{a}_{\mathrm{LO}}, \\ \hat{a}_2 &= -\sqrt{1-T}a_{\mathrm{sig}} + \sqrt{T}\hat{a}_{\mathrm{LO}}. \end{aligned} \tag{2.32}$$

Then, the photon current of the outputs of the second beam splitter

$$\begin{aligned} \langle \hat{a}_1^\dagger \hat{a}_1 \rangle &= T\langle \hat{a}_{\mathrm{sig}}^\dagger \hat{a}_{\mathrm{sig}} \rangle + (1-T)\langle \hat{a}_{\mathrm{LO}}^\dagger \hat{a}_{\mathrm{LO}} \rangle + \sqrt{T(1-T)}\langle \hat{a}_{\mathrm{sig}}^\dagger \hat{a}_{\mathrm{LO}} + \hat{a}_{\mathrm{LO}}^\dagger \hat{a}_{\mathrm{sig}} \rangle, \\ \langle \hat{a}_2^\dagger \hat{a}_2 \rangle &= (1-T)\langle \hat{a}_{\mathrm{sig}}^\dagger \hat{a}_{\mathrm{sig}} \rangle + T\langle \hat{a}_{\mathrm{LO}}^\dagger \hat{a}_{\mathrm{LO}} \rangle - \sqrt{T(1-T)}\langle \hat{a}_{\mathrm{sig}}^\dagger \hat{a}_{\mathrm{LO}} + \hat{a}_{\mathrm{LO}}^\dagger \hat{a}_{\mathrm{sig}} \rangle. \end{aligned} \tag{2.33}$$

It is clear that, for $T = 1/2$, the differential photon current

$$I_- = \langle \hat{a}_1^\dagger \hat{a}_1 \rangle - \langle \hat{a}_2^\dagger \hat{a}_2 \rangle = \langle \hat{a}_{\mathrm{sig}}^\dagger \hat{a}_{\mathrm{LO}} + \hat{a}_{\mathrm{LO}}^\dagger \hat{a}_{\mathrm{sig}} \rangle. \tag{2.34}$$

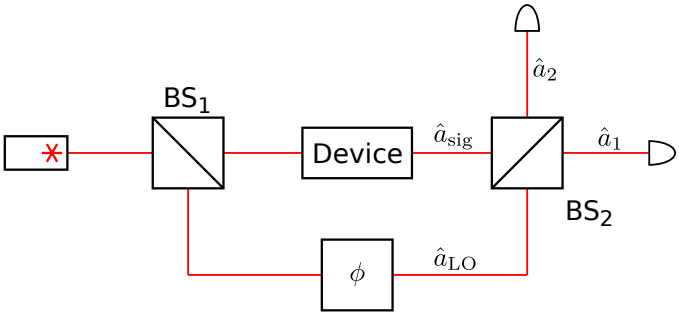

Figure 2.3: Homodyne detection scheme. The light from a single laser is split into two arms. One passes through a device to be measured (signal arm). The other one only experiences a phase shift. They are combined at a beam splitter and then measured by two photodetectors. The final signal is the subtraction of the photocurrent.

For small signals, write the optical field as a constant classical amplitude (α) plus some fluctuation[3],

$$\begin{aligned}\hat{a}_{\mathrm{sig}} &= \alpha_{\mathrm{sig}} + \delta\hat{a}_{\mathrm{sig}},\\ \hat{a}_{\mathrm{LO}} &= \alpha_{\mathrm{LO}} + \delta\hat{a}_{\mathrm{LO}}.\end{aligned} \tag{2.35}$$

Also, adapt the phase convention $\arg\alpha_{\mathrm{sig}} = 0$, $\arg\alpha_{\mathrm{LO}} = \phi$, and consider the typical situation in a homodyne detection, $|\alpha_{\mathrm{LO}}| \gg |\alpha_{\mathrm{sig}}|$. By keeping only the linear term of the fluctuation,

$$I_- \approx 2\alpha_{\mathrm{sig}}|\alpha_{\mathrm{LO}}|\cos\phi + \sqrt{2}|\alpha_{\mathrm{LO}}|\left(\delta X_{\mathrm{sig}}\cos\phi + \delta Y_{\mathrm{sig}}\sin\phi\right). \tag{2.36}$$

The differential photon current is separated into two parts, one is a constant, while the other term contains the signal. By properly tuning the phase ϕ, it is possible to one of the quadratures or their combination. Also, the signal is amplified by the square root of the power on the local oscillator arm. In experiment in this work, Y quadrature of the optical field is measured. This can be done by setting the phase $\phi = \pm\pi/2$. Note that the constant term vanishes. The vanishing constant term can be used to lock the phase ϕ.

2.1.8. Determining overcouple or undercouple

In this work, reflection signal of the optical cavity is measured. For such an optical cavity, the dissipation can be considered to have two loss channels. One is the extrinsic loss, containing all the signal reflected back and it is associated with κ_{e}. The other channel is intrinsic dissipation, including all the dissipation where light is not reflected back and it is associated with κ_{i}. Determining $\kappa_{\mathrm{e}}/\kappa$ is important in this work, since it relates to the total efficiency in a system. Only the reflected signal is measured.

The reflected (classical) amplitude from such a cavity

$$r(\Delta) = 1 - \frac{\kappa_{\mathrm{e}}}{\kappa/2 - \mathrm{i}\Delta}. \tag{2.37}$$

[3]The fluctuation includes the signal we want to measure.

By simplify measuring and fitting the reflectivity,

$$|r(\Delta)|^2 = 1 - \frac{\kappa_e \kappa_i}{(\kappa/2)^2 + \Delta^2}, \tag{2.38}$$

it is possible to get $\kappa_i \kappa_e$ and κ. Combining that $\kappa = \kappa_e + \kappa_i$, two different solutions exist unless the optical cavity is critically coupled ($\kappa_i = \kappa_e$). It is clear that interchanging κ_i and κ_e does not change the reflectivity. To unambiguously determine whether the optical cavity is overcoupled ($\kappa_e > \kappa_i$), I perform phase measurements using the scheme in Figure 2.3. To perform the measurement, the optical path lengths of the two arms are carefully balanced, up to a small offset. The intentional offset will be clear by the end of this part. Similar to the homodyne measurement, the power on the local oscillator arm is much stronger than the power on the signal arm. The second beam splitter has a transmission of about $1/2$. Unlike a balanced homodyne measurement, this splitting ratio does not have to be precise.

Let the optical field after the first beam splitter be α_0 for the LO arm and $\epsilon\alpha_0$ for the signal arm. Since only the intensity is measured eventually, without the loss of generality, I require that α_0 and ϵ are both real and positive. With the power on LO arm being much larger than the power on the signal arm, $\epsilon \ll 1$.

The optical field arriving at the second beam splitter

$$\begin{aligned} \alpha_{sig} &= r(\Delta)\epsilon\alpha_0, \\ \alpha_{LO} &= e^{i(k\delta L + \phi_0)}\alpha_0, \end{aligned} \tag{2.39}$$

where $k = \omega_L/c$ is the wavenumber of the beam, δL is the optical length difference between the signal arm and the LO arm, and ϕ_0 is an additional phase different between the two arms. Let the transmission of the second beam splitter be T, the differential signal gives

$$I_- = (1-2T)\left(1 - |R(\Delta)\epsilon|^2\right)\alpha_0^2 + 4\epsilon\sqrt{T(1-T)}\mathrm{Re}\left(r(\Delta)e^{-i(k\delta L+\phi_0)}\right)\alpha_0^2. \tag{2.40}$$

When detuning is large, $\Delta \gg \kappa$, the reflection from the cavity $r(\Delta) \approx 1$. Also, keep the leading order in ϵ. The difference of the photon flux

$$I_-|_{\Delta\gg\kappa} \approx (1-2T)\alpha_0^2 + 4\epsilon\sqrt{T(1-T)}\cos(k\delta L + \phi)\alpha_0^2. \tag{2.41}$$

Note that k is a function of the detuning. The reflected signal oscillates between $(1-2T)\alpha_0^2 \pm 4\epsilon\sqrt{T(1-T)}\alpha_0^2$, with an oscillation period (free spectral range) of $2\pi c/\delta L$.

In the measurement, a requirement of the length offset is that the free spectral range is large, $2\pi c/\delta L \gg \kappa$. At the vicinity of the resonance ($|\Delta| \ll 2\pi c/\delta L \gg \kappa$), write $\phi_{LO} = k\delta L + \phi_0$ and treat it as a constant,

$$\begin{aligned} I_-\big|_{|\Delta|\ll\frac{2\pi c}{\delta L}} \approx (1-2T)\alpha_0^2 + 4\epsilon\sqrt{T(1-T)}\Bigg(&\left(1 - \frac{\kappa_e\kappa/2}{(\kappa/2)^2+\Delta^2}\right)\cos\phi_{LO} \\ &- \frac{\kappa_e\Delta}{(\kappa/2)^2+\Delta^2}\sin\phi_{LO}\Bigg). \end{aligned} \tag{2.42}$$

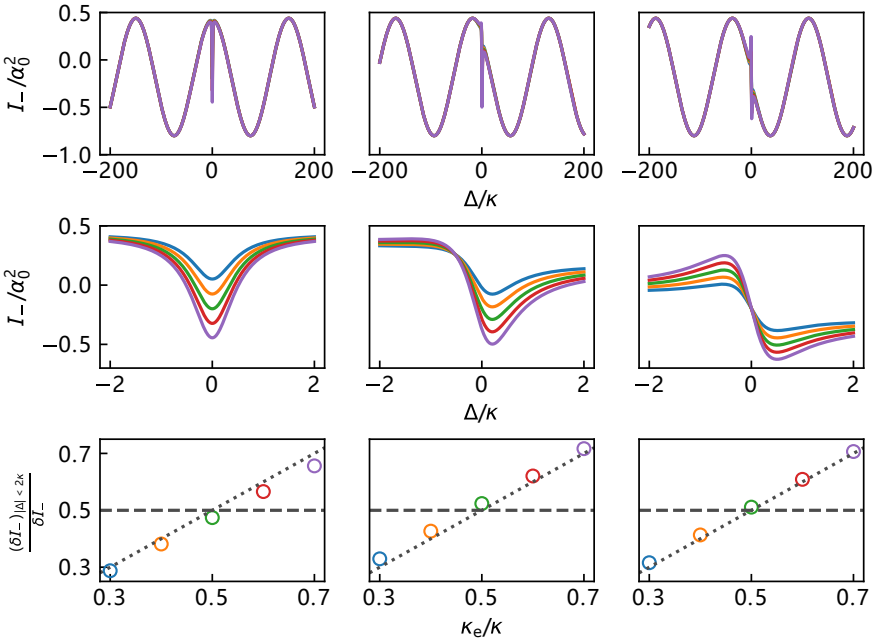

Figure 2.4: Differential photo current in a phase measurement in theory. From left to right: $k_0\delta L+\phi_0 = 0,\ \pi/4, \pi/2$. Different colors show different κ_e, with $\kappa/(2\pi) = 10$ GHz being fixed. The corresponding κ_e/κ can be read from the last column with the same color. From blue to purple the cavity changes from undercouple to overcouple. The second row is a zoom in of the first row, in the vicinity of the resonance. It is clear that it is possible to distinguish over- or under-coupled cavities. The third row plots the difference between the maximum and minimum I_-, with the values obtained from the second row normalized by the values from the first row. For a cavity that is not close to the critical coupling (the typical case in this work), it is easy to distinguish whether it is over- or under-coupled by setting a bound at 0.5. The dotted lines plot $\delta I_-|_{|\Delta|<2\kappa}/\delta I_- = \kappa_e/\kappa$ (see equation (2.44)). A small error is due to the small offset $\delta L \neq 0$. In the calculation, the following parameters are used: resonance frequency $\lambda_{cav} = 1550$ nm, path length imbalance $\delta L = 0.2$ mm, the power ratio between the two arms $\epsilon^2 = 0.1$, transmission of the second beam splitter $T = 0.6$. The splitting ratio of $0.4/0.6$ shows that the scheme does not require a well tuned beam splitter. It makes it compatible with a sweeping over a large frequency range since the splitting ratio is wavelength-dependent for a practical beam splitter.

The extremum is achieved when $\Delta = -\frac{\kappa}{2\sin\phi_{LO}}(\cos\phi_{LO} \pm 1)$.[4] It corresponds to a difference between the maximum and minimum

$$\left(I_-^{max} - I_-^{min}\right)_{|\Delta|\ll\frac{2\pi c}{\delta L}} = 8\epsilon\sqrt{T(1-T)}\frac{\kappa_e}{\kappa}\alpha_0^2. \tag{2.43}$$

It clearly distinguish between κ_e and κ_i. Combining the measurement where $\Delta \gg \kappa$ (equation (2.41)), it is possible to get a response

$$\frac{\left(I_-^{max} - I_-^{min}\right)_{|\Delta|\ll\frac{2\pi c}{\delta L}}}{\left(I_-^{max} - I_-^{min}\right)_{|\Delta|\gg\kappa}} = \frac{\kappa_e}{\kappa}. \tag{2.44}$$

[4]When $\phi_{LO} = 0$, there is a minimum $\Delta = 0$. The maximum occurs at $\Delta \to \infty$.

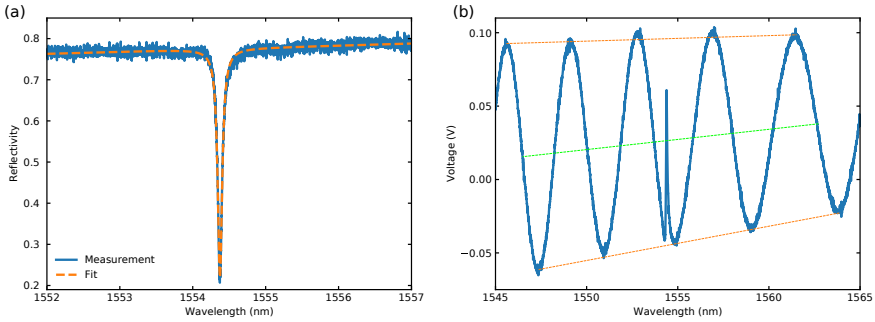

Figure 2.5: An example of measuring the reflection of a device. (a) An intensity measurement. The y axis is normalized to the input power, showing the reflectivity. A fitting shows $\kappa/2\pi = 9.3$ GHz. $\kappa_e/2\pi$ is either 2.2 or 7.1 GHz. (b) A phase measurement. The path length is tuned to have a free spectral range of about 4 nm. The peak is due to the phase response of the cavity. It clearly shows that the device is overcoupled. The orange dashed lines are a guide to the eye to show the background oscillations, and the green dashed line shows the center.

Note that this expression only depends on the ratio κ_e/κ. In a measurement, the two regimes $|\Delta| \gg \kappa$ and $|\Delta| \ll \frac{2\pi c}{\delta L}$ are measured in a same laser scan. The scanning where $|\Delta| \gg \kappa$ is used as a calibration. To get the calibration, the free spectral range $2\pi c/\delta L$ should be smaller than the laser scanning range. Also, to reach the above formula, note that the maximum and minimum of the differential photon flux in this interference scheme are obtained at a detuning of the order of κ, it requires $\kappa \ll \frac{2\pi c}{\delta L}$.[5] For a typical device in this work, $\kappa/(2\pi) \sim 10$ GHz. It corresponds to $\delta L \ll 1$ cm. This can be easily achieved by using a free space setup.

Some example traces obtained from equation (2.40) are plotted in figure 2.4. It is clear that it is possible to distinguish between an overcoupled and an undercoupled optical cavity. For a typical situation in an experiment, equation (2.44) still gives a good approximation. With the typical regime of interest in this work where the cavity is deeply overcoupled, setting a bound of 0.5 is sufficient to distinguish. An example of the measurement is shown in figure 2.5. The two possible κ_e values are first determined by fitting the reflectivity. Then, a phase measurement is performed to pinpoint the κ_e. In this case, a peak due to the cavity is seen. It is then compared to the background oscillations, and it is shown to be overcoupled.

2.2. Mechanical dissipation in high-stress Silicon Nitride

Increasing the $Q_M \times f_M$ product is one of the central focus in this work, as described in section 2.1.4. Typically, I keep the mechanical frequency to be around 1 MHz, a sweet point that it is small enough to fit the feedback cooling experiments, and it is not too low considering the classical noise. The goal is then to reduce the

[5] This is not necessary if a full model is taken into account, but meeting this criteria is not challenging in an experiment and thus I only consider this situation here.

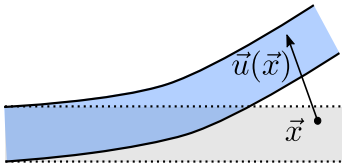

Figure 2.6: An illustration of the deformation of the material. The gray color shows the undeformed structure, while the blue shows the deformed. The small part of the material at spacial coordinate $\vec{x}$ is displaced by $\vec{u}(\vec{x})$.

dissipation of the mechanical resonator. In this work, I focus on high-stress LPCVD grown silicon nitride.

2.2.1. Mechanical damping due to internal damping [6]

Consider a part of the structure shown in figure 2.6. At the static state, the structure is shown in gray. Consider a specific mode. At time t, the displacement field is $\vec{u}(\vec{x})$, where $\vec{x}$ is in the frame of undeformed structure. In the following, I will omit $\vec{x}$ and t when it is clear from the content. The strain of the structure is[35]

$$\epsilon_{ij} = \frac{1}{2}\left(\partial_i u_j + \partial_j u_i + \partial_i u_k \partial_j u_k\right), \tag{2.45}$$

where $\partial_i = \frac{\partial}{\partial x_i}$, and the indices i, j are the components of the spacial vectors. Here, I keep the nonlinear term $\partial_i u_k \partial_j u_k$. We will see that, even for small displacement, it cannot be neglected for the high stress material.

The deformation results in a stress in the material[35]

$$\sigma_{ij} = \sigma_{ij}^{(0)} + \Delta\sigma_{ij} = \sigma_{ij}^{(0)} + \frac{E}{1+\nu}\left(\epsilon_{ij} + \frac{\nu}{1-2\nu}\epsilon_{kk}\delta_{ij}\right), \tag{2.46}$$

where E is the Young's modulus, ν is the Poisson's ratio. The term $\sigma_{ij}^{(0)}$ is due to the fact that there is a static stress in the material.

The quality factor of a mode is given by the elastic energy stored in the structure, divided by the energy dissipation per oscillation. Let the elastic energy density be U_S,

$$\begin{aligned} U_S &= \frac{\Omega_\mathrm{M}}{42\pi}\int_0^{2\pi} \mathrm{d}t \frac{1}{2}\sigma_{ij}(t)\epsilon_{ij}(t) \\ &= \frac{\Omega_\mathrm{M}}{4\pi}\frac{E}{1+\nu}\int_0^{2\pi} \mathrm{d}t \left(\left(\epsilon_{ij}(t)\epsilon_{ij}(t) + \frac{\nu}{1-2\nu}\epsilon_{kk}(t)\epsilon_{ll}(t)\right) + \sigma_{ij}^{(0)}\epsilon_{ij}(t)\right). \end{aligned} \tag{2.47}$$

For high Q oscillations, we can approximate the motion by a simple harmonic oscillator. Write $\vec{u}(t) = \vec{u}\sin(\Omega_\mathrm{M} t)$. Then, all the terms linear to u_i integrate to 0, and the terms quadratic to u is kept. For small oscillations,

$$U_S = \frac{1}{4}\left(\frac{E}{1+\nu}\left(\epsilon_{ij}^{\mathrm{lin}}\epsilon_{ij}^{\mathrm{lin}} + \frac{\nu}{1-2\nu}\epsilon_{kk}^{\mathrm{lin}}\epsilon_{ll}^{\mathrm{lin}}\right) + \sigma_{ij}^{(0)}\partial_i u_k \partial_j u_k\right). \tag{2.48}$$

[6] In this part, the summation convention for the repeated indices applies.

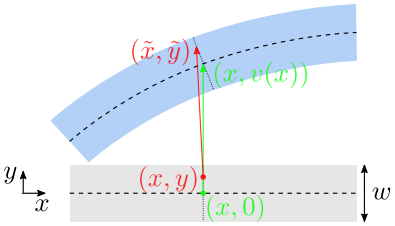

Figure 2.7: An illustration of the motion of a segment of a mechanical beam, moving from the gray part to the light blue part. The dashed line indicates the center of the beam ($y = 0$). The dotted line is perpendicular to the center line, and the elements on the two dotted line are the same.

We see that the nonlinear term appears due to the initial stress. Actually, the internal stress makes silicon nitride out-standing from many other materials in terms of mechanical quality factor at high temperature.[36]

Phenomenologically, the dissipation in the system can be modeled as a complex Young's modulus.[37, 38] Equivalently, it can be written as a phase lag (loss angle[7], ϕ) between the stress and the actual motion. This value has been found to be only weakly dependent on the frequency within the frequency range we are interested in[37], and here I approximate it as a constant.[8] For small oscillation, we again keep terms up to the quadratic for the dissipation density,

$$\begin{aligned} \Delta U &= \int_0^{\frac{2\pi}{\Omega}} \Delta\sigma_{ij}(t)\mathrm{d}\epsilon_{ij}(t) = \int_0^{\frac{2\pi}{\Omega}} \mathrm{d}t\Delta\sigma_{ij}\sin(\Omega t+\phi)\frac{\mathrm{d}}{\mathrm{d}t}\left(\epsilon_{ij}\sin(\Omega t)\right) \\ &= \pi\sin(\phi)\frac{E}{1+\nu}\left(\epsilon_{ij}^{\mathrm{lin}}\epsilon_{ij}^{\mathrm{lin}} + \frac{\nu}{1-2\nu}\epsilon_{kk}^{\mathrm{lin}}\epsilon_{ll}^{\mathrm{lin}}\right). \end{aligned} \tag{2.49}$$

The non-linear term in the strain disappears because it only couples to $\sigma_{ij}^{(0)}$ in the small oscillation limit and it integrates to 0.

Finally, the mechanical quality factor can be obtained by integrating the energy storage and dissipation density,

$$Q_{\mathrm{M}} = \frac{\int \mathrm{d}^3x\Delta U(\vec{x})}{\int \mathrm{d}^3x U_S(\vec{x})}. \tag{2.50}$$

2.2.2. Mechanical quality factor for an Euler-Bernoulli beam

In equations 2.48 and 2.49, I wrote down the formula for the mechanical dissipation and the energy storage for a general structure. They, however, do not immediately give an intuitive picture on how to increase the mechanical quality factor. In this part, I consider a simplified situation. The mechanical resonator is approximated by an Euler-Bernoulli beam, where the beam can be considered as a 1D structure and and Poisson's ratio vanishes. Also, I assume that the cross-section is a rectangle.

[7] Given by the angle of the complex Young's modulus.

[8] This value has found to be different between the region close to the surface and the region deep inside the bulk.[39] In this work, I only consider a uniform loss angle as it is sufficient to explain phenomenon and to design structures with high quality factor.

The stress σ_{ij} is non-zero only if $i = j = 1$ be the x component. In literature, the formulation with this situation was derived earlier than equations 2.48 and 2.49, and it leads to the concepts including bending loss, dissipation dilution, and soft-clamping.[35] Here, I take a different approach, where the scheme for 1D long string is derived from equations 2.48 and 2.49.

Consider a segment of the beam with a width w and thickness h, as sketched in figure 2.7. The mechanical motion is in y direction, and it is uniform across the thickness. For this structure, it is sufficient to consider it in 2 dimensions, since it is uniform across z. Define the coordinate such that $y = 0$ is the center of the undeformed structure. At the center plane, the displacement field is $v(x)$. Then, consider a small element originally located at (x, y). Without any deformation, the line formed by (x, y) and $(x, 0)$ is perpendicular to the center line. With the deformation introduced by the mechanical motion, the two points moves to $(\tilde{x}, \tilde{y})$ and $(x, v(x))$. The line formed by these two points should still be perpendicular to the center, at x. Then,

$$(\tilde{y} - v)v'(x) = -(\tilde{x} - x). \tag{2.51}$$

Further, the distance between these two points remains unchanged,

$$(\tilde{y} - v)^2 + (\tilde{x} - x)^2 = y^2. \tag{2.52}$$

This gives the displacement of the point originally at (x, y),

$$\begin{aligned} u(x, y) &= -\frac{v'(x)}{\sqrt{1 + v'^2(x)}} y, \\ v(x, y) &= \left(\frac{1}{\sqrt{1 + v'^2(x)}} - 1 \right) y + v(x). \end{aligned} \tag{2.53}$$

The displacement v is smooth and small. It is sufficient to keep the terms with the lowest order to the derivative and the smallest exponents. Then, the non-zero terms involved in equations 2.48 and 2.49 are

$$\begin{aligned} \partial_x u_k \partial_x u_k &= v'^2(x), \\ \epsilon_{ij}^{\text{lin}} &= v''^2(x) y^2. \end{aligned} \tag{2.54}$$

The contribution to the first equation is from $k = 2$ (y component), and the contribution to the second equation is from $i = j = 1$ (x component). Substitute them into equations 2.48 and 2.49, and carry out the integral over y and z direction, the line density of the energy storage and dissipation is obtained,

$$\begin{aligned} U_s(x) &= \frac{\sigma_{11}^{(0)}}{4} v'^2(x) w h, \\ \Delta U(x) &= \frac{\pi}{12} \sin(\phi) E v''^2(x) w^3 h. \end{aligned} \tag{2.55}$$

Here, I have also neglected terms that have a higher order in derivative or higher order in its exponent. The expression for U_s is only a good approximation for small oscillations and high stress material. The result matches what has been derived in reference [37] with a different method.

From equation (2.55), it is clear that the energy storage is from the rotation[9] (v') of the structure, and the energy dissipation is from the bending (v'') of the structure. It is interesting to note that the energy dissipation density is proportional to w^3,[10] and that the energy storage is proportional to w. This observation leads to the novel fishbone design in chapter 3.

2.2.3. Simulation

The mechanical quality factor is simulated in COMSOL Multiphysics®. Eigenvalue simulation is used to obtain the mechanical modes, from which the quality factor can be calculated. When working with high stress silicon nitride, extra care needs to be taken.

Firstly, the above formalism is based on introducing the imaginary part of the Young's modulus, and it can be directly implemented in COMSOL. However, COMSOL does not seem to know the "small oscillation" requirement. A typical displacement field simulated from the eigenvalue simulation is of the order of 1 meter. Since the problem is not linear, the above formalism needs to be implemented into COMSOL as a post-processing step.

Next, there is an issue about the frame. In the simulation, an initial geometry with a constant initial stress is first defined. This geometry, and its internal stress, are not the actual geometry and stress distribution for a fully suspended structure. These are obtained by doing a steady state simulation. For a physical device, this step corresponds to the release of the structure. After this, the stress would be redistributed, and the geometry would deform. The mechanical modes, and the corresponding eigenvalue simulations, are on the deformed structure. To properly calculate the energy dissipation and energy storage in equations (2.48) and (2.49), the coordinate should correspond to a deformed structure. In COMSOL, it does not know the change of the frame.

Consider a small element initially centered at $x_i^{(0)}$ with a volume $\mathrm{d}^3x^{(0)}$. It is also the coordinate of all the elements in COMSOL. Then, after the "release" step, this small element moves to a new coordinate

$$x_i = x_i^{(0)} + u_i^{(r)}\left(\vec{x}^{(0)}\right). \tag{2.56}$$

Note that the displacement $u^{(r)}$ in this step is position-dependent. Without specifying, I will always use the original coordinate for the argument of the displacement. Then, for a small displacement introduced in this step, equations (2.48) and (2.49)

[9] More precisely, from the elongation resulting from the rotation.

[10] Strictly speaking, the cubic dependency only valid when the loss angle is uniform across the material. For high stress LPCVD silicon nitride, it might deviate noticeably for structure with dimension smaller than 100 nm.

can be evaluated in COMSOL by the geometry transformation,

$$\frac{\partial x_i^{(0)}}{\partial x_j} = \delta_{ij} - \frac{\partial u_i^{(r)}}{\partial x_j^{(0)}},$$
$$\partial_i u_j = \frac{\partial u_j(\vec{x})}{\partial x_i} = \frac{\partial u_j(\vec{x}^{(0)})}{\partial x_k^{(0)}} \frac{\partial x_k^{(0)}}{\partial x_j} = \frac{\partial u_j(\vec{x}^{(0)})}{\partial x_k^{(0)}} \left(\delta_{ki} - \frac{\partial u_k^{(r)}}{\partial x_i^{(0)}} \right). \tag{2.57}$$

u is the displacement for the oscillations. On the last equation, I make use of the fact that the element on $\vec{x}^{(0)}$ and the one on $\vec{x}$ are the same element. Hence, I can replace $u_j(\vec{x})$ by $u_j(\vec{x}^{(0)})$. Substitute it into equations (2.48) and (2.49), it gives the energy density that can be evaluated in COMSOL. Regarding to the final integral in equation (2.50), the volume is changed by the determinant of a Jacobian matrix, $\mathrm{d}^3x = \left| \frac{\partial \vec{x}}{\partial \vec{x}^{(0)}} \right| \mathrm{d}^3x^{(0)}$. The matrix elements are given by

$$\left(\frac{\partial \vec{x}}{\partial \vec{x}^{(0)}} \right)_{i,j} = \frac{\partial x_i}{\partial x_j^{(0)}}. \tag{2.58}$$

It would result in a lengthy expression. A python script is written to generate the expression for COMSOL.

3

Feedback cooling of a room temperature mechanical oscillator close to its motional groundstate

Preparing mechanical systems in their lowest possible entropy state, the quantum groundstate, starting from a room temperature environment is a key challenge in quantum optomechanics. This would not only enable creating quantum states of truly macroscopic systems, but at the same time also lay the groundwork for a new generation of quantum limited mechanical sensors in ambient environments. Laser cooling of optomechanical devices using the radiation pressure force combined with cryogenic pre-cooling has been successful at demonstrating groundstate preparation of various devices, while a similar demonstration starting from a room temperature environment remains an outstanding goal. Here we combine integrated nanophotonics with phononic bandgap engineering to simultaneously overcome prior limitations in the isolation from the surrounding environment, the achievable mechanical frequencies, as well as limited optomechanical coupling strength, demonstrating a single-photon cooperativity of 200. This new microchip technology allows us to feedback cool a mechanical resonator to around 1 mK, near its motional groundstate, from room temperature. Our experiment marks a major step towards accessible, widespread quantum technologies with mechanical resonators, operating in ambient environments.

Part of this chapter has been published in Physical Review Letters **22**, 223602 (2019) [40].

3.1. Introduction

The last decade has seen immense progress on observing quantum effects with microfabricated mechanical oscillators [41–46]. This is not only of significant interest for understanding the fundamental aspects of quantum physics in macroscopic objects, but also for the potential of using mechanical systems for quantum information processing tasks and as novel quantum sensors [47]. Excess classical (i.e. thermal) noise typically obscures the quantum features of these devices, thus limiting their usefulness and practical adoption for quantum limited sensing. Groundstate cooling can alleviate this problem, but so far has only been possible by pre-cooling the devices using cryogenic methods [48–52]. The main limitations preventing to reach this regime from room temperature include insufficient isolation from the surrounding environment and too low mechanical frequencies, which can be formulated into the condition of the product of the mechanical frequency and its quality factor $f_{\mathrm{M}} \cdot Q_{\mathrm{M}} \geq 6 \times 10^{12}$ [53]. In addition, the optomechanical coupling rate g_0 also plays a dominant role in the ability to efficiently laser cool the motion of a resonator. There are several approaches focusing on overcoming these limitations. In particular, experiments featuring optically levitated nanospheres have come to within a few thermal phonons of the mechanical groundstate recently [54–57]. While the absence of any physical attachment to the environment allows trapped nanospheres to exhibit extremely large quality factors, they require UHV systems and complex stabilization mechanisms for their optical traps, making them impractical as sensors and for other applications. Chip-based mechanical oscillators have recently also been shown to feature competitively large mechanical quality factors at room temperature with $Q_{\mathrm{M}} \gtrsim 10^8$, most prominently in high-stress silicon nitride membranes [58–60]. Here, similar limitations as with levitated nanospheres, such as mirror noise [61, 62], exist.

In this work, we develop a new type of fully integrated optomechanical structure that allows us to significantly increase the mechanical quality factor of a high-frequency in-plane mode, while also allowing to realize a coupled opto-mechanical cavity used for on-chip optical read-out of the motion. We measure a $f_{\mathrm{M}} \cdot Q_{\mathrm{M}} \approx 2.6 \times 10^{13}$, combined with an optomechanical coupling of $G_{\mathrm{OM}}/2\pi = 21.6 \pm 0.2$ GHz/nm, enabling us to cool the mechanical mode from room temperature to 1.2 mK. This corresponds to a thermal mode occupation of less than 27 phonons, a reduction by more than 5 orders of magnitude in the effective temperature. Our novel design applies previous discoveries on the dominant role of bending losses and results in a device that resembles a fishbone-like photonic and phononic structure.

3.2. Device

Significant progress has been made over the last years in understanding and mitigating the losses in integrated (opto-) mechanical structures, resulting in experimental demonstrations of ultra-high Q_{M} devices. In particular, bending loss has been shown to be one of the dominant limiting mechanisms for mechanical quality factors in 1D high-stress silicon nitride structures [37, 64]. Various approaches in strain [58, 59] and mode shape engineering [64] have recently succeeded in achiev-

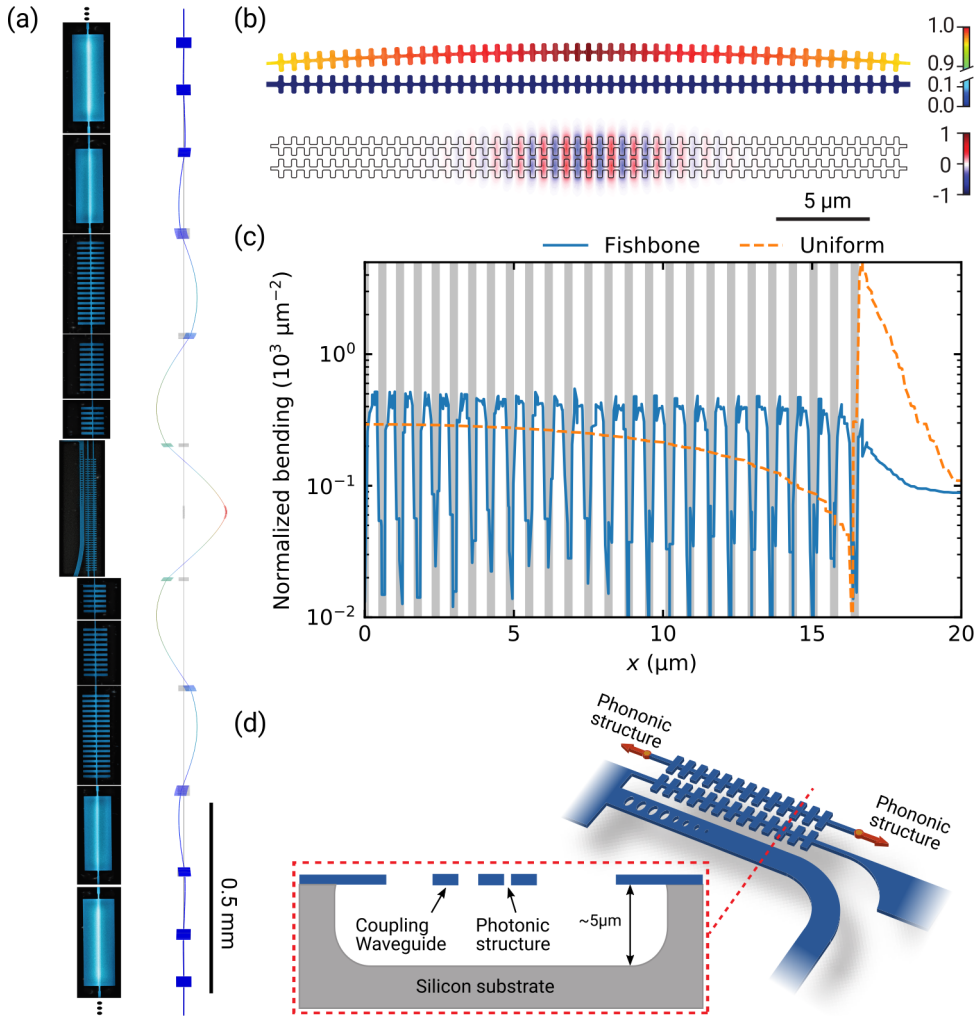

Figure 3.1: (a) A stitched SEM image of the fabricated structure (left) and the simulation of a high quality factor mechanical mode (right). (b) Mechanical (top) and photonic (bottom) simulation of the center part containing the photonic crystal. A short second beam forming the other half of the photonic crystal cavity is fixed close to the mechanical beam. The short structure does not feature any mechanical motion around the defect-mode. The two structures form an optical cavity with the light strongly confined in the gap between the two beams. The mechanical motion changes the gap size, shifting the optical resonance frequency and hence giving rise to the optomechanical interaction. (c) Bending ($\partial^2 v/\partial x^2$) normalized to the displacement within the photonic fishbone structure. In the center, the magnitude of the bending alternates between the thin (large bending, white) and thick (small bending, gray) parts of the structure. As the mechanical losses are proportional to the cube of the width, the fishbone devices exhibit significantly higher mechanical quality factor a uniform beam of equal width (orange), typically used for photonic crystal zipper cavities [63]. (d) Sketch of the central photonic crystal and coupling waveguide. Clearly visible is the short second beam in the center. A cross-section at the red dashed line is shown in the box on the left.

ing ultrahigh-Q_{M} mechanical resonators. By using adiabatically chirped phononic crystals for example [64], the mechanical mode is localized in the center of the beam and the bending can significantly be reduced, leading to increases in Q_{M}. While this concept works very well for the out-of-plane motion, it is much more challenging for an in-plane mode[65]. This is due to the loss ΔU being proportional to the cube of the thickness in the motional direction [64], which for the in-plane mode is equivalent to the width w of the structure $\Delta U \propto w^3(\partial^2 v/\partial x^2)$, with v being the displacement. In practice, there are several parts of an optomechanical structure that require a certain minimum width, such as the phononic crystal itself, which is partly comprised of wide blocks of material. The bending of these very wide blocks results in large mechanical dissipations. Furthermore, in order to form a good optical cavity, the photonic crystal at the center of the structure also requires a minimum width, which is comparable to the optical wavelength [63]. Both factors largely reduce the attainable mechanical quality factor. With our new fishbone design we minimize w in the parts with maximal bending, allowing us to significantly reduce ΔU.

Our structure is fabricated from a 350 nm thick high-stress (1.3 GPa) silicon nitride layer deposited on a silicon handle wafer. As shown in Figure 3.1(a), it is based on the differential motion of two strings, where one of them is significantly longer (2.6 mm) than the other (115 μm). The longer string of this zipper structure is connected to the chip through a phononic crystal, with a bandgap for the in-plane mode between 610 kHz and 1.10 MHz (Figure 3.2(a)). This design forms a defect in the center, introducing confined modes with frequencies within the bandgap, significantly reducing the losses of these modes. As the amplitude of the modes of interest is largest in the center of the structure, we reduce its bending by introducing an adiabatic transition of the unit cells of the phononic crystals. This results in a weaker confinement and smaller bending close to the center [64]. As mentioned above, this does however not immediately result in a high quality factor of the in-plane modes, as the width of the structure close to the bending areas becomes important. We therefore design the overall device as a string with a width of only 165 nm, limited by our fabrication process. When adding the phononic crystal we avoid wide and rigid regions in the design, segmenting the blocks closest to the center into a fishbone-like structure.

A similar approach is also taken for the central photonic crystal used to read-out the mechanical motion. Instead of a traditional photonic structure with holes in a wavegeuide [63], we achieve an alternating index contrast through a fishbone design. The wider parts are roughly 1 μm in width, while the narrow ones between the teeth have a width of only 165 nm. This geometry localizes the bending to the narrow parts (cf. Figure 3.1c), significantly reducing the overall bending losses. For comparison, we observe a typical enhancement of $f_{\mathrm{M}} \cdot Q_{\mathrm{M}}$ by more than a factor of 5 between devices with and without the photonic fishbone structure.

The optical cavity is formed between the long and short strings and the optical field is confined within the gap formed by the fishbones and designed to operate at a wavelength of around $\lambda = 1550$ nm. Due to the strong confinement, the resonance frequency of the cavity is very sensitive to the gap size. In the simulation, shown

in Figure 3.1b, we obtain an optomechanical coupling strength $G_{\mathrm{OM}}/2\pi = \frac{\partial \omega_{\mathrm{cav}}}{\partial x} = 28.6$ GHz/nm, with ω_{cav} the cavity frequency, for a typical 200 nm gap. Combining G_{OM} with the localized mechanical mode of interest, which has small effective mass $m\mathrm{eff} = 7.36 \times 10^{-14}$ kg, we obtain a single photon coupling rate $g_0/2\pi = 313$ kHz. The resulting optimized structure features a 16.5 μm long photonic crystal cavity, while the overal structure has a length of 2.6 mm.

We design the mechanical defect mode at a frequency $f_{\mathrm{M}} = \Omega_{\mathrm{M}}/2\pi = 950$ kHz. A ringdown measurement of this mode in 5×10^{-6} mbar vacuum, shows a quality factor of 2.73×10^7 (cf. SI), yielding $f_{\mathrm{M}} \cdot Q_{\mathrm{M}} = 2.59 \times 10^{13}$. The total optical resonance's ($\lambda = 1549.9$ nm) linewidth is measured to be $\kappa/2\pi = 33.0$ GHz, and the coupling rate to an adjacent optical waveguide $\kappa_{\mathrm{e}}/2\pi = 31.4$ GHz. The strongly over-coupled cavity ensures that most of the light in the cavity is reflected back into the waveguide, which is necessary to achieve high detection efficiency. To further characterize the device, we measure the optical spring effect (see SI for details), allowing us to experimentally determine a single photon coupling rate of $g_0/2\pi = 237 \pm 2$ kHz, corresponding to an optomechanical coupling of $G_{\mathrm{OM}}/2\pi = 21.6 \pm 0.2$ GHz/nm, in good agreement with simulations. We determine the single photon cooperativity of our device $C_0 = \frac{4g_0^2}{\kappa\Gamma_{\mathrm{M}}} \approx 200$, which represents the relative strength of the single photon interactions against any loss channels, a key characteristics of the system [32, 63].

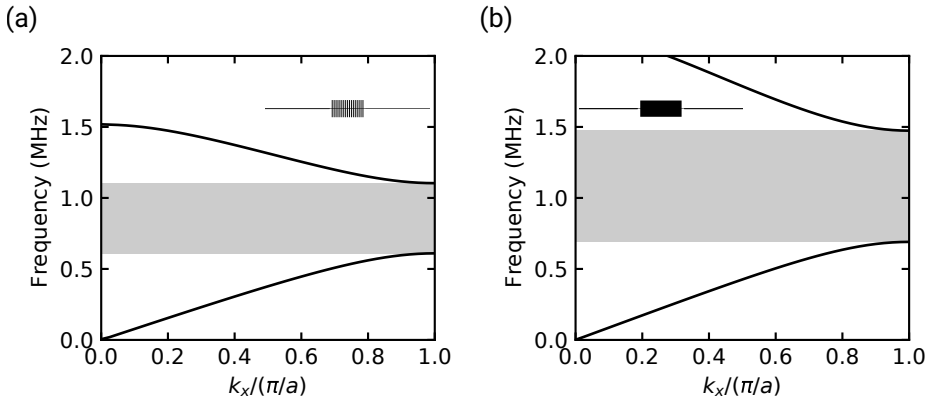

Figure 3.2: Band diagram for the in-plane mode of the phononic (a) fishbone and (b) block structure. We apply a periodic boundary condition in the x-direction, with k_x being the wavevector. The blocks in the long beam form a bandgap between 0.6 and 1.1 MHz for the teeth structure, and between 0.7 and 1.5 MHz for the block structure.

3.3. Experiment and results

In this unresolved side band regime [22], an active feedback cooling scheme can be used to reduce the thermal energy of the mechanical oscillator [52, 66]. In this scheme, unlike in the traditional cavity cooling approach [48], the extremely large bandwidth of the optical cavity allows to retrieve information on the motion of the

mechanical resonator at a high rate. In our experiment, we measure the position of the mechanics and process it in real-time, using the resulting signal to actively control the optical input power into the optomechanical cavity. The modulation of the intensity changes the radiation-pressure force, hence allowing to control and actively cool the mechanics itself. Figure 3.4a shows a sketch and description of our setup used to demonstrate such feedback cooling of our mechanical resonator. The measured signal containing the information on the position of the mechanical oscillator is sent to an FPGA controller (RedPitaya 125-14), with its output directly connected to an electro-optical intensity modulator just before the device. The FPGA control allows us to implement an almost arbitrarily complicated feedback filter. We apply a derivative filter with a 2^{nd} order underdamped low-pass filter to cool the mechanical defect mode. The feedback phase at the resonance frequency is tuned to be $-\pi/2$. Due to a small delay in the system, applying this signal directly would heat other nearby mechanical modes and make the system unstable. We therefore cascade a series of notch filters to tune the phase response locally, which provides a weak cooling over the surrounding modes (cf. Figure 3.3). The total delay of the feedback loop is measured to be 0.49 µs.

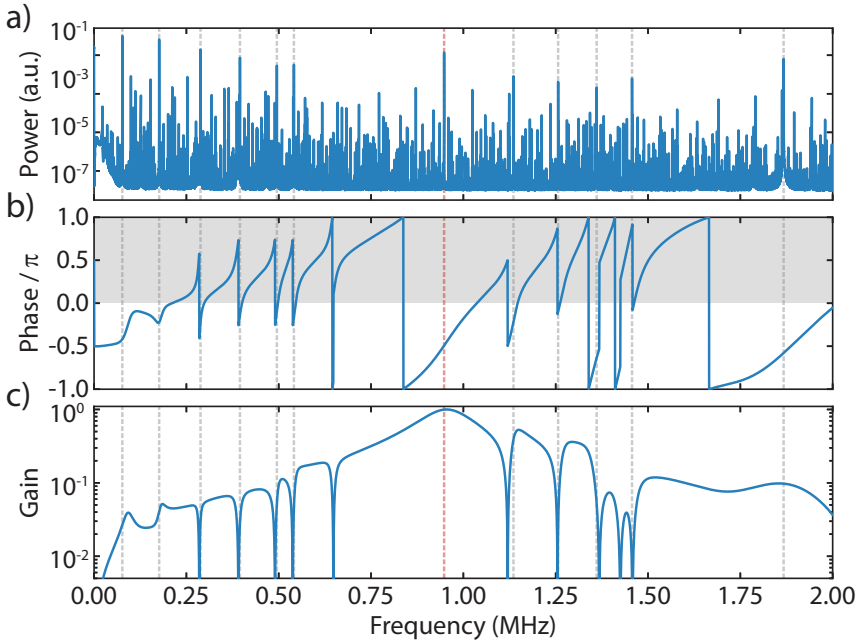

Figure 3.3: (a) Mechanical spectrum. The red dashed line marks the high-Q_{M} defect mode. Gray lines indicate additional mechanical modes that strongly couple to the optical cavity, while most other spurious peaks arise from the mixing of these modes in the detection itself. (b) Phase response of the feedback control. The circuit has a phase of -0.5π at the resonance of the defect mode, with the gray area indicating the unstable region due to heating. (c) Gain of the feedback control. We implement several filter functions with large bandwidth, allowing us to suppress and partly cool other modes that are excited in order to stabilize the system.

Figure 3.4b shows the calibrated displacement power spectrum (S_{yy}) of the mechanical oscillator with different levels of cooling from a bath at room temperature. We keep the cavity photon number fixed at $n_{\mathrm{cav}} = 120$, while increasing the gain of the feedback filter to increase the amount of feedback. The mechanical peak amplitude reduces and broadens, corresponding to a cooling of the mode of interest. The curves are then fitted and we extract the displacement spectrum S_{xx} [52, 63]. This allows us to calculate the average phonon number $\bar{n}$, which is shown as a function of electronic gain in Figure 3.4c. The lowest occupation we obtain is $\bar{n} = 26.6 \pm 0.7$, reduced from 6.5×10^6 at room temperature. We note that our measurements are not quantum-noise-limited in this experiment, resulting in a slightly increased phonon occupancy compared to the theoretically expected value. This additional noise floor results from the optical fiber touching the waveguide and introducing broadband mechanical modes. These mechanical waveguide modes shift the resonance frequency of the cavity weakly, resulting in an increase of the detection noise. At high gain, this noise is fed into the mechanics and limits the cooling efficiency. Unlike in the ideal case of a quantum-noise-limited measurement, increasing the input optical power does not reduce the classical noise and hence it does not lead to more efficient cooling. Using different types of coupling methods or re-designing the waveguide will allow us to reduce the classical noise further, allowing us to in principle cool to an occupation of $\bar{n}_{\mathrm{min}} \approx 14$, with everything else left unchanged.

3.4. Conclusion and outlook

In summary, we have designed and fabricated a novel, fully intergrated optomechanical system, featuring a fishbone-like photonic and phononic structure, with a $Q_{\mathrm{M}} = 2.73 \times 10^7$ of an in-plane mechanical mode combined with a large optomechanical coupling rate of $g_0 = 237$ kHz. We use this device to demonstrate active-feedback cooling close to the quantum groundstate of motion, starting from room temperature. By tuning the FPGA-based feedback filter, we stabilize spurious modes that strongly couple to the optics, allowing us to reach an effective mode temperature of 1.2 mK, corresponding to less than 27 phonons. Further improvements in the noise performance of our setup, together with enhancements of Q_{M} and optomechanical coupling, should allow for these structures to be cooled fully into their groundstate, which will enable mechanical quantum experiments at ambient temperatures. In addition, the simplicity in fabrication of our devices, consisting of a single SiN layer on chip only, combined with their fully integrated on-chip character, makes them ideal candidates for quantum sensing applications [47, 63].

In order to get even closer to the groundstate in the continuous feedback cooling scheme, the measurement rate ($\Gamma_{\mathrm{meas}} = x_{\mathrm{zpf}}^2 / S_{xx}^{\mathrm{imp}} = 4\eta n_{\mathrm{cav}} g_0^2/\kappa$) has to be comparable or larger than the decoherence rates in the system, i.e. the thermal decoherence ($\Gamma_{\mathrm{th}} \approx \Gamma_{\mathrm{M}} n_{\mathrm{th}}$) and the back-action rate ($\Gamma_{\mathrm{ba}} = \Gamma_{\mathrm{M}} n_{\mathrm{ba}}$, where $n_{\mathrm{ba}} = n_{\mathrm{cav}} C_0$) [32]. Here, η is the overall detection efficiency, which for our experiment is $\eta = 0.50$, while $n_{\mathrm{ba}} = 2.4 \times 10^4 \ll n_{\mathrm{th}}$, hence making the thermal component the dominant decoherence channel. Excluding classical noise, we find $\Gamma_{\mathrm{meas}}/(\Gamma_{\mathrm{th}}/8) = 0.015 \ll 1$ [32], which is orders of magnitude larger than in pre-

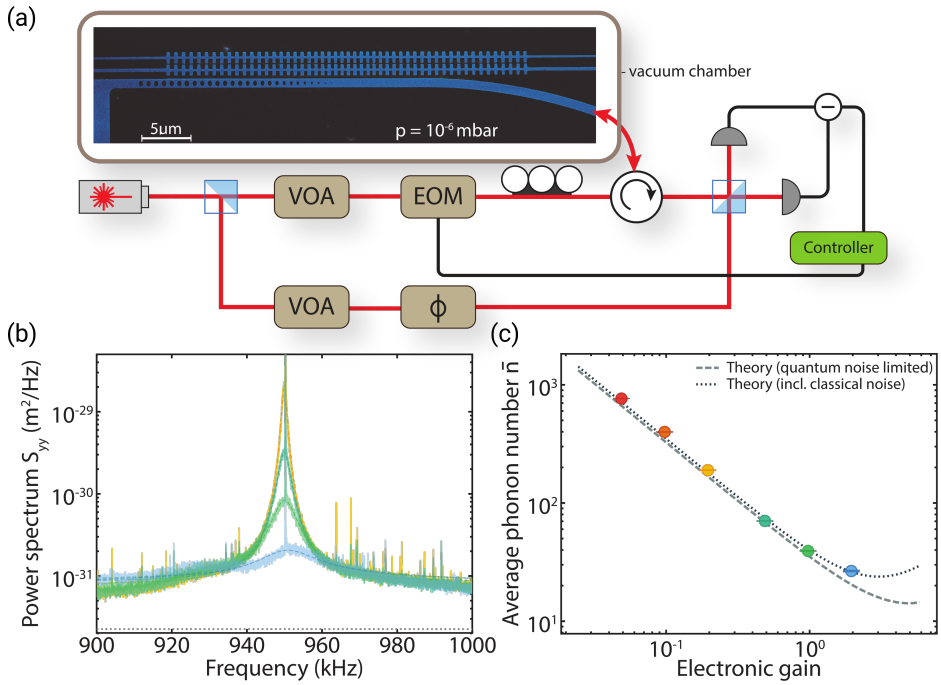

Figure 3.4: (a) Sketch of the feedback cooling setup. A laser is first tuned on cavity resonance and phase modulated to generate a calibration tone. It is then split into two arms, with both intensities being controlled through variable optical attenuators (VOA). The bottom path is the local oscillator for the homodyne detection scheme, where the phase can be controlled using a fiber stretcher (ϕ). The light in the upper (signal) arm is intensity modulated in an electro-optical modulator (EOM) and sent to the waveguide [67], where it is then evanescently coupled into the optical cavity. At the end of the waveguide we pattern a photonic crystal mirror, which allows the light from the cavity to be reflected back into the fiber with a collection efficiency of 91%. This light is then mixed with the local oscillator on a beamsplitter and measured in a home-built low-noise balanced photodetector with a quantum efficiency of 70%, in order to perform the phase-sensitive measurement. The detected signal is electronically processed in an FPGA-based controller, which directly modulates the light in real-time through the EOM, and hence allows to cool the mechanical resonator. (b) Cooled mechanical spectra S_{yy}, with increased feedback gain from orange to blue and constant intracavity photon number n_{cav}. The dashed lines are fits to the spectra, while the gray dotted line indicates the quantum limited noise floor. (c) Average phonon number extracted from the spectra in (b), with corresponding color coding. The gray dashed line represents the theoretically predicted quantum-noise-limited phonon number, and the dark blue dotted line the expected phonon number when taking the noise into account.

vious similar experiments [63].

Several approaches to increasing this ratio exist. For example, by redesigning the coupling waveguide to obtain a quantum-noise-limited measurement, the intracavity photon number can be raised further, and is eventually only bound by absorption heating. Increasing the optomechanical coupling rate can be achieved by improving the fabrication and reducing the gap size between the strings forming the optical cavity. A reduction of the gap to 100 nm yields $G_{\mathrm{OM}} = 2\pi \times 45$ GHz/nm, which is more than twice the current value. Another way is to further reduce the

thermal decoherence rate, through device improvements. Our current design is not optimized to maximize the stress [58], which would lead to more stored energy, increasing Q_{M}. At the moment, the maximum simulated stress in the structure is 1.5 GPa, which is still far below the yield strength of SiN (~6 GPa). Higher stress can also be achieved through an overall longer beam, while at the same time allowing for more adiabatic chirping in the geometry, which would further reduce mechanical losses. Combining all of these approaches should allow to reach the quantum groundstate. In partiular, moderately increasing the mechanical quality factor to $Q_{\mathrm{M}} \approx 1 \times 10^8$, would lead to an increase of $\Gamma_{\mathrm{meas}}/(\Gamma_{\mathrm{th}}/8)$ to 0.06 and the phonon number could be reduced to 6. Together with a reasonable reduction of the gap to 100 nm and a small increase of the cavity photon number to 200, a phonon occupation around 3 will be achievable. Further improvements in Q_{M} to $\gtrsim 7 \times 10^8$ [60, 64] will finally enable phonon numbers below unity starting from room temperature.

3.5. Supplementary Information

3.5.1. Device design

For our design, we first set the geometry of the photonic crystal as the fishbone structure. We then fix the width of the narrow part of the photonic crystal to 165 nm, a width that can easily be fabricated with high yield. The photonic crystal consists of adiabatically chirped unit cells, with a defect region at the center and mirror regions at the ends. We then perform finite element simulations (FEM) of the optical properties of a unit cell of the mirror region and the defect, using COMSOL. The free parameters are the period of the unit cells, as well as the width and the length of the wide part. These parameters are tuned such that we obtain a bandgap around 1550 nm for TE-like modes for the mirror. We design the defect such that the lower-band crosses the center of this bandgap. With this initial design we then run an optimization algorithm [68] maximizing G_{OM}/κ, where G_{OM} is calculated using the moving boundary effect [69].

The mechanical simulations are also performed using COMSOL, where the width of the initial string is again chosen to be 165 nm. We first simulate the band structure for the unit cell closest to the clamping region and a unit cell of the last phononic fishbone structure. In order to reduce the parameter space for the fishbone structure, both its vertical width and the distance between individual fins is fixed to 0.8 μm. Through the simulations, we find bandgaps for the block and fishbone structure, respectively. Finally, we run a full mechanical simulation of the whole assembled long string. As the stress differs between the individual unit cell and the complete simulations, we manually adjust the length of the string in order to obtain the right mode. We then again run an optimization, this time maximizing $f_{\mathrm{M}} \cdot Q_{\mathrm{M}}$, where Q_{M} is evaluated as the ratio between the stored elastic energy and the bending loss [35]. We also set a lower bound on f_{M} in the optimization.

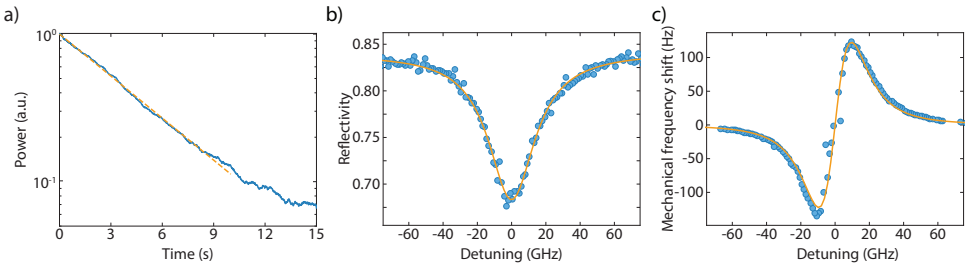

Figure 3.5: (a) Ringdown measurement of the mechanics with a decay time constant of 4.58 s, corresponding to a mechanical quality factor of $Q_{\mathrm{M}} = 2.73 \times 10^7$ ($\omega \mathrm{M}/2\pi = 950.4$ kHz). (b) Normalized optical cavity resonance ($\lambda = 1549.9$ nm). (c) Optical-spring effect measured by detuning the laser around ω_{M}. The fits to (b) and (c) yield a total cavity linewidth $\kappa/2\pi = 33.0$ GHz and optomechanical coupling $G_{\mathrm{OM}}/2\pi = 21.6$ GHz/nm.

3.5.2. Device fabrication & characterization

Our devices are fabricated from a 350 nm thick high-stress silicon nitride film deposited in an LPCVD furnace on silicon. The pattern is first generated using standard electron beam lithography and then transferred into the silicon nitride layer using a CHF_3 plasma etch. Next, we clean the chip in a piranha solution and use hydrofluoric acid to remove any oxidation. Finally, we undercut our structures using a fluorine-based dry release [47]. We would like to highlight the simplicity of the fabrication process, requiring a minimal amount of steps in order to make the suspended structure, completely avoiding the need for complex multilayered processes [65].

In order to measure the mechanical and optical properties of our device, we perform a mechanical ringdown measurement, as well as a wavelength sweep of the optical resonance (see Figure 3.5a,b), respectively. We determine the optomechanical coupling rate by measuring the optical spring effect of the mechanical mode as a function of laser detuning (cf. Figure 3.5c).

The mechanical spectrum close to our mode of interestis shown in Figure 3.7a, from which we identify and verify that the mechanical mode we measure is the correct in-plane mechanical mode we design. A zoom-in of thespectrum around 948 kHz (gray region) is plotted in Figure 3.7b. Due to the single-layer geometry, the in-plan emode (left) has a large optomechanical coupling, while the coupling of the out-of-plane mode (right) is weak. The out-of-plane mode has a slightly higher frequency, which agrees with our simulations (see c and d). We further confirm the mode by comparing it with a higher order in-plane mode (green arrow, Figure 3.7e), whose frequency is 19 kHz higher, which is also in excellent agreement with simulations (20 kHz higher).

3.5.3. Large cavity linewidth

In this work, the optical linewidth is 33.0 GHz, with an intrinsic linewidth of 31.4 GHz. Here, I justify the large linewidth used in this work.

Consider the fundamental mode. The long string has a fundamental mode at 76 kHz and with an effective mass of $m = 10^{-12}$ kg. At room temperature, the thermal

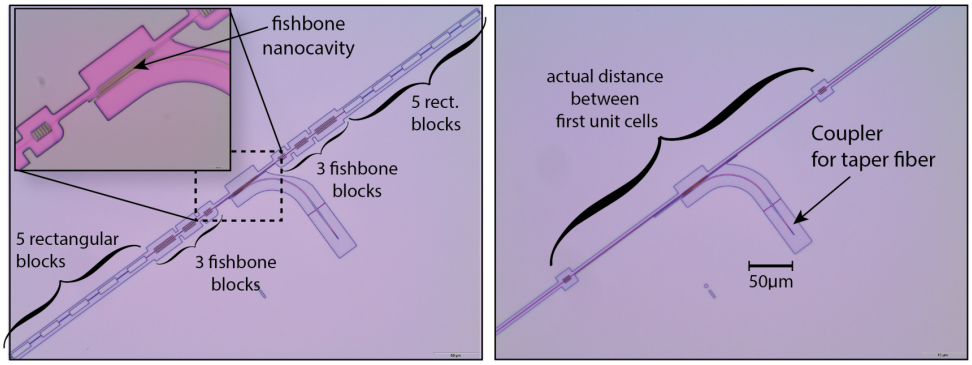

Figure 3.6: (Left) Microscope image of the complete device design. The tethers of the structure shown here are shortened by about a factor of 10 compared to the device used in the main text in order to fit into one picture. The long beam consists of the fishbone nanocavity structure in the center, symmetrically connected on both sides by 3 fishbone phononic shield blocks, followed by 5 rectangular phononic shield blocks and then clamped to the chip. The inset shows a zoom-in of the fishbone nanocavity. (Right) Shown is an image of the device with the actual dimensions used in our experiments, with only the first fishbone phononic shield blocks visible. Both images show the waveguide used to couple light from the tapered optical fiber into the photonic crystal cavity.

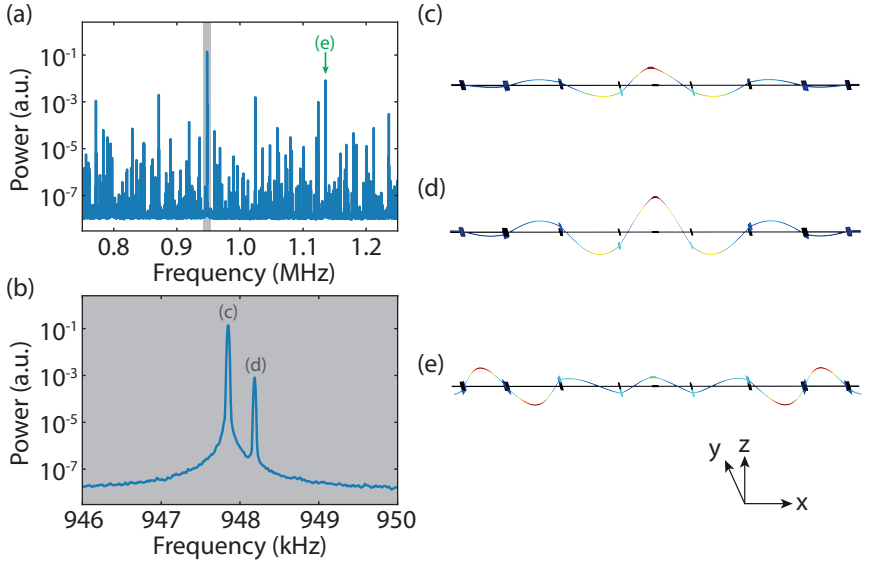

Figure 3.7: (a) Mechanical spectrum close to the high-Q mode. A zoom-in of the highlighted gray area is shown in (b). (c-e) Simulated mode shapes of the corresponding modes labeled in (a) and (b). The mode in (c) is the in-plane mode of interest, (e) a higher order mode, while (d) is an out-of-plane mode.

fluctuation would be $x_{\mathrm{rms}} = 0.16\,\mathrm{nm}$. The fundamental mode has a similar optomechanical coupling G_{OM} as the mode of interest since they have a similar deformation at the photonic crystal region. The thermal fluctuation then corresponding a fluctu-

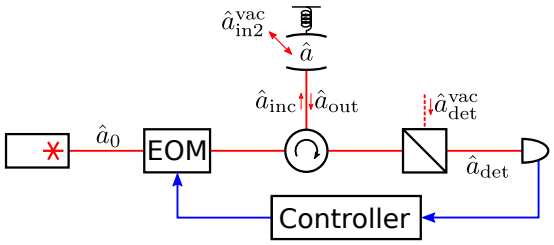

Figure 3.8: A general measurement-based feedback cooling scheme. Optical paths are indicated in red and the flow of electrical signals is indicated in blue. The light from the laser is modulated by an intensity EOM, and then the light travels to the optomechanical cavity. The reflected light is collected and measured. The signal is then fed to a classical controller, which controls the intensity EOM.

ation of the cavity resonance frequency of $\delta\omega_{\mathrm{cav}}/(2\pi) = 3.4$ GHz. The system has many more modes. The fluctuation for the third order in-plane mode is 1.1 GHz, and for the mode of interest is 0.9 GHz. To keep the system in a linear regime, the cavity linewidth should be much larger than the cavity resonance frequency fluctuation. Therefore, a cavity of a large linewidth is used in this work. Still, in figure 3.3, it is possible to see lots of mixing of the modes. In the cooling spectrum in figure 3.4, there are spikes near the mode of interests. They are also from the mixing of different modes in the readout. When the feedback strength is increased, these spikes diminish.

3.5.4. Measurement-based feedback cooling theory

Here, I sketch the theory in the measurement-based feedback cooling, following the treatment in [70].

A scheme of the feedback cooling is sketched in figure 3.8. Light from a continuous wave laser with $\Delta = 0$ is intensity-modulated by an intensity EOM, and then it is sent into the optomechanical cavity. For a modulation depth $\epsilon(t)$, $\alpha_{\mathrm{in}}^2 = (1+\epsilon(t))\alpha_0^2$. Here, I choose the phase convention that α_0 is real and positive, and it is compatible with the phase convention for the optomechanical system since the detuning is 0. For small modulation,

$$\delta\hat{X}_{\mathrm{inc}} = \frac{\epsilon}{2}\bar{\alpha}_{\mathrm{in}} + \delta\hat{X}_{\mathrm{inc}}^{\mathrm{vac}}. \tag{3.1}$$

The first term is due to the modulation of the intensity, and $\bar{\alpha}_{\mathrm{in}}$ is the static input field. $\hat{X}_{\mathrm{inc}}^{\mathrm{vac}}$ is the vacuum fluctuation. In this continuous measurement scheme with small fluctuation, the linearized Langevin equation in the Fourier domain is more convenient to work with. Also, in this work, the cavity decay rate κ is the much larger than the frequency of any dynamics considered in this work ($\kappa \gg \omega$). With $\Delta = 0$, equation 2.8 is simplified as

$$\begin{aligned}\delta\hat{Y}(\omega) &= \frac{4g}{\kappa}Q(\omega) + \frac{2}{\kappa}\left(\sqrt{\kappa_{\mathrm{e}}}\delta Y_{\mathrm{inc}}^{\mathrm{vac}} + \sqrt{\kappa_{\mathrm{i}}}\delta Y_{\mathrm{in2}}^{\mathrm{vac}}\right),\\ Q(\omega) &= \chi_{\mathrm{M}}(\omega)\left(2g\frac{\sqrt{\kappa_{\mathrm{e}}}}{\kappa}\epsilon(\omega)\bar{\alpha}_{\mathrm{in}} + \frac{4g}{\sqrt{\kappa}}\hat{X}_{\mathrm{in}}^{\mathrm{vac}} + \sqrt{2\Gamma_{\mathrm{M}}}P_{\mathrm{in}}\right).\end{aligned} \tag{3.2}$$

The new input vacuum field is defined as $\hat{a}_{\text{in}}^{\text{vac}} = \left(\sqrt{\kappa_{\text{e}}}\delta a_{\text{inc}}^{\text{vac}} + \sqrt{\kappa_{\text{i}}}\hat{a}_{\text{in2}}\right)/\sqrt{\kappa}$. Also, note that the Y quadrature of the light is not modulated in the scheme, the input of the Y quadrature is only the vacuum noise.

In the detection, Y quadrature of the output light is measured. Let the detection efficiency be η,

$$\begin{aligned} Y_{\text{det}} &= \sqrt{\eta}\left(\delta Y_{\text{inc}} - \sqrt{\kappa_{\text{e}}}\delta Y\right) + \sqrt{1-\eta}\hat{Y}_{\text{det}}^{\text{vac}} \\ &= -4\sqrt{\eta}g\frac{\sqrt{\kappa_{\text{e}}}}{\kappa}Q + \sqrt{\eta}\left(1 - \frac{\kappa_{\text{e}}}{\kappa/2}\right)Y_{\text{inc}}^{\text{vac}} + \frac{\sqrt{\eta\kappa_{\text{e}}\kappa_{\text{i}}}}{\kappa/2}\delta Y_{\text{in2}}^{\text{vac}} + \sqrt{1-\eta}Y_{\text{det}}^{\text{vac}}. \end{aligned} \tag{3.3}$$

The measurement result is then fed to a controller. In this work, a linear filter is implemented. Let the transfer function of the filter be $h_{\text{fb}}(\omega)$. The classical modulation then becomes

$$\epsilon(\omega) = -h_{\text{fb}}(\omega)Y_{\text{det}}(\omega). \tag{3.4}$$

The scheme forms a control problem and it is possible to solve for $Q(\omega)$. The phonon occupancy can be find by integrating the spectrum of the mechanical resonator

$$\bar{n}_{\text{th}}^{\text{cooling}} = \frac{1}{2}\left(\int_{-\infty}^{\infty}\frac{\mathrm{d}\omega}{2\pi}\left(1 + \frac{\omega^2}{\Omega^2}\right)S_{QQ}(\omega)\right) - \frac{1}{2}. \tag{3.5}$$

The above equations assume shot-noise limited detection. However, in this work, a large classical noise presents. A classical noise term $Y_{\text{det}}^{\text{Noise,cl}}$ can be incoherently added to the detection signal in equation 3.3,

$$Y_{\text{det}} = \sqrt{\eta}\left(\delta Y_{\text{inc}} - \sqrt{\kappa_{\text{e}}}\delta Y\right) + \sqrt{1-\eta}\hat{Y}_{\text{det}}^{\text{vac}} + Y_{\text{det}}^{\text{Noise,cl}}. \tag{3.6}$$

The classical noise raises the noise floor in the detection, and hence feedback controller add more noise to the mechanical resonator. It increases the final phonon occupancy.

In this scheme, the ability to resolve the mechanical motion is of great importance. In the measurement, the signal from the mechanical resonator mixes with measurement noise. In an ideal experiment without all the classical noise, there is still vacuum fluctuation. It is illustrative to define a measurement rate Γ_{meas} (see section 2.1.5). Heuristically, It can be understood as the time scale to resolve the zero-point fluctuation of the mechanical resonator. The final phonon occupancy can then be roughly estimated by comparing it to the thermal decoherence rate Γ_{M}, which is the heating rate when phonon occupancy is 0. A ground state is achieved only if the thermal decoherence rate is comparable or lower than the time it takes to resolve a single phonon.

3.5.5. Stable feedback cooling

In the presence of multiple modes with relatively high quality factor and a significant delay, a feedback controller should be carefully designed. The delay introduces a

phase lag for the control, which can turn cooling into heating for some of the mechanical modes. Combining equations 3.2, 3.3 and 3.4 yields the form

$$Q(\omega) = \chi_{\mathrm{M}}(\omega)\left(-\beta h_{\mathrm{fb}}(\omega) Q(\omega) + N_{\mathrm{in}}(\omega)\right), \tag{3.7}$$

where $N_{\mathrm{in}}(\omega)$ denotes all the input (noise) terms, and $\beta = -8\sqrt{\eta} g^2 \frac{\kappa_{\mathrm{e}}}{\kappa^2}\bar{\alpha}_{\mathrm{in}}$. Then,

$$Q(\omega) = \chi_{\mathrm{M}}^{\mathrm{eff}}(\omega) N_{\mathrm{in}}(\omega). \tag{3.8}$$

Here, the effective susceptibility is defined,

$$\begin{aligned}
\chi_{\mathrm{M}}^{\mathrm{eff}}(\omega) &= \chi_{\mathrm{M}}(\omega) / \left(1 - \beta h_{\mathrm{fb}}(\omega)\chi_{\mathrm{M}}(\omega)\right) \\
&= \Omega_{\mathrm{M}} / \left(\Omega_{\mathrm{M}}^2 - \omega^2 - \mathrm{i}\Gamma_{\mathrm{M}}\omega - \Omega\beta h_{\mathrm{fb}}(\omega)\right) \\
&= \Omega_{\mathrm{M}} / \left(\Omega_{\mathrm{M}}^2 - \omega^2 + \Omega\beta \mathrm{Re} h_{\mathrm{fb}}(\omega) - \mathrm{i}\left(\Gamma_{\mathrm{M}} - \frac{\Omega_{\mathrm{M}}\beta}{\omega}\mathrm{Im} h_{\mathrm{fb}}(\omega)\right)\omega\right).
\end{aligned} \tag{3.9}$$

A stable feedback requires that all the poles of $\chi_{\mathrm{M}}^{\mathrm{eff}}(\omega)$ have negative imaginary parts. When designing the feedback filter, taking care of all the imaginay parts the poles for all the mechanical modes is challenging and it is not necessary. In the last line of equation 3.9, note that the imaginary part of the feedback introduces an effective damping rate $\Gamma_{\mathrm{M}}^{\mathrm{eff}}(\omega) = \Gamma_{\mathrm{M}} + \frac{\Omega_{\mathrm{M}}\beta}{\omega}\mathrm{Im} h_{\mathrm{fb}}(\omega)$. For a mechanical mode with high quality factor, only the frequency range close to the mechanical frequency has a large contribution. For small feedback strength, the feedback term only perturbs the dynamics. Thus, it is good enough to only look at the effective damping at the mechanical frequency, $\Gamma_{\mathrm{M},j}^{\mathrm{eff}}(\omega = \Omega_{\mathrm{M},j})$ for the j-th mode. For $\Gamma_{\mathrm{M},j}^{\mathrm{eff}} < 0$, the damping becomes heating for the mode and the feedback drives the system to an unstable state. Requiring $\mathrm{Im}\ h_{\mathrm{fb}}(\omega) < 0$, or equivalently $\arg\ h_{\mathrm{fb}}(\omega) \in (-\pi, 0)$, ensures that the feedback is cooling, under the approximation. In practice, a small margin to the phase $\arg\ h_{\mathrm{fb}}(\omega)$ is sometimes needed.

3.5.6. Feedback filter design and implementation[1]

In this work, the feedback controller is implemented on Red Pitaya (STEMlab 125-14), a board with analog-to-digital converter (ADC, 125 MSa/s, 14 bit), digital-to-analog converter (DAC, 125 MSa/s, 14 bit) and a field-programmable gate array (FPGA, Xilinx Zynq 7010). The analog signal from the photodetector is first digitized by the ADC, and then it is processed by the FPGA. The signal is then converted back to analog signal by the DAC. The DAC, ADC and the FPGA run at a clock rate of 125 MHz, but the computation for the filter is reduced to 62.5 MHz in order to have sufficient time to perform operations for the filters. Both the sampling rate and the computation speed of the FPGA is still much higher than the frequency range of interest. It is therefore sufficient to approximate the input and the output to be continuous, and a discrete-time analysis is not necessary.

[1] When designing filters for linear continuous-time signal processing, analysis are in general performed in Laplace space. However, it is sufficient to stay in Fourier domain in this part, and therefore I only analyze the transfer function in Fourier domain. The Laplace space is related to the Fourier domain, under the convention in this work, by $s = \sigma - \mathrm{i}\omega$, where σ is a real number.

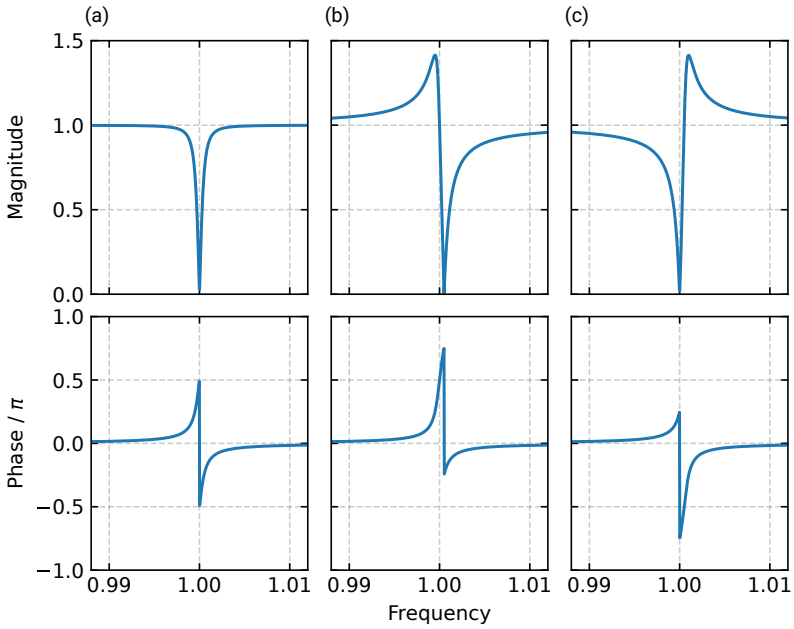

Figure 3.9: Transfer function of (a) a notch filter and (b, c) its variants. The upper panels are for the magnitude respond and the lower are the phase response. The frequency is in arbitrary unit. For a notch filter, the center frequency $\sqrt{b_0}/(2\pi) = 1$, and the bandwidth $\sqrt{b_1}/(2\pi) = 0.001$. a_2, representing the gain, is set to 1. It brings a phase shift of $\pm 0.5\ \pi$. By changing a_2 and b_2, it is possible to tune the phase response. It is useful to address the mode at a frequency where the response of the feedback controller is close to 0.5π. (b) $\sqrt{a_0}/(2\pi) = 1.0005$ and $\sqrt{b_0}/(2\pi) = 1$. The phase response is shifted to the positive side. (c) $\sqrt{b_0}/(2\pi) = 1.0005$ and $\sqrt{a_0}/(2\pi) = 1$. The phase response is shifted to the negative side.

Before introducing the design strategy and implementation details, it is noteworthy to mention the general form of a (maximum) second order filter, with a transfer function

$$\frac{a_2\omega^2 + a_1\omega + a_0}{\omega^2 + b_1\omega + b_0}. \tag{3.10}$$

The filter design is built on top of it. Note that it also directly gives the biquad filter in a discrete time realization.

The goal is to cool the main mechanical mode to a low thermal occupation state. To do the feedback cooling, a band-pass filter of the form

$$\frac{\omega}{\Omega_0^2 - \omega^2 - \mathrm{i}\Gamma_0\omega} \tag{3.11}$$

is firstly assigned, where Ω_0 and Γ_0 are the parameters of the filter. It is the main filter that handles the main mode. It provides a high response around its resonance frequency, and the response is low for other frequencies. Two additional elliptic low pass filters provide extra damping to the feedback response at high frequencies.

For other mechanical modes, the response of the feedback filter would thus be low for the experiment condition. It is, however, not low enough to avoid heating of these modes.

To keep the system stable, efforts should be taken to avoid heating of other modes. As motivated in 3.5.5, the feedback should has a phase response between $-\pi$ and 0 at the resonance frequency of these modes. To to this, starting from the first mode, I cascade second order filters when necessary to make sure that $\Gamma_{\mathrm{M}}^{\mathrm{eff}}$ for the specific mode is damping. A typical example is the second order notch filter, with its transfer function shown in figure 3.9(a). It is essentially a bandpass filter with $a_1 = 0$ and $a_0/a_2 = b_0 > 0$ in equation 3.10. The center frequency of the stopband is $\sqrt{b_0}/(2\pi)$, and the bandwidth is given by $b_1/(2\pi)$. It has a large phase tuning range of $\pm 0.5\pi$ and low response at the center frequency. It is useful to damp the response and tune the phase simultaneously. Small modifications to a notch filter changes the response, with a different phase tuning range, is also useful to tune the phase response. Some examples are shown in figure 3.9(b, c). They are in general required for closely spaced mechanical modes whose frequencies are around the region where the phase response of the bare feedback controller is about 0.5π. However, these tuning has an expense of increasing the gain for some frequency ranges. Also, they make the filter more expensive in terms of the resources on an FPGA.

In order to achieve a highly efficient cooling, the response of the feedback at frequency of the main mechanical mode should be around -0.5π. It is achieved by adding delay cycles to tune the phase response. Note that each cascaded filter also increases delay of the system. Both adding a pure delay and cascading a filter might lead to the change of the phase condition from cooling to heating for some of the modes. It is thus an iterative process to settle the final filter.

Besides cascading the filter, adding filters in parallel is another option and it does not increase the delay. However, it is challenging to design a parallel scheme. Firstly, the final response is the summation of the complex response of all the filters. It is less intuitive to see how the transfer function behaves by adding a filter in parallel to many existing filters, especially when working on phase and gain of the filter. On the order hand, for a cascaded structure, the response is from a multiplication, where the phase is summed directly. By looking on only the transfer function of the added filter, it is immediate to know the new transfer function of the system. Secondly, in practice, for a complicated mechanical structure with lots of modes, the resource on an FPGA is precious. It is easier to optimize the resource usage with cascaded filter by setting some of the coefficients of the second order filters to be 0. It is also not immediately clear how to optimize for the parallel structure. Therefore, I opted for the cascaded structure in this work.

After designing the filters, the continuous-time design are translated to discrete-time design in MATLAB. The HDL coder module in MATLAB then generates Verilog codes for the filter part. Auxiliaries functions are supplemented to form the final feedback controller. After the signal is sent to the FPGA, the width of the signal is first increased to 25 bits by padding zeros. A higher number of bits reduces the rounding errors. Then, it is smoothed by averaging every 4 adjacent sampling

points. It acts as a simple low pass filter. Immediately, it is decimated to half the data rate. It makes it possible to handle the arithmetic (addition, subtraction and multiplication) with the high bit width. The signal is then delayed, scaled and sent to the filter part. The output of the filter is scaled again, truncated, and sent to the output of the FPGA. Ideally, the first scaling should make good use of all the available data bits while avoiding overflowing. The second scaling could be used to tune the overall gain of the feedback. Note that a red-pitaya has 2 analog outputs with 125 MSa/s sampling rate. Another output can be used to monitor the internal signal in different phase of this process. This scheme is implemented in Verilog and compiled by Xilinx Vivado.

4

Integrated optomechanical device with high-Q fundamental mechanical mode and large optomechanical interaction

The rapid development of high-Q macroscopic mechanical resonators marks great advances in optomechanics. They potentially allow quantum-limited or quantum-enhanced applications at ambient temperature. However, coupling these structures to light within an integrated structure and achieving high coupling strength places a key challenge in their utilization. Here, we present an integrated optomechanical structure with a versatile fabrication method. A photonic crystal cavity is placed above a mechanical resonator with high-Q fundamental out-of-plane mode, and both are separated by a small gap. A highly confined optical field has a large overlap with the mechanical mode, enabling a high optomechanical interaction strength. With a novel design of the photonic crystal, it is also possible to achieve a very large cavity photon number. We further demonstrate feedback cooling on a device at room temperature, yielding a phonon number of about 22 over the 1.1 MHz mechanical mode. Our novel fabrication method potentially allow accessible quantum experiments and applications with high-Q mechanical resonators.

4.1. Introduction

Integrated cavity optomechanical systems have attracted lots of attentions for the potential in both classical[8, 71, 72] and quantum[21, 73, 74] applications, and for its ability to study fundamental physics[75, 76]. A mechanical resonator with high quality (Q) factor and a large coupling to the optical cavity is important,[22] since they are related to the ability to maintain coherence oscillations and to have an efficient readout and control. Great progress has been made on designing and fabricating mechanical resonators with high quality factor at room temperature.[60, 64, 77] It potentially enables quantum limited sensing[47, 78] or macroscopic quantum phenomena[79] at high temperature. Integrating optical cavity and mechanical resonator with high Q in-plane mechanical mode has also been demonstrated and it shows a large single photon cooperativity. [40] Out-of-plane motion would provide a higher $f_{\mathrm{M}} \cdot Q_{\mathrm{M}}$ product[37, 64], the mechanical frequency times its quality factor, due to the achievable thickness. Even for the fundamental mode, it has been proposed and shown to be able to achieve a high quality factor.[77, 80] Potentially, mechanical structures with the high-Q fundamental out-of-plane modes, with other modes separated far away which minimizes the disturbing from the other closely spaced mechanical modes, provide a clean platform for further quantum optomechanical experiments. However, coupling to an integrated optical cavity is still challenging. Attempts on making integrated optomechanical devices coupling to the out-of-plane motion have been made.[32, 81, 82] However, forming a fully integrated optomechanical device with high Q mechanical resonator is still yet to be achieved as we have noticed.

In this work, we develop a novel type of flexible, fully integrated optomechanical fabrication method that enables a large optomechanical coupling to the out-of-plane mechanical mode. Especially, we demonstrate devices with mechanical resonator having a high-Q fundamental mode. By using a pick-and-place technique [83, 84], we fabricate structures where a photonic crystal is placed above a mechanical resonator with a 1.1 MHz fundamental out-of-plane mode and an intrinsic quality factor of around 2×10^7. The photonic crystal and the mechnical structure are separated by a controllable small gap of around 100 nm. With the versatile fabrication technique, we have reliably fabricated devices with different gap distances, and find that both the mechanical quality factor and the optomechanical coupling of the fully integrated structure are sensitive to the gap. For a spacing of 130 nm, it is possible to achieve a $g_0/2\pi \approx 260$ kHz and $Q_{\mathrm{M}} \approx 1.6 \times 10^7$ simultaneously. This corresponds to $f_{\mathrm{M}} \cdot Q_{\mathrm{M}} \approx 2.9(k_{\mathrm{B}}T/h)$ at room temperature. We further show that the structure allows a large intracavity photon number, potentially allowing approaching a unity quantum cooperativity C_{qu} at some high temperature. We perform feedback cooling with a large feedback bandwidth on a device with $Q_{\mathrm{M}} = 1.5 \times 10^7$, and we obtain an effective phonon occupation of 22.1 ± 1.0. The minimum achievable phonon number is currently limited by the mechanical motion of the photonic crystal at low frequency, which introduces classical noise. This technique potentially provides a versatile platform for future experiments and applications with high-Q out-of-plane mechanical motion.

4.2. Structure and fabrication

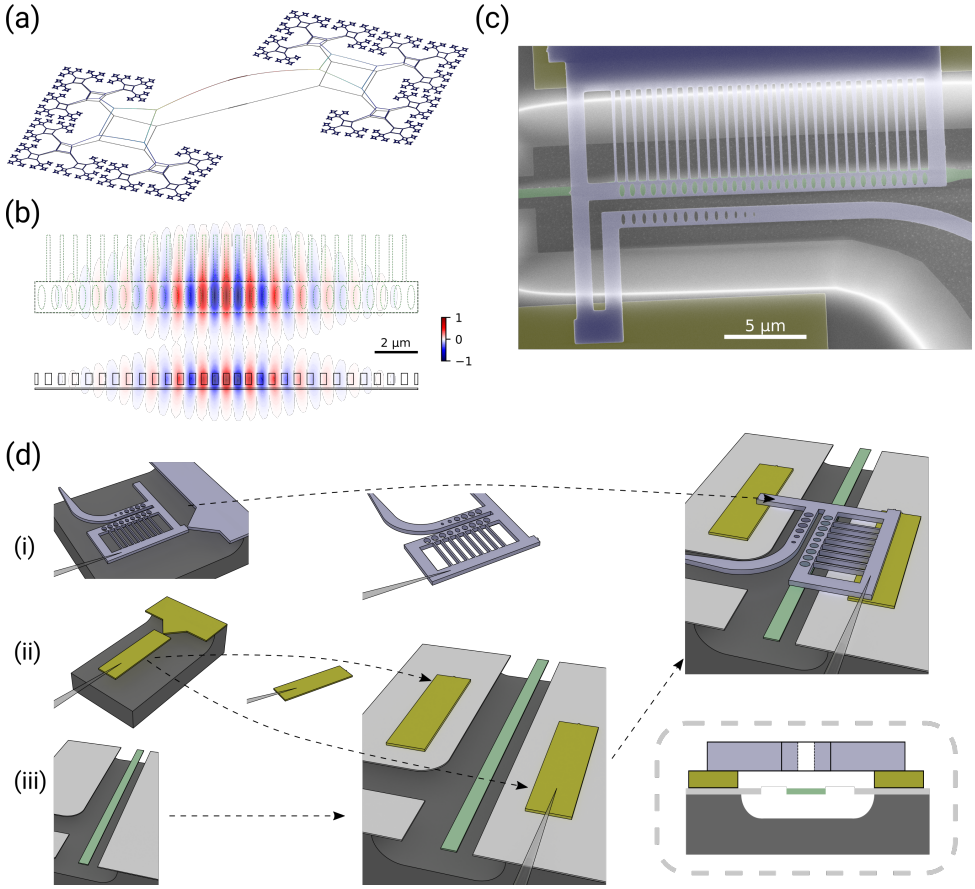

Figure 4.1: (a) Simulation of the fundamental out-of-plane mechanical mode of the fractal structure. The mechanical motion is gradually damped from the center to the clamping points. (b) Electric field distribution (top) on the upper surface of the mechanical layer and (bottom) on the center vertical plane. The green dashed line on the upper plot shows the projection of the photonic crystal. The mechanical layer in the simulation has a width of 1 µm, the same as the width of the photonic crystal. (c) An SEM image of the coupling part between the photonic crystal structure (purple) and the mechanical resonator (green). Spacers (yellow) are put between to separate the photonic crystal and the mechanical structure. The assembling of the three-layer structure is sketched in (d). The process starts from three different chips, all structures are fabricated on the silicon nitride thin film. They are patterned with (i) photonic crystals, (ii) spacers, and (iii) mechanical structures. A fiber is used to pick up the spacers and to place them on the mechanical chip. Then the photonic crystal is stacked on top of the spacer. Drawing in the box at the bottom-right is the side view of the assembled structure. Photonic crystal is placed on top of spacers, which are placed on the non-overhanging part of the silicon nitride. The thickness of the spacers determines the gap distance between the photonic crystal and the mechancial resonator.

Our mechanical structure is inspired from a fractal-like structure [77, 80], which has been proposed and shown to have an extraordinary high quality mechanical factor over the fundamental mode for low frequency mechanics. The mechanical

resonator in this work is targeted at around 1 MHz with a smaller footprint. The fundamental mode of the self-similar structure is shown in figure 4.1(a). Each unit is connected to three similar, but smaller, child units. Our mechanical structure is made on 50 nm thick high stress silicon nitride, and it is well known that stress increases the mechanical quality factor.[36, 37, 64] A thinner material would lead to a higher mechanical quality factor [37, 64], at the expense of reducing the optomechanical coupling. In our structure, comparing to the binary tree [77], an additional child unit facilitates preserving the high stress on the parent unit. The stress at the center can be maintained or even enhanced without significantly increasing the width of the tethers in the child units. In our structure, the width of the tethers marginally increases from 500 nm at the center to 1.4 μm at the clamping. In simulation, the stress is increased to 1.6 GPa at the center tether, up from 1.3 GPa intrinsic stress. The parent and the child units are connected by four tethers forming a diamond shape. Each tether still connects to only two other tethers. The parent and the child nodes, including the node straight after the parent, are then softly connected and it reduces bending loss. In ringdown measurements, It allows achieving a high quality factor as high as 2×10^7 at 1.1 MHz (figure 4.7a).

The optical cavity is formed by a separate photonic crystal cavity, made from silicon nitride with a width of 1.0 μm. The structure and the simulation of the electric field is shown in figure 4.1(b). The photonic crystal cavity strongly confines the light at the center. Extra tethers on the side raise the frequency of its mechanical motion to minimize its impacts onto the mechanical structure. Also, the clamping tethers improve the thermal conductivity of our photonic crystal, allowing a large cavity photon number. The mechanical structure is sensed by and hence coupled to the evanescent field of the photonic crystal cavity, as shown in the bottom of figure 4.1(b). The part of mechanical structure underneath being widened in order to have a larger overlap to the optical field. In this work. we choose a width of 0.8 μm and 1.0 μm. A wider structure lowers the frequency of the low-Q torsional mode of the mechanical resonator (figure 4.8b) and potentially interfere with the measurements to the fundamental high-Q motion.

The fabrication of the devices is based on the "pick-and-place" method [83, 84]. Shown in figure 4.1(d), we first fabricate the mechanical structures, photonic structures, and spacers on three separate chips. The spacers are used to provide a support to the photonic crystals and the thickness defines the gap size. The SiN spacer and the photonic crystals attach to the substrate via a weak tether, with a width of about 100 nm. A tapered fiber with a sharp tip is then placed onto the spacers and onto the photnoic crystal separately, and then a structure can adhere onto the fiber. By moving the fiber, it is possible to break the weak tether and the structure is still attached on the fiber. We first work on the spacers to pick them up and put them on the mechanical chip. Then, a photonic crystal structure is transferred and placed above the spacers, as the top layer. We monitor this process by a camera with a 50× objective. It is sufficient to achieve a good alignment for our silicon nitride photonic crystals, as shown in the SEM image (figure 4.1(c)). The images for transferring a photonic crystal structure is shwon in figure 4.7.1.

Having a small gap between the two layers is important to achieve a high op-

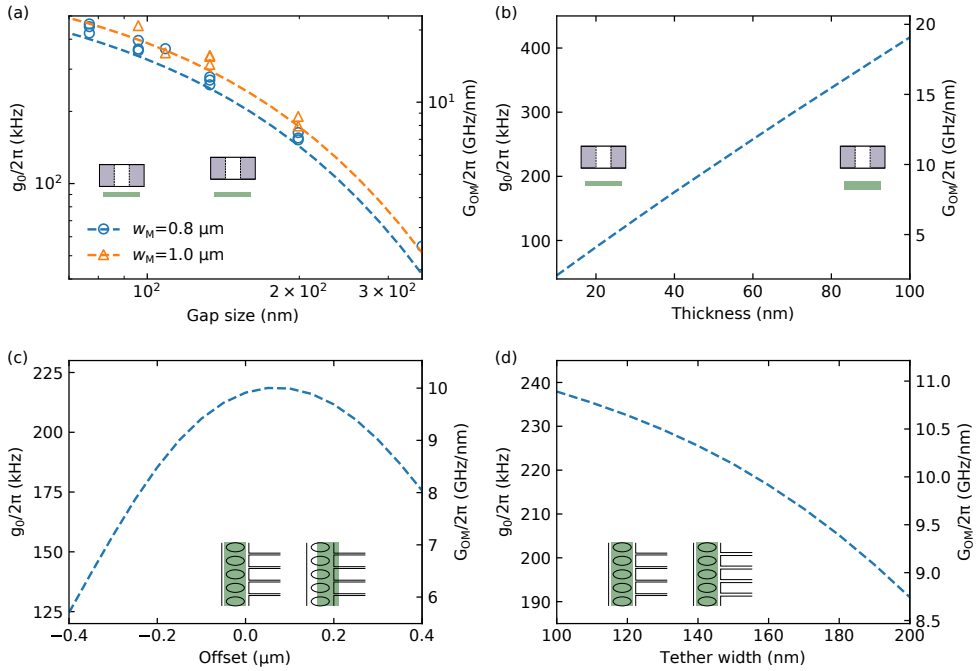

Figure 4.2: g_0 for different (a) gap sizes, (b) thickness of the mechanical layer, (c) misalignment or offsets and (d) widths of the clamping tethers. Dashed lines are simulations. In (a), The circles and triangles are measurement results. Blue and orange are for different mechanical layer thickness.

tomechanical coupling. This is especially the case here as the mechanical resonator only couples to the evanescent field from the photonic crystal. We calculate the optomechanical coupling strength G_{OM} using the perturbation method [69] and the corresponding g_0 for our structure, as shown in figure 4.2. Increasing the gap size from 75 nm to 350 nm reduces the optomechanical coupling strength $G_{\mathrm{OM}}/2\pi$ from 21.6 GHz/nm to 2.2 GHz/nm by one order of magnitude, for a mechanics width of 1 µm beneath the photonic crystal. With this technique, there is no fundamental limit on the gap size, as it is fixed by the spacer. Also, since it is performed in air and there is no process after, there would not be any adhesion issues [85]. With this technique we reliably achieve a gap of 75 nm. We compare the measurements on our devices to the simulations of the optomechanical coupling, which shows good agreement. It also indicates that the alignment in the lateral direction is good with this scheme, since a misalignment would largely reduce the optomechanical coupling (figure 4.2b). In this work, we use a width of 0.8 µm and 1 µm for the mechanical structure direct underneath the photonic crystal. A wider structure allows a larger tolerance, but we find that it is already sufficient. Also, for this asymmetric photonic crystal design, a perfect alignment in the lateral direction does not give the best optomechanical coupling as the clamping tethers attract the optical field to the side (figure 4.2c). When there is no lateral offset, a small reduction in the tether width increases the optomechanical coupling. Another factor for the optome-

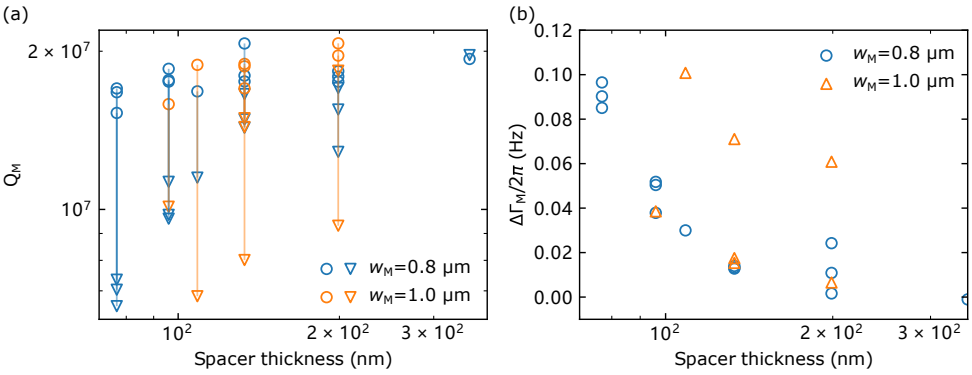

Figure 4.3: (a) Measured mechanical quality factor before (circle) and after (triangle) assembling the mechanical resonator. (b) Increase of the mechanical linewidth Γ_M.

chanical coupling is the thickness of the mechanical layer. For our structure, G_{OM} depends on the electric field difference on the upper and on the lower surface of the mechanical structure. The presence of a thin mechanical layer only perturbs the electrical field distribution. The electric field strength at certain location can then be linearized and its value is very not sensitive to the thickness of the mechanical layer. G_{OM} is then proportional to the thickness of the mechanical structure. This, however, imposes a trade-off for the thickness of the mechanical resonator since a thinner layer is beneficial for the mechanical quality factor [37, 64].

4.3. Change of the mechanical quality factor

After forming the cavity, we see a reduction in the mechanical quality factor. The reduction is more significant for a smaller gap (figure 4.3). We use a large laser detuning to measure the mechanical quality factor, minimizing optomechanical heating or cooling. We have also measured the mechanical quality factor with both blue and red detuned laser and we do not see any difference. Thus we eliminate the possibility of optomechanical cooling or heating. We attribute the reduction of quality factor to some coupling between the mechanical motion of the two layers. The fundamental mode of the photonic crystal structure is shown in figure 4.8(c). While the cause is still being investigating, we can define a coupling parameter. Enlarging the distance reduces the coupling and thus the reduction of the quality factor becomes smaller. An analysis (section 4.7.2) shows that the reduction of its mechanical quality factor depends on the mechanical frequency and qualify factor of the photonic crystal. In this scheme, a photonic crystal is stress-released and its quality factor is low. Thus, clamping tethers are used to increase the mechanical frequency. We saw that by introducing the extra tethers reduce the quality factor degradation.

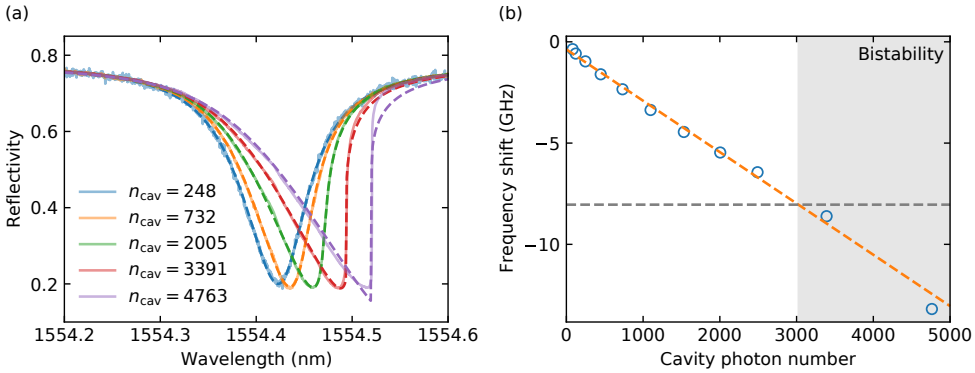

Figure 4.4: Optical resonance frequency shift for different input power (converted to cavity photon numbers on resonance). (a) Reflection spectrum when sweeping the laser from short wavelength to long wavelength. Dashed lines are fittings to extract the frequency shift, and the results are plotted in (b). A linear fit is performed to extract the coefficient for the optical resonance tuning, which is used to obtain the bistability bound. The gray dashed line marks the maxim frequency shift above which the optical bistability occurs. It corresponds to a bistability region in the gray area.

4.4. Improved cavity photon number

Getting a large cavity phonon number is important in cavity optomechanics, as the single photon interaction strength is enhanced by the cavity photon number $g = \sqrt{n_{\mathrm{cav}}} g_0$. Especially, the quantum cooperativity $C_{\mathrm{qu}} = 4\frac{n_{\mathrm{cav}} g_0^2}{\kappa \Gamma_{\mathrm{M}} n_{\mathrm{th}}}$, being proportional to n_{cav}, is a figure of merit for optomechanics in the quantum regime.[22] It compares the photon-phonon interaction rate to the decoherence of the system, and a value comparable or even higher than unity is often desirable.[79] However, due to the heat generation from the photon absorption and the static optomechanical interaction, optical resonance frequency decrease.[86] When the photon number is sufficiently high, bistability occurs and it limits the quantum cooperativity.[22, 63, 87, 88] With the clamping tethers to the photonic crystals, we show that it is possible to achieve a high cavity photon number before reaching the bistability regime. We slowly sweep the laser across the optical resonance from short wavelength to long at different input power and measure the reflection. A measurement is shown in figure 4.4, with $\kappa/2\pi = 10.1$ GHz and a gap size of 130 nm. It has a quality factor of $Q_{\mathrm{M}} = 1.49 \times 10^7$. The cavity photon number shown in the plot is the value on resonance. As the input power is increased, the reflection signal becomes more and more asymmetric. We fit the reflection curves and, from the asymmetry, extract the cavity resonance frequency shift. For the device, we found that bistability occurs for $n_{\mathrm{cav}} \gtrsim 3000$. This corresponds to $C_{\mathrm{qu}} \approx 0.2$ at room temperature, or $C_{\mathrm{qu}} \approx 1$ at 50 K.

4.5. Feedback cooling

We perform measurement-based feedback cooling [70] with the aforementioned device at 300 K. The optical cavity has a coupling to the waveguide $\kappa_e/2\pi = 7.7$

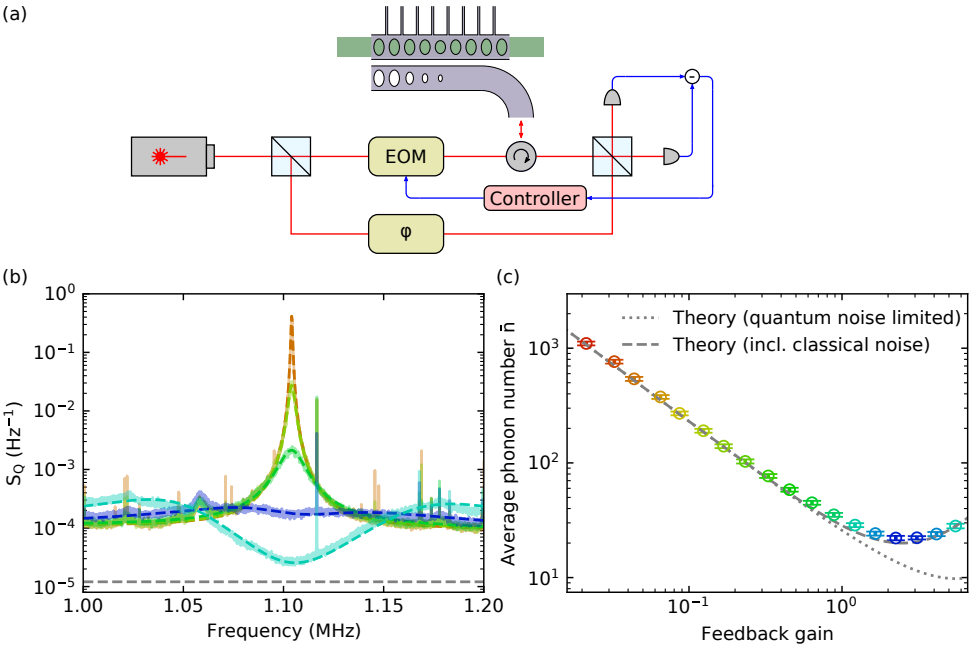

Figure 4.5: (a) Sketch of the feedback cooling setup. A laser on cavity resonance frequency is first phase modulated to generate a phase modulation tone (not shown). The light is then split into two arms. One is attenuated by a variable optical attenuator (VOA), modulated by an intensity electro-optical modulator (EOM), and sent into a waveguide. The light then evanescently couples into the photonic crystal cavity, which is placed above the mechanical resonator (green). At the end of the waveguide it is patterned with photonic crystal mirrors. The light coupled out is then reflected and collected back by an optical fiber. The light then mixes with the light on the other path (local oscillator, LO) with a variable beam splitter, which is tuned to 50:50. The phase difference between the two paths is locked such that the Y quadrature of the light is measured. The measured signal is then send to an FPGA controller, and it controls the intensity EOM to modulate the input power. (b) The measured power spectrum density of the mechanical displacement at different feedback strength. Noise squashing is observed on the light blue curve. The gray dotted line indicates the noise floor of shot noise limited detection. The dashed lines shows the fitting to the measured results, from which the average phonon number at different fitted feedback gain is extracted. The results are shown in (c). The colors in (b) and (c) are correspondence. The dotted line shows the expected phonon number with a shot-noise limited detection and the dashed line shows the expected phonon number with the classical noise extracted from the measurement. They both show good agreement at small feedback gain, while the dashed line captures the increased phonon number due to the classical noise.

GHz. The optomechanical coupling is determined by an optical spring measurement, showing $g_0/2\pi = 257.4 \pm 4.9$ kHz (figure 4.7). It corresponds to a large single photon cooperativity of $C_0 = \frac{4g_0^2}{\kappa\Gamma_M} = 350$, meaning a large measurement rate per photon.[32, 40] The measurement scheme is shown in figure 4.5(a). The laser is tuned to be on resonance of the optical cavity, the phase quadrature of the output light contains the information of the mechanical resonator. Being in the deep sideband-unresolved regime [22, 23], the high bandwidth of the optical cavity allows to resolve the mechanical motion at a high rate. A balanced homodyne mea-

surement is used to measure the phase quadrature, from which the displacement of the mechanical resonator can be obtained. A home-build low noise balanced photodetector converts the optical signal to electrical signal, and then the signal is sent to an FPGA controller (RedPitaya 125-14). The output of the controller connects to an electro-optical intensity modulator right before the device, modulating the input power. By tuning the filter and the delay such that the feedback phase response is $\pi/2$, a cooling can be achieved.

Figure 4.5(b) shows the calibrated single side power spectrum density of the displacement (S_Q, with Q being the displacement in the unit of quanta), at various feedback strength. It corresponds to different gain of the feedback controller. In the measurement, we keep the cavity photon number constant ($n_{\mathrm{cav}} = 341$). The mechanical peaks get broadened and its amplitude is reduced when we increase the feedback gain, corresponding to a reduction of phonon occupation. We fit the traces and extract the average phonon occupancy. It shows a minimum of 22.1 ± 1.0, down from 5.7×10^6 at room temperature. In the experiment, a much higher optical power is still possible, as shown before. However, we are already highly limited by the classical noise and a larger input power does not improve the experiment. For a measurement without the classical noise, we are expecting a phonon number of 10 (dotted line in figure 4.5(c)). The classical noise is mainly due to the low-Q mechanical modes of the photonic crystal (the fundamental mode is plotted in figure 4.8(c)). They all have resonance frequencies much higher than that of the mode of interests. However, the internal damping has a frequency response scaling as $1/f$ [38, 89, 90] for the frequencies lower than the resonance frequency. The thermal force then leads to a substantial low frequency mechanical motion at high temperature, especially for these mechanical modes with low quality factor. It gives the elevated noise floor and it limits the sensing to the mechanical motion of the high Q fundamental mode around 1 MHz. We expect that the noise floor would go down when the device is cooled to a lower bath temperature, since the thermal force is reduced and the intrinsic dissipation of the material get improved [36, 80]. Furthermore, in this work, we use the stress-relieved LPCVD SiN for the photonic crystal and its geometry is not optimized. It has a quality factor of about 560. With this versatile fabrication technique, improvements would also be available by choosing materials with a lower intrinsic mechanical damping and by designing geometries minimizing radiation loss through the clamping. [36, 38, 91–93] Also, by reducing the thickness of the mechanical layer, mechanical quality factor over the mode of interest would increase. [37, 64] To perform feedback cooling approaching the ground state, a measurement rate $\Gamma_{\mathrm{meas}} = 4\eta n_{\mathrm{cav}} g_0^2/\kappa$ should be at least comparable to the thermal decoherence rate, $\Gamma_{\mathrm{th}} = n_{\mathrm{th}}\Gamma_{\mathrm{M}}$.[32] A higher quality factor on the mode of interest means that the measurement rate can be reduced. Simultaneously the measured classical noise would be reduced, improving the performance.

4.6. Conclusion

In summary, we have demonstrated a simple and flexible technique to integrate a photonic crystal cavity with a mechanical device, realizing a large optomechani-

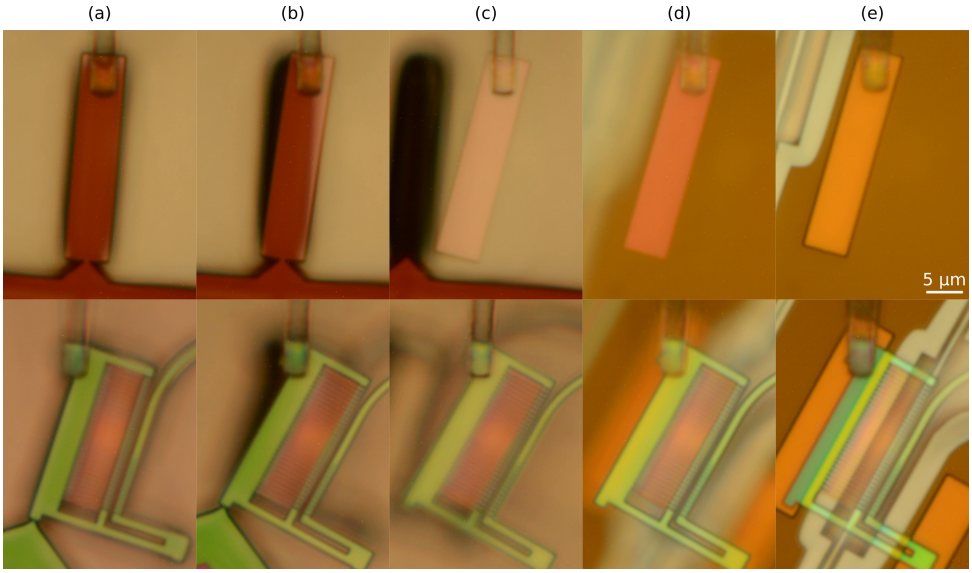

Figure 4.6: Device assembling procedural for the spacers (top) and the photonic crystal (bottom).

cal coupling between a high-Q out-of-plane fundamental mechanical mode and an optical mode of the photonic crystal cavity. The optomechanical coupling strength is sensitive to the distance between the photonic crystal and the mechanical layer, which can be easily set by using spacers of the desired thickness. We find that gap size influences the mechanical quality factor, which is likely from the non-optical coupling between the mechanical motion of the two layers. Further, we show that, with the newly designed photonic crystals with clamping tethers, a large intra-cavity photon number can be achieved. It potentially allows quantum optomechanical experiment at high temperature. We choose an assembled device, with a mechanical quality factor $Q_{\mathrm{M}} = 1.5 \times 10^7$ and an optomechanical coupling $g_0/2\pi = 257$ kHz, and we perform feedback cooling. We achieve an average phonon occupancy of about 22, limited by the classical noise introduce by the thermal motion of the photonic crystal structure. We expect that the classical noise can be overcome by reducing the environment temperature, by using different material, by optimizing the photonic structure design, and by realizing higher mechanical quality factor using thinner mechanical structure.

4.7. Supplementary Information

4.7.1. Assembling procedure

The assembling of a devices is shown in figure 4.6, with the top rows showing taking off and putting down a spacer, and the bottom row shows the process to the photonic crystal. A chip with the spacers, suspended and weakly attached onto the substrate, is first placed under the microscope and monitored by a camera. A fiber

touches the spacer, and bends the weak connection between for the spacer. The connection then breaks. It is then directly brought directly above the mechanical chip. The rotation alignment is done beforehand by fitting the edge of the spacer and by comparing it to alignment markers close to the mechanical structure (not shown). The chip is then brought up slowly until the spacer touches down. A change of color is visible when this process is finished. The same procedural is repeated for different spacers. The transferring of the photonic crystal follows the same procedural. The fiber is attached to the side of the photonic crystal, avoiding any contamination of the photonic crystal from the fiber. Note that the structure of the photonic crystal is large, the whole structure might not touch down simultaneously. It is noticeable in figure 4.6e from the difference of the color. Additional step is performed to force other parts of the photonic crystal to stick onto the spacers.

4.7.2. Reduction of mechanical quality factor

In this work, we see a reduction of mechanical qualify factor after the full structure is assembled. The exact cause is still not known. We attribute it to some coupling between the mechanical structure and the photonic crystal. Examples of the coupling can be from the charges on the structures, or the van der Waals force.

Label the displacement of the photonic crystal as δz_{PhC}, and the displacement of the mechanical resonator as δz_{M}. If they have some arbitrary coupling, it is possible to write

$$F^c_{\mathrm{PhC}} = -F^c_{\mathrm{M}} \approx F^c_0 + \alpha_c(\delta z_{\mathrm{PhC}} - \delta z_{\mathrm{M}}). \tag{4.1}$$

F^c_{PhC} is the force exerted from the mechanical resonator to the photonic crystal, and F^c_{M} is the force on the mechanical resonator. F^c_0 is the force at equilibrium, and α_c is the linear coupling strength. Higher order terms to the displacement are neglected for small displacement. We will be interested in the dynamics. F^c_0 only introduce a constant shift for the equilibrium position and it will be neglected in the following.

The photonic crystal also has its mechanical modes. Here, I simplify both the mechanical resonator and the mechanical motion of the photonic crystal as damped harmonic oscillators. In Fourier domain, they have equation of motion

$$\begin{aligned} \chi^{-1}_{\mathrm{PhC}}(\omega)\delta z_{\mathrm{PhC}}(\omega) &= \alpha_c(\delta z_{\mathrm{PhC}}(\omega) - \delta z_{\mathrm{M}}(\omega)) + F_{\mathrm{PhC}}(\omega), \\ \chi^{-1}_{\mathrm{M}}(\omega)\delta z_{\mathrm{M}}(\omega) &= -\alpha_c(\delta z_{\mathrm{PhC}}(\omega) - \delta z_{\mathrm{M}}(\omega)) + F_{\mathrm{M}}(\omega). \end{aligned} \tag{4.2}$$

$$\chi_j^{-1}(\omega) = m_j\left(\Omega_j^2 - \omega^2 - \mathrm{i}\Gamma_j\omega\right) \tag{4.3}$$

is the inverse of the susceptibility of the mechanical resonator ($j = \mathrm{M}$) or of the photonic crystal ($j = \mathrm{PhC}$). F_j is the force from other sources, such as the thermal force. In a practical structure, multiple modes present. For the specific geometry for the photonic crystal, the three lowest order modes do not have a large frequency difference. Thus this simplified analysis only serve to understanding it phenomenologically. Also, we acknowledge that the dissipation Γ_j is also frequency-dependent for internal damping[38, 89, 90]. Here, we will only be focusing on a small frequency range around Ω_{M} and hence we drop the frequency dependency here. It,

however, could be different from $\Gamma_{\mathrm{PhC}}(\omega = \Omega_{\mathrm{PhC}})$ by a factor $\Omega_{\mathrm{PhC}}/\Omega_{\mathrm{M}}$ for a purely internal damping model. For the whole system, it is then

$$\begin{pmatrix} \chi_{\mathrm{PhC}}^{-1}(\omega) - \alpha_c & \alpha_c \\ \alpha_c & \chi_{\mathrm{M}}^{-1} - \alpha_c \end{pmatrix} \begin{pmatrix} \delta z_{\mathrm{PhC}}(\omega) \\ \delta z_{\mathrm{M}}(\omega) \end{pmatrix} = \begin{pmatrix} F_{\mathrm{PhC}}(\omega) \\ F_{\mathrm{M}}(\omega) \end{pmatrix}. \tag{4.4}$$

Inverting the matrix on the left-hand side, we then have

$$\chi = \begin{pmatrix} \left(\chi_{\mathrm{PhC}}^{-1} + \frac{\alpha_c}{\alpha_c \chi_{\mathrm{M}} - 1}\right)^{-1} & \left(\chi_{\mathrm{PhC}}^{-1} + \chi_{\mathrm{M}}^{-1} - \frac{\chi_{\mathrm{PhC}}^{-1}\chi_{\mathrm{M}}^{-1}}{\alpha}\right)^{-1} \\ \left(\chi_{\mathrm{PhC}}^{-1} + \chi_{\mathrm{M}}^{-1} - \frac{\chi_{\mathrm{PhC}}^{-1}\chi_{\mathrm{M}}^{-1}}{\alpha}\right)^{-1} & \left(\chi_{\mathrm{M}}^{-1} + \frac{\alpha_c}{\alpha_c \chi_{\mathrm{PhC}} - 1}\right)^{-1} \end{pmatrix}, \tag{4.5}$$

$$\begin{pmatrix} \delta z_{\mathrm{PhC}}(\omega) \\ \delta z_{\mathrm{M}}(\omega) \end{pmatrix} = \chi(\omega) \begin{pmatrix} F_{\mathrm{PhC}}(\omega) \\ F_{\mathrm{M}}(\omega) \end{pmatrix}. \tag{4.6}$$

The two modes are coupled. For the device we have, $\Omega_{\mathrm{PhC}} \gg \Omega_{\mathrm{M}}$. Around Ω_{M}, we can still approximate them as separate modes and

$$\delta z_{\mathrm{M}}(\omega) \approx \left(\chi_{\mathrm{M}}^{-1}(\omega) + \frac{\alpha_c}{\alpha_c \chi_{\mathrm{PhC}}(\omega) - 1}\right)^{-1} F_{\mathrm{M}}(\omega). \tag{4.7}$$

as the off-diagonal terms are much smaller in magnitude. Then, for the mechanical resonator, the inverse of effective susceptibility becomes

$$1/\chi_{\mathrm{M}}^{\mathrm{eff}}(\omega) = \chi_{\mathrm{M}}^{-1}(\omega) + \frac{\alpha_c}{\alpha_c \chi_{\mathrm{PhC}}(\omega) - 1}. \tag{4.8}$$

Its imaginary part represents the dissipation [22]. Evaluate around the frequency of the mechanical resonator,

$$\mathrm{Im}\frac{1}{\chi_{\mathrm{M}}^{\mathrm{eff}}(\omega)} \approx -m_{\mathrm{M}} \left(\Gamma_{\mathrm{M}} + \frac{\alpha_c^2 \Gamma_{\mathrm{PhC}}/m_{\mathrm{M}} m_{\mathrm{PhC}}}{\left(\alpha_c/m_{\mathrm{PhC}} - (\Omega_{\mathrm{PhC}}^2 - \Omega_{\mathrm{M}}^2)\right)^2 + \Gamma_{\mathrm{PhC}}^2 \Omega_{\mathrm{M}}^2}\right)\omega. \tag{4.9}$$

The dissipation is increased by

$$\begin{aligned} \delta\Gamma_{\mathrm{M}} &= \frac{\alpha_c^2 \Gamma_{\mathrm{PhC}}/m_{\mathrm{M}} m_{\mathrm{PhC}}}{\left(\alpha_c/m_{\mathrm{PhC}} - (\Omega_{\mathrm{PhC}}^2 - \Omega_{\mathrm{M}}^2)\right)^2 + \Gamma_{\mathrm{PhC}}^2 \Omega_{\mathrm{M}}^2} \\ &\approx \frac{\alpha_c^2}{m_1 m_2} \frac{\Gamma_{\mathrm{PhC}}}{\Omega_{\mathrm{PhC}}^4}. \end{aligned} \tag{4.10}$$

We see that, if there is any coupling between the mechanical resonator and the mechanics of the photonic crystal, the quality factor of the mechanical resonator is always reduced. The last approximation is appropriate for our devices since $\Omega_{\mathrm{PhC}} \approx 8\Omega_{\mathrm{M}}$ for the fundamental mechanical mode of the photonic crystal. Though the equation shows a $\Omega_{\mathrm{PhC}}^{-4}$ dependency, we would like to emphasis that Γ_{PhC} also depends on Ω_{PhC}. Especially, for structural damping, $\Gamma_{\mathrm{PhC}} \sim \Omega_{\mathrm{PhC}}^2$[38, 89, 90]. Still, increasing the mechanical frequency of the photonic crystal reduce the dissipation degradation, and it is one of the reason why the tethers are used. We have designed and assembled photonic crystals without the clamping tethers. $\Omega_{\mathrm{PhC}} \approx 3\Omega_{\mathrm{M}}$, and we see a systematic larger degradation in the mechanical quality factor.

4.7.3. Optical bistability

Optical bistability can be either caused by photon absorption of the material or the static optomechanical effect [22, 86]. Here, we are not intended to distinguish both since they cause similar effects in our measurement.

In the present of linear absorption or the static optomechanical effect, the optical resonance frequency shifts and it is proportional to the cavity photon number with a coefficient β,

$$\delta\omega_{\mathrm{cav}} = \omega_{\mathrm{cav}} - \omega_{\mathrm{cav}}^{(0)} = \beta n_{\mathrm{cav}}(\Delta). \tag{4.11}$$

$\omega_{\mathrm{cav}}^{(0)}$ is the original cavity resonance frequency. In a typical situation, $\beta < 0$. The actual detuning, is then a function of the cavity photon number

$$\Delta(n_{\mathrm{cav}}) = \Delta_0 - \beta n_{\mathrm{cav}}(\Delta). \tag{4.12}$$

Δ_0 is the detuning with vanishing input power and it is a fixed value with given laser wavelength.

Let the cavity photon number at resonance be N_{cav}, as a fixed value for a given input power,

$$n_{\mathrm{cav}}(\Delta) = \frac{(\kappa/2)^2}{(\kappa/2)^2 + \Delta^2} N_{\mathrm{cav}}. \tag{4.13}$$

Equation 4.12 and 4.13 define the behavior of the system, and we use them to fit the traces in figure 4.4a. Combining these two equations, we get a equation of Δ,

$$\Delta^3 - \Delta_0\Delta^2 + \left(\frac{\kappa}{2}\right)^2 \Delta + \left(\frac{\kappa}{2}\right)^2 (\beta N_{\mathrm{cav}} - \Delta_0) = 0 \tag{4.14}$$

Optical bistability occurs when there are more than one possible $\Delta \in R$ for a fixed laser frequency, namely a fixed Δ_0. This regime corresponds to an unstable regime. Consider a situation when $\Delta = 0$ in the bistability regime. A small pertubation, either slightly reducing the photon number or Δ becoming slightly smaller than 0, the cavity photon number is reduced and hence the optical resonance frequency drifts to high frequency side. This then reduces cavity photon number and it makes Δ more negative. Without an active feedback, the resonance would be lost. On the other hands, if there is only a single solution, with a small perturbation, Δ and cavity photon number would return to their original value. For an optical cavity, proposals have been made to work in the regime $\Delta > 0$ [87]. However, this blue detuned regime heats up the mechanical resonator. Thus, the transistion between multiple solution and single solution in equation 4.14 marks the boundary between a stable and an unstable system.

Define

$$y(\Delta) = \Delta^3 - \Delta_0\Delta^2 + \left(\frac{\kappa}{2}\right)^2 \Delta + \left(\frac{\kappa}{2}\right)^2 (\beta N_{\mathrm{cav}} - \Delta_0). \tag{4.15}$$

For equation 4.14, having multiple solutions implies that y is not a monotonically increasing function. $y'(\Delta)$ should have 2 real solutions. Thus, $\Delta_0^2 - \frac{3}{4}\kappa^2 > 0$. With this satisfied, the local minimum and maximum happens when

$$\Delta = \Delta_{\pm} = \frac{1}{3}\Delta_0 \pm \frac{1}{6}\sqrt{4\Delta_0^2 - 3\kappa^2}. \tag{4.16}$$

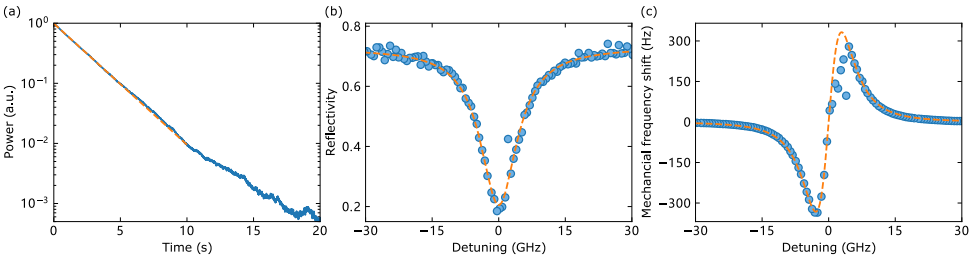

Figure 4.7: The characterization of the device used in the feedback cooling. (a) Ringdown measurement shows a quality factor of $Q_{\mathrm{M}} = 1.49 \times 10^7$ ($\Omega_{\mathrm{M}}/2\pi = 1.10$ MHz). (b) Cavity reflectivity close to the resonance (1554.6 nm). The fitting yields a linewidth $\kappa/2\pi = 10.1$ GHz. (c) Optical spring measurement by detuning the input laser around the cavity resonance frequency. On blue detuning ($\omega_{\mathrm{L}} > \omega_{\mathrm{cav}}$), mechanical frequencies is not stable because of optical heating.

4

Then, the bistability happens if and only if there exists a real ϵ_0 such that $y(\Delta_+) < 0$ and $y(\Delta_-) > 0$. Note that both $y(\Delta_+)$ and $y(\Delta_-)$ are monotonically decreasing as Δ_0 increases in their ranges. The bistability bound is then given by

$$N_{\mathrm{cav}} > \left| \frac{4\sqrt{3}\kappa}{9\beta} \right|. \tag{4.17}$$

The non-stable regime is colored in gray in figure 4.4b, with β obtained by the linear fit of the change of optical resonance frequency. We note that the measurement in the bistability regime might not be reliable. We first do a linear fit to all the data points in figure 4.4b, extracting a bistability bound of $N_{\mathrm{cav}} \approx 3000$. We then perform another fitting with only the data $N_{\mathrm{cav}} < 3000$. We do not see substential different between the two fits. In figure 4.4b, we present the fitting result and the corresponding bistability bound from the latter fit.

4.7.4. Characterization of the device for the feedback cooling

The characterization of the device we used in the feedback cooling is shown in figure 4.7. Ringdown measurement for the mechanical resonator after assembling the full device, optical cavity reflection measurement and the optical spring measurement is shown. A fitting shows a quality factor of $Q_{\mathrm{M}} = 1.49 \times 10^7$ and $g_0/2\pi = 257.4 \pm 4.9$ kHz.

In figure 4.8(a) the spectrum with a wide frequency range is shown. The mode of interest, namely the fundamental mode of the mechanical resonator, is highlighted with green dashed line. Other mechanical modes have very different frequencies. We notice two mechanical modes with low quality factor, one (figure 4.8(b), 2.8 MHz) corresponds to the fundamental torsional mode of the mechanical structure, and the other one corresponds to the fundamental mechanical mode of the photonic crystal (figure 4.8(c), 8.9 MHz). Due to the structural damping in the silicon nitride,[38, 89, 90] they give raise to a noise floor that is much higher than the shot noise at low frequencies (gray dashed line). In the measurement, we also suspect that the mechanical motions of the photonic crystal structure couple to

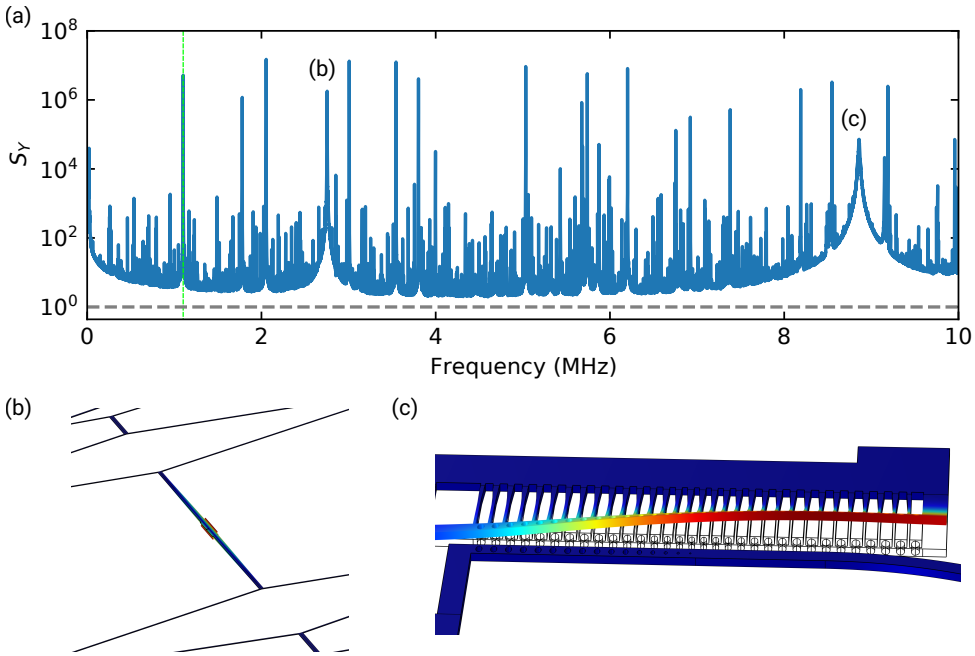

Figure 4.8: (a) A spectrum measurement with a wide frequency range, normalized to the shot noise (gray dashed line). The mechanical mode of interest is marked with green. It is the fundamental mode of the mechanical resonator, and it is far away from other mechanical modes. Two mechancial modes with low quality factor are highlighted, with (b) the torsional mode of the mechanical resonator and (c) the fundamental mechanical mode of the photonic crystal structure.

the mechanical resonator, reducing the mechanical quality factor of the mechanical resonator.

4.7.5. Mechanical resonator design

The mechanical resonator is formed by the fractal structure. On each level of the fractal, parameters, including the tether widths, lengths, the size of the diamond-shape connections, are assigned. This forms a large parameter space. Optimization is then performed with the package Py-BOBYQA [94]. It implements a derivative-free optimization algorithm to minimize the objective function (mechanical quality factor) within a bounded parameter space. It approximates a small region in the parameter space by a quadratic function, and then seek the next point by interpolation. Due to the expensive simulation of the mechanics and the large parameter space, the optimization is terminated when the quality factor is "good enough". For the mechanical structure, it still has in-plane motions and torsional modes. We also want the frequency of the fundamental in-plane mode and the torsional mode far away. It is, however, not included in the optimization part. This is done by manually enlarging the center diamond. It slightly reduces the mechanical quality factor.

5

Coherent feedback of optomechanical system in the sideband-unresolved regime

Preparing macroscopic mechanical resonators close to their motional quantum groundstate and generating entanglement with light offers great opportunities in developing new generation of quantum applications and in studying fundamental physics. We propose an experimental relevant scheme based on coherent feedback with linear, passive optical components to achieve ground-state cooling and photon-phonon entanglement generation with optomechanical devices, especially in the sideband-unresolved regime. We find that, by introducing another passive optical cavity with narrow linewidth, an optomechanical system in the deep sideband-unresolved regime could have a dynamics similar to a sideband-resolved system. The feedback introduces added noise, which depends on the optical loss on the feedback path. Overall the effective quantum cooperativity can be improved with small loss and at reasonable original quantum cooperativity. We also show that it is possible to perform ground state cooling by introducing such an optical cavity, or a mirror with a delay line. Finally, we propose a coherent feedback scheme to generate optomechanical entanglement with additional optical cavities, and the entanglement can be verified by measuring the output light from the cavities. We show that a large squeezing of the Einstein-Podolski-Rosen quadratures for the output light is achievable with feasibly high-Q mechanical resonator, efficient feedback and large quantum cooperativity.

5.1. Introduction

In the past decade, optomechanical systems have seen great progress on many applications and on studying fundamental physics [8, 21, 46, 71–74, 76]. Especially, a microfabricated optomechanical system with a large mechanical resonator and an integrated optical cavity has attracted lots of interest, as it provides a versatile and easy-to-use platform in many areas including sensing,[8, 47] potential usage in a quantum network,[14, 95, 96] and the studying of quantum effect in a truly macroscopic system[11]. These structures typically have a high optomechanical interaction strength, due to the confined optical modes.[86, 97] Recently, many advancements have been achieved over the mechanical resonator, including coherent oscillations at room temperature[40, 60, 64, 80], and over the integration with optical cavities[40] (and see chapter 4). These optomechanical systems typically operate at the sideband-unresolved regime, where the mechanical resonance frequency is lower than the linewidth of the optical cavity. This is a consequence the large mechanical resonator, lowering the mechanical resonance frequency. Also, for the integrated optical cavity with small mode volume, which is essential to obtain a large optomechanical coupling, a small dissipation is challenging to achieve.

Many advancements in optomechanics have been made in the sideband-resolved regime. They are mostly based on the idea of suppressing either the phonon creation or the annihilation process through the optical cavity.[22, 33] In a sideband-unresolved system, however, the suppression is insignificant due to the large optical linewidth, making many proposals incompatible to a sideband-unresolved system. On the other hand, the large bandwidth of the optical cavity allows obtaining the information of the mechanical resonator and interacting to it efficiently. This leads to the ideas including measurement-based feedback[70] and short-pulses based[28–31] schemes. While the measurement-based scheme is still largely limited to performing ground state cooling, cooling and entanglement generation has been proposed based on pulses with a duration much shorter than the mechanical resonance period (short pulse). However, a mechanical resonator is typically not a single-mode system, and the additional modes might present as noise with the short pulses.[98] For continuous measurement, inferring photon-phonon entanglement has also been proposed, with a squeezing of the Einstein-Podolski-Rosen (EPR) quadratures up to 50%.[79] In this work, by further exploring the large bandwidth of the optical cavity, we propose schemes based on coherent feedback by other linear, passive optical elements. We show that it is possible to achieve ground state cooling with continuous drive, and large squeezing of the EPR quadratures with long pulses.

5.2. Optomechanical system

We consider an optomechanical system consisting of a single mechanical mode and a single-mode optical cavity. The mechanical mode has an angular resonance frequency Ω_{M} and an energy damping rate Γ_{M}. Its field is bosonic, and the position and momentum quadratures are described by two normalized Hermitian operators $\hat{X}_{\mathrm{M}}$ and $\hat{Y}_{\mathrm{M}}$. The optical field has a resonance frequency of ω_{C} and an energy

damping rate κ_{C}, with the amplitude and phase quadratures $\hat{X}_{\mathrm{C}}$ and $\hat{Y}_{\mathrm{C}}$. Through out this work, we will also use a vector $\hat{u} = (\hat{X}, \hat{Y})^T$ to represent the quadratures. The four quadrature satisfies the commutation relation $[\hat{u}_{\alpha,i}, \hat{u}_{\beta,j}] = \mathrm{i}\sigma_{\alpha\beta}\varepsilon_{ij}$, where α, β are for C (cavity field) or M (mechanical field), $i, j \in (1, 2)$ for the X or Y quadrature. In the following, we will also use i, j to denote the components of $\hat{u}$. ε_{ij} is the Levi-Civita symbol. $\varepsilon_{ij} = 1$ for $i = 1$, $j = 2$, $\varepsilon_{ij} = -1$ for $i = 2$, $j = 1$, and 0 otherwise. The annihilation operators of the two bosonic field are $\hat{a}_\alpha = (\hat{X}_\alpha + \mathrm{i}Y_\alpha)/\sqrt{2}$. In a frame rotating with the laser (drive) frequency ω_{L}, the Hamiltonian of the linearized dynamics of the system ($\hbar = 1$ throughout this work) [23, 33]

$$H = -\frac{\Delta_{\mathrm{C}}}{2}(\hat{X}_{\mathrm{C}}^2 + \hat{Y}_{\mathrm{C}}^2) + \frac{\Omega_{\mathrm{M}}}{2}(\hat{X}_{\mathrm{M}}^2 + \hat{Y}_{\mathrm{M}}^2) + 2g\hat{X}_{\mathrm{M}}\hat{X}_{\mathrm{C}}. \tag{5.1}$$

The coupling between the optical and the mechanical filed has a strength $g = \sqrt{n_{\mathrm{C}}}g_0$, which is the single photon coupling g_0 [22] enhanced by the photon number inside the optomechanical cavity n_{C}. The detuning $\Delta_{\mathrm{C}} = \omega_{\mathrm{L}} - \omega_{\mathrm{C}}$ is the frequency difference between the input laser and the cavity field. The coupling between the two $\hat{X}$ quadratures introduces two processes. One is the Stokes process, where a photon from the laser is scattered to a photon with a lower frequency and a photon. Another one is the anti-Stokes process, where a drive photon absorbs a phonon and it is scattered into a photon with a higher frequency.[22] In a sideband-resolved system, depending on the detuning, one process is suppressed by the optical cavity. The asymmetry of these two processes are used in ground-state cooling of the mechanical resonator [48] and entanglement generation and readout [46]. However, in a sideband-unresolved system, the two scattering processes happen at a similar rate. Thus, a single sideband-unresolved system is not compatible to many works based on this idea.[29, 31]

The mechanical resonator and the optical cavity couples to the environment through their loss channels. For the optics, we consider a cavity where the reflection is measured. The resonance frequency is much larger than $k_{\mathrm{B}}T/h$ (k_{B} is the Boltzmann constant and h is the Planck's constant), as optical photons is used. This gives a thermal occupation of 0. The optical cavity contains two loss channels. The extrinsic loss with a rate κ_{e} couples to the drive $\hat{u}_{\mathrm{C}}^{\mathrm{in,e}}$. For a constant drive, the intrinsic field is simplify a vacuum field for the linearized dynamics. They have the commutation relation $[\hat{u}_{\mathrm{C},i}^{\mathrm{in,e}}(t), \hat{u}_{\mathrm{C},j}^{\mathrm{in,e}}(t')] = \mathrm{i}\varepsilon_{ij}\delta(t - t')$. The intrinsic loss with a rate $\kappa_{\mathrm{C}}^{(\mathrm{i})}$, including all the other losses such as scattering and material absorption, couples to a vacuum filed $\hat{u}_{\mathrm{C}}^{\mathrm{in,i}}$. The two channels give the total decay of the optical cavity, $\kappa_{\mathrm{C}} = \kappa_{\mathrm{C}}^{(\mathrm{e})} + \kappa_{\mathrm{C}}^{(\mathrm{i})}$. The mechanical resonator oscillates at a low frequency and it couples to a bath having a large number of excitations (phonons) n_{th}. In a typical experiment in the sideband-unresolved regime, $n_{\mathrm{th}} \approx \frac{k_{\mathrm{B}}T}{\hbar\Omega_{\mathrm{M}}} \gg 1$ and the mechanical quality factor Q_{M} is high. The bath only couples to the momentum quadrature of the harmonic oscillator and it is approximately Markovian, $\hat{u}_{\mathrm{M}}^{\mathrm{in}} = (0, \hat{Y}_{\mathrm{M}}^{\mathrm{in}})$, with $\langle \hat{Y}_{\mathrm{M}}^{\mathrm{in}}(t)\hat{Y}_{\mathrm{M}}^{\mathrm{in}}(t') + \hat{Y}_{\mathrm{M}}^{\mathrm{in}}(t')\hat{Y}_{\mathrm{M}}^{\mathrm{in}}(t)\rangle \approx (n_{\mathrm{th}} + 1/2)\delta(t - t')$. [79] The linearized dynamics

of the system follows the Quantum Langevin equation [23, 79]

$$\begin{aligned}
\dot{\hat{X}}_{\mathrm{C}} &= -\frac{\kappa_{\mathrm{C}}}{2}\hat{X}_{\mathrm{C}} - \Delta_{\mathrm{C}}\hat{Y}_{\mathrm{C}} + \sqrt{\kappa_{\mathrm{C}}^{(\mathrm{e})}}\hat{X}_{\mathrm{C}}^{\mathrm{in,e}} + \sqrt{\kappa_{\mathrm{C}}^{(\mathrm{i})}}\hat{X}_{\mathrm{C}}^{\mathrm{in,i}},\\
\dot{\hat{Y}}_{\mathrm{C}} &= \Delta_{\mathrm{C}}\hat{X}_{\mathrm{C}} - \frac{\kappa_{\mathrm{C}}}{2}\hat{Y}_{\mathrm{C}} - 2gX_{\mathrm{M}} + \sqrt{\kappa_{\mathrm{C}}^{(\mathrm{e})}}\hat{Y}_{\mathrm{C}}^{\mathrm{in,e}} + \sqrt{\kappa_{\mathrm{C}}^{(\mathrm{i})}}\hat{Y}_{\mathrm{C}}^{\mathrm{in,i}},\\
\dot{\hat{X}}_{\mathrm{M}} &= \Omega_{\mathrm{M}}\hat{Y}_{\mathrm{M}},\\
\dot{\hat{Y}}_{\mathrm{M}} &= -\Omega_{\mathrm{M}}\hat{X}_{\mathrm{M}} - \Gamma_{\mathrm{M}}Y_{\mathrm{M}} - 2gX_{\mathrm{C}} + \sqrt{2\Gamma_{\mathrm{M}}}\hat{Y}_{\mathrm{M}}^{\mathrm{in}},
\end{aligned} \tag{5.2}$$

with an output of the optical field

$$\hat{u}_{\mathrm{C}}^{\mathrm{out}} = \hat{u}_{\mathrm{C}}^{\mathrm{in,e}} - \sqrt{\kappa_{\mathrm{C}}^{(\mathrm{e})}}u_{\mathrm{C}}. \tag{5.3}$$

Experimentally, when a reflection measurement scheme [22] is used, only the light couples back to the input channel could be collected and hence the output only includes this part of light. Typically, the optomechanical cavity is treated with a single loss channel with $\kappa_{\mathrm{C}}^{(\mathrm{e})} = \kappa_{\mathrm{C}}$.[70, 79] The intrinsic loss is thought to be as part of an inefficient in detection. However, we will see in section 5.5.1 that it is not sufficient to describe the system with coherent feedback.

5.3. Coherent feedback with linear optical elements

A coherent feedback loop can change the dynamics of a system significantly.[99–104] Work has been done on many systems, including sideband-resolved optomechanical cavity[105, 106], directly coupled cavities[107, 108], and hybrid systems such as those involving atoms[109]. They have shown promising results. Here, we consider the scheme where the optomechancial cavity is connected to either an external optical cavity or a mirror via an optical path. The scheme is shown in figure 5.1. Experimentally, the optical path might be free-space optics, optical fiber, or on-chip waveguides. The light traveling through the path acquire a single way delay τ_{s}, phase shift ϕ_{s} and the path has a single way efficiency η_{s}. We consider the situation where the delay, efficiency and phase shift is independent of time. Then, the input, output of the optomechanical cavity are related to the input, output of the auxiliary component,

$$\begin{aligned}
\hat{u}_{\mathrm{A}}^{\mathrm{in},1}(t) &= \sqrt{\eta_{\mathrm{s}}}R(\phi_{\mathrm{s}})\hat{u}_{\mathrm{C}}^{\mathrm{out}}(t-\tau_{\mathrm{s}}) + \sqrt{1-\eta_{\mathrm{s}}}\hat{u}_{\mathrm{fw}}^{\mathrm{in}}(t),\\
\hat{u}_{\mathrm{C}}^{\mathrm{in}}(t) &= \sqrt{\eta_{\mathrm{s}}}R(\phi_{\mathrm{s}})\hat{u}_{\mathrm{A}}^{\mathrm{out},1}(t-\tau_{\mathrm{s}}) + \sqrt{1-\eta_{\mathrm{s}}}\hat{u}_{\mathrm{bw}}^{\mathrm{in}}(t).
\end{aligned} \tag{5.4}$$

$\hat{u}_{\mathrm{fw}}^{\mathrm{in}}$ and $\hat{u}_{\mathrm{bw}}^{\mathrm{in}}$ are the input vacuum due to the dissipation on the optical connection. R is a rotational matrix,

$$R(\phi) = \begin{pmatrix} \cos\phi & \sin\phi \\ -\sin\phi & \cos\phi \end{pmatrix}, \tag{5.5}$$

due to the phase acquired in the optical path. The auxiliary component in general has two sides, with channel 1 coupling to the optomechanical system, and channel

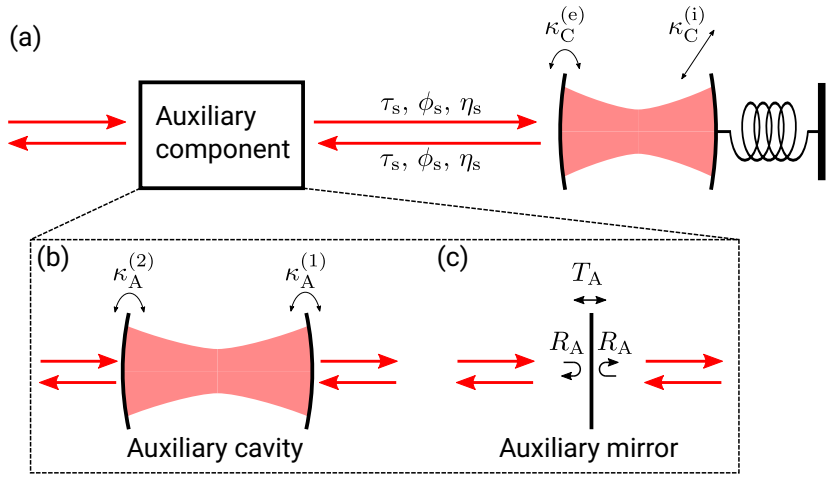

Figure 5.1: (a) Coherent feedback scheme. The optomechanical cavity, with an intrinsic loss $\kappa_C^{(i)}$ and an external coupling $\kappa_C^{(e)}$, is connected an auxiliary component via an optical path. The output light from the optomechanical cavity couples to the auxiliary component, and then it travels back to the optomechanical cavity. It forms a feedback loop. The optical path introduces a single-way delay of τ_s, phase ϕ_s, and it has a single-way efficiency of η_s. On the left, it can be used as a channel to couple driving laser into the feedback system and to perform measurements. We consider (b) an auxiliary cavity or (c) an auxiliary mirror for the auxiliary component in this work. The auxiliary cavity has a coupling of $\kappa_A^{(1)}$ to the internal feedback optical path and $\kappa_A^{(2)}$ to the outside. The auxiliary mirror has a reflectivity of R_A.

2 coupling to the outside such as for the driving and the readout. With a constant drive or without a drive from channel 2, the input $\hat{u}_A^{\text{in},2}$ is simplify a vacuum field.

In this work, we will mostly focus on using an optical cavity as the auxiliary component, where the intracavity field is denoted as $\hat{u}_A = (\hat{X}_A,\ \hat{Y}_A)$. Then,

$$\begin{aligned}\dot{\hat{X}}_A &= -\frac{\kappa_A}{2}\hat{X}_A - \Delta_A\hat{Y}_A + \sqrt{\kappa_A^{(1)}}\hat{X}_A^{\text{in},1} + \sqrt{\kappa_A^{(2)}}\hat{X}_A^{\text{in},2},\\ \dot{\hat{Y}}_A &= \Delta_A\hat{X}_A - \frac{\kappa_A}{2}\hat{Y}_A + \sqrt{\kappa_A^{(1)}}\hat{Y}_A^{\text{in},1} + \sqrt{\kappa_A^{(2)}}\hat{Y}_A^{\text{in},2},\end{aligned} \tag{5.6}$$

where $\kappa_A^{(1)}$ and $\kappa_A^{(2)}$ are loss, or coupling, to the right and left channels. The output on both sides are given by the input-output relation [22]

$$\hat{u}_A^{\text{out},k} = \hat{u}_A^{\text{in},k} - \sqrt{\kappa_A^{(k)}}\hat{u}_A, \tag{5.7}$$

where $k \in (1, 2)$ denotes the index of the coupling channel.

For the coherent feedback cooling in section 5.5.2, we also consider the scheme where a mirror with a reflectivity R_A is used as the coherent feedback component. In this case, there is no addition fields with a time derivative and the output is directly given by the input

$$\hat{u}_A^{\text{out},1} = \sqrt{R_A}u_A^{\text{in},1} + \sqrt{1-R_A}u_A^{\text{in},2}. \tag{5.8}$$

Here, we drop an added phase from the reflection. Any additional phases can be included into phase of the optical path ϕ_s.

Combining the dynamics in the system, we reach a Langevin equation of the form,

$$\dot{\hat{u}}(t) + D\dot{\hat{u}}(t-\tau) = A_0\hat{u}(t) + A_1 u(t-\tau) + \sum_{n=0}^{2} C_n \hat{u}_{in}(t - n\tau_s). \tag{5.9}$$

All the localized fields are included in $\hat{u}$, and all the input fields are included in $\hat{u}_{in}$. For example, for the coherent feedback with an auxiliary cavity, we can write $\hat{u} = (\hat{X}_M,\ \hat{Y}_M,\ \hat{X}_C,\ \hat{Y}_C,\ \hat{X}_A,\ \hat{Y}_A)^T$. The delay τ depends on the scheme. For the coherent feedback with mirror, $\tau = \tau_s$. For the scheme with an auxiliary cavity, $\tau = 2\tau_s$. We, however, do not need to distinguish the two schemes for the input noise term.

5.4. Static state dynamics

5.4.1. Dynamics with delay for steady state

Equation 5.9 is a delayed differential equation of the neutral type [110] when D, A_1, C_1 and C_2 are non-zero. In this work, only coherent feedback cooling is analyzed with delay, where the laser drive and the internal parameters are all constant. It allows transforming equation 5.9 to the Fourier domain,

$$-\mathrm{i}\omega\left(I + De^{\mathrm{i}\omega\tau}\right)\hat{u}(\omega) = \left(A_0 + A_1 e^{\mathrm{i}\omega\tau}\right)\hat{u}(\omega) + \left(\sum_{n=0}^{2} C_n e^{in\omega\tau_s}\right)\hat{u}_{in}(\omega), \tag{5.10}$$

where I is the identity matrix, and the Fourier transform is defined as

$$\mathcal{F}[\hat{u}(t)](\omega) = \int_{-\infty}^{+\infty} \hat{u}(t)e^{\mathrm{i}\omega t}\mathrm{d}t. \tag{5.11}$$

Rearranging equation 5.10 yields

$$\hat{u}(\omega) = M(\omega)\hat{u}_{in}(\omega), \tag{5.12}$$

where the transfer matrix

$$M(\omega) = -\left(\mathrm{i}\omega\left(I + De^{\mathrm{i}\omega\tau}\right) + A_0 + A_1 e^{\mathrm{i}\omega\tau}\right)^{-1}\left(\sum_{n=0}^{2} C_n e^{in\omega\tau_s}\right). \tag{5.13}$$

The input noise has a single-side spectrum [70]

$$\begin{aligned} S_{u_{in_i}}(\omega) &= 1, \\ S_{X_M^{in}}(\omega) &= S_{Y_M^{in}}(\omega) = 2n_{th} + 1, \end{aligned} \tag{5.14}$$

where u_{in_i} are for the elements corresponding to the optical input noise only. It is then possible to get the spectrum of $\hat{u}$,[70]

$$S_u(\omega) = \left|M(\omega)\right|^2 S_{u_{\mathrm{in}}}. \tag{5.15}$$

The absolute value and the square are performed entry-wise. The average phonon occupancy can be derived by integrating the spectrum of the mechanical field, [70]

$$n_{\mathrm{phn}} = \frac{1}{2}\left(\int_0^\infty \frac{d\omega}{2\pi}\left(S_{X_{\mathrm{M}}}(\omega) + S_{Y_{\mathrm{M}}}(\omega)\right)\right) - \frac{1}{2}. \tag{5.16}$$

Note that the above scheme is valid only when the system is stable. Determining the stability of the system can be done purely classically. A stable system means that all the poles of the corresponding transfer function in equation 5.15 are in the lower-half plane in the Fourier domain, or in the left-half plane in the Laplace domain. For a system without delay, i.e., $D = A_1 = C_1 = D_2 = 0$, the real part of all the eigenvalues of the matrix A_0 should be negative. [111, 112] For a system with delay, the exponential term $\mathrm{e}^{\mathrm{i}\omega\tau}$ introduces infinity poles to the system. It makes it very different from a system without delay and it is more challenging to test the stability. In our case, only a single delay parameter presents and the method performing the stability test is established in control theory. We follow the scheme described in [110, 113], and details are described in section 5.7.2.

5.5. Results

In this section, I provide some results for a system with coherent feedback. Especially, we are interested in an optomechanical system in the sideband-unresolved regime, which is relevant for many integrated optomechanical systems with low-frequency mechanical resonators[8, 32, 40, 47, 86, 96, 97] (and see chapter 4). We demonstrate, under specific condition with an auxiliary cavity, that the effective dynamics of the system is similar to a single optomechanical cavity. By introducing an auxliary cavity with a narrow bandwidth $\kappa_{\mathrm{A}} < \Omega_{\mathrm{M}}$, we can effectively bring the system into a sideband-resolved regime. A coherent feedback system has more parameters to tune, allowing further optimizations. We also study the performance when a coherent feedback is used in reducing the energy of the mechanical motion. Cooling its motion to close to the ground state is possible with a large quantum cooperativity. Furthermore, we show that a coherent feedback scheme with auxiliary cavities without delay allows producing and verifying entanglement between the mechanical resonator and the input light.

5.5.1. Similarity of a sideband-resolved system with auxiliary cavity

In this part, we show that the linearized dynamics of a sideband-unresolved system can be made to be similar to a sideband-resolved system under practical experimental condition. Consider an optomechanical system within the deep sideband-unresolved regime, $\kappa_{\mathrm{C}} \gg \Omega_{\mathrm{M}}$. The cavity field has a dynamics that is much faster

than the dynamics of the mechanical resonator. Essentially, for the dynamics we are interested in, $\left|\langle\dot{\hat{u}}_{\mathrm{C},i}\rangle\right| \ll \left|\langle\frac{\kappa_\mathrm{C}}{2}\hat{u}_{\mathrm{C},i}\rangle\right|$. It is then possible to eliminate the derivative to cavity field by approximating an instant response to the mechanical resonator.[70, 79] Also, let $\Delta_\mathrm{C} = 0$. Then, the optical field

$$\begin{aligned}\frac{\kappa_\mathrm{C}}{2}\hat{X}_\mathrm{C} &\approx \sqrt{\kappa_\mathrm{C}^{(\mathrm{e})}}\hat{X}_\mathrm{C}^{\mathrm{in,e}} + \sqrt{\kappa_\mathrm{C}^{(\mathrm{i})}}\hat{X}_\mathrm{C}^{\mathrm{in,i}},\\ \frac{\kappa_\mathrm{C}}{2}\hat{Y}_\mathrm{C} &\approx -2gX_\mathrm{M} + \sqrt{\kappa_\mathrm{C}^{(\mathrm{e})}}\hat{Y}_\mathrm{C}^{\mathrm{in,e}} + \sqrt{\kappa_\mathrm{C}^{(\mathrm{i})}}\hat{Y}_\mathrm{C}^{\mathrm{in,i}},\end{aligned} \tag{5.17}$$

For the feedback part, let $\phi_\mathrm{s} = 0$. This can be achieved by locking the length of the feedback path. Also, we consider a short feedback path $\tau_\mathrm{s} \ll 2\pi/\Omega_\mathrm{M}$, which allow us to approximate $\tau_\mathrm{s} \approx 0$. It results in a linearized Langevin equation

$$\begin{aligned}\dot{\hat{X}}_\mathrm{A} &= \frac{\tilde{\kappa}_\mathrm{A}}{2}\hat{X}_\mathrm{A} - \Delta_\mathrm{A}\hat{Y}_\mathrm{A} + \sqrt{\tilde{\kappa}_\mathrm{A}^{(1)}}\hat{\tilde{X}}_\mathrm{A}^{\mathrm{in},1} + \sqrt{\kappa_\mathrm{A}^{(2)}}\hat{X}_\mathrm{A}^{\mathrm{in},2},\\ \dot{\hat{Y}}_\mathrm{A} &= \Delta_\mathrm{A}\hat{X}_\mathrm{A} + \frac{\tilde{\kappa}_\mathrm{A}}{2}\hat{Y}_\mathrm{A} - 2\tilde{g}\hat{Y}_\mathrm{M} + \sqrt{\tilde{\kappa}_\mathrm{A}^{(1)}}\hat{\tilde{Y}}_\mathrm{A}^{\mathrm{in},1} + \sqrt{\kappa_\mathrm{A}^{(2)}}\hat{Y}_\mathrm{A}^{\mathrm{in},2},\\ \dot{\hat{X}}_\mathrm{M} &= \Omega_\mathrm{M}\hat{Y}_\mathrm{M},\\ \dot{\hat{Y}}_\mathrm{M} &= -\Omega_\mathrm{M}\hat{X}_\mathrm{M} - \Gamma_\mathrm{M}\hat{Y}_\mathrm{M} + \sqrt{2\Gamma_\mathrm{M}}P_\mathrm{in} - 2\tilde{g}\left(\hat{X}_\mathrm{A} - \sqrt{\frac{(1-\eta_\mathrm{s})\xi_1}{\eta_\mathrm{OM}\eta_\mathrm{rt}\kappa_\mathrm{A}^{(1)}}}\hat{X}_\mathrm{add}\right),\end{aligned} \tag{5.18}$$

where $\eta_\mathrm{OM} = \kappa_\mathrm{C}^{(\mathrm{e})}/\kappa_\mathrm{C}$ and $\xi_n = 1 - \eta_\mathrm{s}^n r_\mathrm{OM}^n$ with $r_\mathrm{OM} = 1 - \frac{\kappa_\mathrm{C}^{(\mathrm{e})}}{\kappa_{\mathrm{OM}/2}}$. We have also introduced two effective fields, $\hat{\tilde{u}}_\mathrm{A}^{\mathrm{in},1} = \left(\hat{\tilde{X}}_\mathrm{A}^{\mathrm{in},1},\ \hat{\tilde{Y}}_\mathrm{A}^{\mathrm{in},1}\right)^T$ and $\hat{u}_\mathrm{add} = (\hat{X}_\mathrm{add},\ \hat{Y}_\mathrm{add})^T$,

$$\begin{aligned}\hat{\tilde{u}}_\mathrm{A}^{\mathrm{in},1} &= \frac{1}{\sqrt{\xi_2}}\left(-\frac{\sqrt{\eta_\mathrm{s}\kappa_\mathrm{C}^{(\mathrm{e})}\kappa_\mathrm{C}^{(\mathrm{i})}}}{\kappa_\mathrm{C}/2}\hat{u}_\mathrm{C}^{\mathrm{in,i}} + r_\mathrm{OM}\sqrt{\eta_\mathrm{s}(1-\eta_\mathrm{s})\hat{u}_\mathrm{bw}^{\mathrm{in}}} + \sqrt{1-\eta_\mathrm{s}}\hat{u}_\mathrm{fw}^{\mathrm{in}}\right),\\ \hat{u}_\mathrm{add} &= \sqrt{\frac{\eta_\mathrm{OM}}{(1-\eta_\mathrm{s})\xi_1}}\left((1-\eta_\mathrm{s})\sqrt{\frac{\kappa_\mathrm{C}^{(\mathrm{i})}}{\kappa_\mathrm{C}^{(\mathrm{e})}}}\hat{u}_\mathrm{C}^{\mathrm{in,i}} + \sqrt{1-\eta_\mathrm{s}}u_\mathrm{bw}^{\mathrm{in}} + \sqrt{\eta_\mathrm{s}(1-\eta_\mathrm{s})}u_\mathrm{fw}^{\mathrm{in}}\right).\end{aligned} \tag{5.19}$$

They are from the combination of the optical vacuum field, and they satisfies the Bosonic commutation relation. Equations (5.18) give a dynamics that is similar to a bare optomechanical cavity where the mechanical resonator is directly coupled to the auxiliary cavity, with modified parameters,

$$\begin{aligned}\tilde{\kappa}_\mathrm{A}^{(1)} &= \frac{\xi_2}{\xi_1^2}\kappa_\mathrm{A}^{(1)},\\ \tilde{\kappa}_\mathrm{A} &= \tilde{\kappa}_\mathrm{A}^{(1)} + \kappa_\mathrm{A}^{(2)},\\ \tilde{g} &= -\frac{\sqrt{\eta_\mathrm{s}\kappa_\mathrm{A}^{(1)}\kappa_\mathrm{C}^{(\mathrm{e})}}}{\xi_1\kappa_\mathrm{C}/2}g.\end{aligned} \tag{5.20}$$

Now, the effective optical decay rate is $\tilde{\kappa}_{\mathrm{A}}$. By using a narrow-linewidth auxiliary cavity, it brings the system into the sideband-resolved regime. Especially, with the optical cavity of the optomechanical system being overcoupled, which can be routinely achieved experimentally [40, 63], $r_{\mathrm{C}} < 0$ and $\xi_2/\xi_1^2 < 1$, $\tilde{\kappa}_{\mathrm{A}} < \kappa_{\mathrm{A}}$. The effective optical decay rate is smaller than the actual decay rate of the auxiliary, enabling even less stringent linewidth requirement over the auxiliary cavity. Experimentally, Fabry-Pérot cavities can have a much narrower linewidth than the mechanical frequencies in many integrated low-frequency optomechanical systems. They, however, might not be suitable for mechanical resonators oscillating at some high frequencies[86, 96, 97] since connecting a Fabry-Pérot cavities to an optomechanical system introduces delay. It becomes an issue when the mechanical resonance frequency is high. Within this regime, an integrated optical cavity [114, 115] is available to meet the linewidth requirement. The drastic reduction of the effective linewidth of the optical cavity allows experiments and applications originally proposed for the sideband-resolved regime. However, it comes with an expense of a reduction of the (effective) optomechanical coupling $\tilde{g}$. Also, the added noise $\hat{X}_{\mathrm{add}}$ increases the effective phonon number of the bath,

$$\tilde{n}_{\mathrm{th}} = n_{\mathrm{th}} + 4\frac{1-\eta_{\mathrm{s}}}{\xi_1}\frac{g^2}{\Gamma_{\mathrm{M}}\kappa_{\mathrm{C}}}. \tag{5.21}$$

Note that the added noise vanishes at the limit of $\eta_{\mathrm{s}} \to 1$, i.e., no loss on the optical path. It does not require a fully overcoupled optomechanical cavity ($\kappa_{\mathrm{i}} = 0$).

In an optomechanical experiment, a figure of merit is the quantum cooperativity $C_{\mathrm{qu}} = \frac{4g^2}{n_{\mathrm{th}}\kappa\Gamma_{\mathrm{M}}}$.[22] A higher value means a more robust optomechanical interaction against decoherence because it compares the interaction rate to the photon and the phonon decoherence rate. A higher value is usually more desirable. For a coherent feedback system with the effective dynamics in equation (5.18), we can write down the effective cooperativity with respect to the quantum cooperativity C_{qu} of a bare optomechanical cavity,

$$\tilde{C}_{\mathrm{qu}} = \frac{4\tilde{g}^2}{\tilde{\kappa}_{\mathrm{A}}\tilde{\Gamma}_{\mathrm{M}}\tilde{n}_{\mathrm{th}}} = \frac{4\eta_{\mathrm{s}}\eta_{\mathrm{C}}(\kappa_{\mathrm{A}}^{(1)}/\kappa_{\mathrm{A}})/\xi_1^2}{\left(1+2\frac{\eta_{\mathrm{s}}r_{\mathrm{C}}}{\xi_1}\frac{\kappa_{\mathrm{A}}^{(1)}}{\kappa_{\mathrm{A}}}\right)\left(1+\frac{1-\eta_{\mathrm{s}}}{\xi_1}C_{\mathrm{qu}}\right)}C_{\mathrm{qu}}. \tag{5.22}$$

For a lossless optical path, the effective quantum cooperativity is enhanced as long as $\kappa_{\mathrm{A}}^{(1)} > \kappa_{\mathrm{A}}/2$, i.e., the auxiliary cavity is overcoupled to the optomechanical side. This is due to the fact that an overcoupled auxiliary cavity recycles photons. When the auxiliary cavity becomes undercouped, the photons can hardly get into the optical cavity. Further, once a photon is coupled into the cavity, it is more likely to exit on the other port and leave the feedback system. When both the optomechanical cavity and the auxiliary cavity are fully overcoupled and when the loss on the optial path vanishes, the enhancement diverges since photon cannot leave the system. It, however, does not correspond to a physical situation. With an inefficient feedback $\eta_{\mathrm{s}} < 1$, the enhancement would become reduction when the original quantum cooperativity is very large due to the added noise coupled from the optical path.

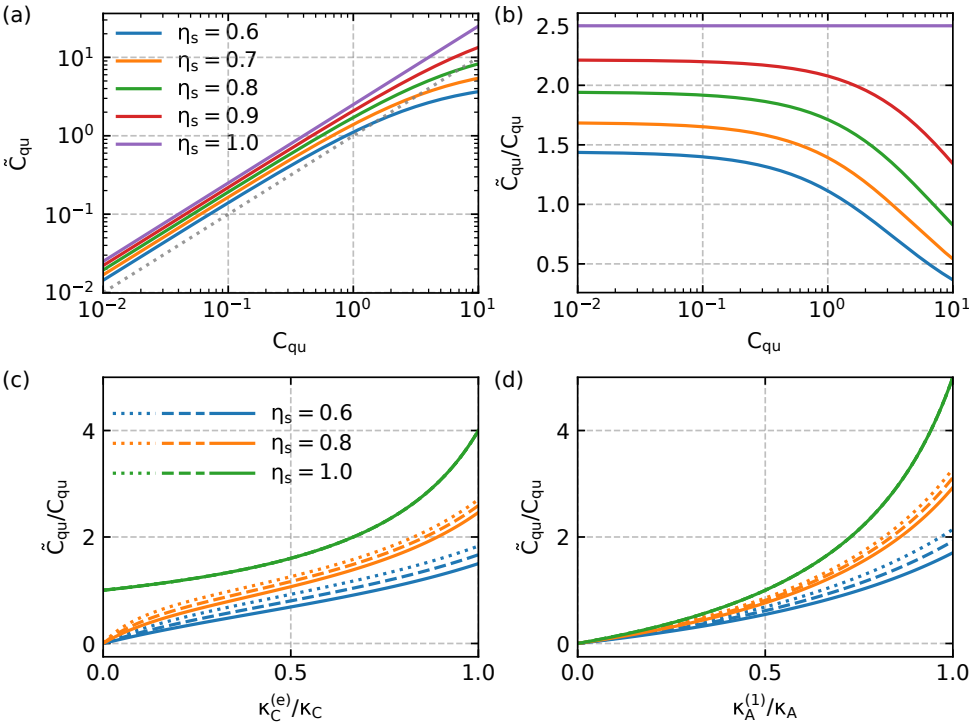

Figure 5.2: (a) Effective quantum cooperativity as a function of the original quantum cooperativity and (b) their ratio at different single-way optical path efficiency. When the original quantum cooperativity is large, the enhancement is reduced and it could become a reduction. The dotted line in (a) draws $\tilde{C}_{qu} = C_{qu}$. (c, d) The quantum cooperativity ratio as a function of the coupling of the optical cavities to the feedback system. The dotted line, dashed lines, and the solid line are for an original quantum cooperativity of 0.1, 0.5 and 1, respectively. In (c), $\kappa_C/2\pi = 10$ GHz is fixed. In (d), $\kappa_A/2\pi = 500$ kHz is fixed. Other parameters for the plot are listed in section 5.7.1.

For a set of practical parameters (section 5.7.1), the effective quantum cooperativity and the ratio between the effective and the original quantum cooperativity is shown in figure 5.2a, b. For an optical feedback path without loss, the cooperativity is enhanced by a factor of 1.5. Also, despite of the added noise, we note that the enhancement is still robust against the loss over the feedback path. With a moderate single way efficiency of 70%, the enhancement of the quantum cooperativity persists until $C_{qu} \approx 3.25$. It already allows for experiments with a relatively large quantum cooperativity. Improving the efficiency still drastically increases the enhancement region. A moderate increase of the single-way efficiency to 0.8 allows a upper bound of $C_{qu} = 6.98$, more than doubling the previous value. The results for changing the coupling efficiency $\kappa_C^{(e)}/\kappa_C$ and $\kappa_A^{(1)}/\kappa_A$ are plotted in figure 5.2c, d, where the dotted, dashed, and solid lines are for $C_{qu} = 0.1,\ 0.5,\ 1$. The total decay rate κ_A and κ_A are fixed. As expected, increasing the coupling to the internal feedback system increases the enhancement of the quantum cooperativity.

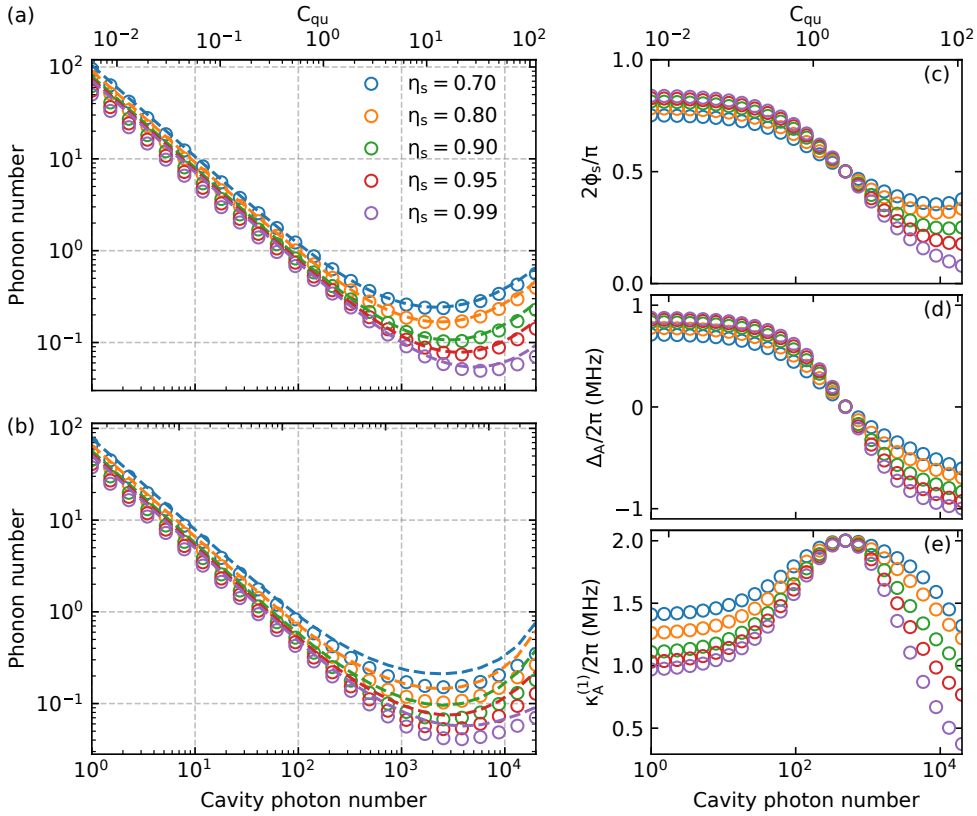

Figure 5.3: Coherent feedback cooling with an auxiliary cavity without delay. The dashed lines show the sideband cooling result for a similar optomechanical cavity (see section 5.5.1), and circles show the optimized results. (a) Only ϕ_s and Δ_A are optimization parameters and (b) ϕ_s, Δ_A and $\kappa_A^{(1)}$ are optimization parameters. The optimized parameters are plotted in (c-e).

5.5.2. Coherent feedback cooling

Preparing a mechanical resonator close to a state with low phonon occupation has attracted lots of interest[42, 78, 116, 117]. For a mechanical resonator contacting a high temperature bath, a phonon occupation below 1 has been achieved in sideband-resolved systems [48, 118] and in sideband-unresolved systems with the measurement-based feedback cooling[52]. Inspired by the similarity between a sideband-unresolved system with coherent feedback and a sideband-resolved system, we show in this section that it is possible to reduce phonon occupation with the coherent feedback scheme. With a large quantum cooperativity, ground-state cooling, where the phonon occupation is below 1, can be achieved. Further, comparing to a single optomechanical system, the coherent feedback scheme has more parameters to tune, allowing it to perform better than a similar optomechanical system described in section 5.5.1.

In figure 5.3a, we show the average phonon occupancy with the coherent feed-

back cooling, where an optomechanical system is coupled to an auxiliary cavity without delay. The phonon number is minimized numerically with respect to the phase acquired on the optical path ϕ_s and the detuning of the auxiliary cavity Δ_A. When the quantum cooperativity approaches 1, the phonon number starts to drop below 1. For a single-way efficiency of 70%, 80% and 90%, it is possible to achieve a minimum phonon number of 0.24, 0.16 and 0.10. When the quantum efficiency becomes too high, the added noise from the feedback and the back-action noise in the optomechanical system dominates and thus the phonon number increases. The sideband cooling results of an equivalent optomechanical system as discussed in 5.5.1 is shown in dashed line. They correspond to a feedback cooling where $\phi_s = 0$ and $\Delta_A = -\Omega_M$. We see that the optimized phonon number is slightly lower. The reduction is larger when the efficiency is higher. A greater benefit can be obtained when we further include $\kappa_A^{(1)}$ as an optimization parameter (figure 5.3b). Experimentally, since the auxiliary cavity is not part of the optomechanical system, it allows us to freely choose the parameters as long as it is feasible. For example, for a Fabry-Pérot cavity, it can be done by choosing the mirror coupling to the feedback system with a correct reflectivity. Here, we keep the coupling to the outer channel the same as before, $\kappa_A^{(2)}/2\pi = 100$ kHz. For a single-way efficiency of 70%, 80% and 90%, it is then possible to achieve a minimum phonon number of 0.15, 0.10 and 0.07. Clearly, it outperforms the condition of simply setting $\phi_s = 0$ and $\Delta_A = -\Omega_M$. The optimized parameters are shown in figure 5.3c-e, showing the optimal parameters being very different from simply setting $\phi_s = 0$ and $\Delta_A = -\Omega_M$. The optimal detuning is not necessarily on the red sideband due to the extra degree of freedom ϕ_s. The optimal linewidth is larger than or comparable to the mechanical frequency, resulting an auxiliary cavity that is heavily overcoupled to the feedback system. It is also interesting to note an optimal point that is fixed for different efficiencies over the feedback optical path. It occurs at roughly at 500 cavity photon ($C_{qu} \approx 2.8$), with the optimal set of parameters $\phi_s \approx \pi/4$, $\Delta_A/2\pi \approx 0$ MHz, and $\kappa_A^{(1)}/2\pi \approx 2$ MHz. Especially, $\kappa_A^{(1)}$ is significantly larger for smaller optical path efficiency, except for this point. The phonon occupancy, however, does not coincide. The reason for this fixed point is not yet understood and it may require solving the model analytically.

In a practical experiment, the optical path would introduce a delay. A delay brings incoherence to the feedback, since the feedback misses new information of the mechanical resonator. For low frequency mechanical resonator, the delay is in general small comparing to the oscillation period. Here, we stress that the delay does not introduce a significant reduction of the cooling performance if the mechanical decoherence rate is small. The decoherence has a time scale that is much longer than the feedback delay. In figure 5.4a, the cavity-assisted coherent feedback with delay is studied, where the round trip delay $2\tau_s$ is set to 0, 0.05 and 0.1 μs. They corresponds to a single-way free-space optical path of 0, 7.5, and 15 m. We do not see a noticeably higher phonon number for different delays with different η_s. The cooling performance is worse at extremely high photon number, which is already outside regime with optimal photon number.

Besides the coherent feedback with an auxiliary cavity, coherent feedback cool-

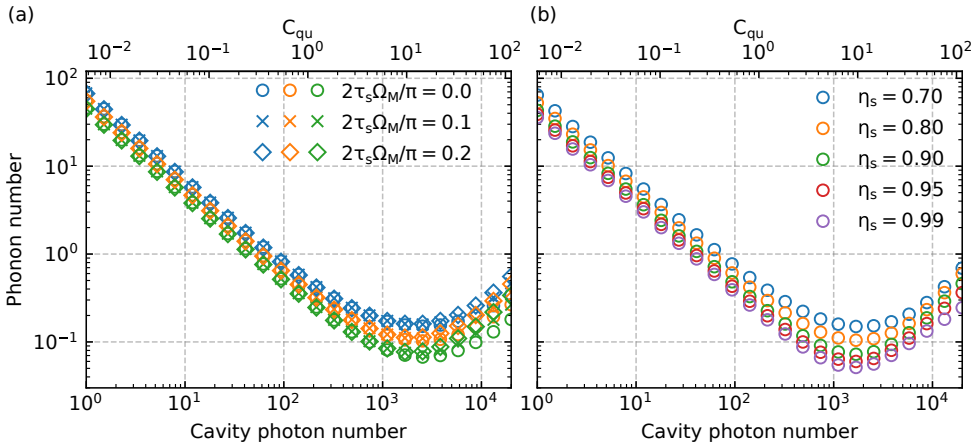

Figure 5.4: Coherent feedback with delay for (a) an auxiliary cavity and (b) an auxiliary mirror. In (a), the round trip delay are 0, 0.05 and 0.1 μs, corresponding to a feedback phase $2\Omega_M\tau_s$ of 0, 0.1π and 0.2π. The single way efficiency over the optical path is $\eta_s = 0.7,\ 0.8,\ 0.9$ for blue, orange and green curves. The phonon number is minimized numerically with respect to $\kappa_A^{(1)}$, Δ_A and ϕ_s. In (b), the reflectivity of the auxiliary mirror is set to 1. Non-unity reflectivity can be included in the optical path efficiency. The phonon number is minimized with respect to τ_s and ϕ_s.

5

ing can also be achieved by using a mirror as the feedback element (figure 5.1c) in the presence of optical delay. With a round-trip delay of around $1/4$ of the mechanical oscillation cycle, similar to the measurement-based feedback cooling[40, 117], the feedback can introduce a damping force to the mechanical resonator when ϕ_s is properly tuned. In figure 5.4b the cooling with a mirror is studied. The reflectivity of the mirror is set to be 1. Typically, a commercially available mirror can have an extremely high reflectivity (>99%). Also, any reduction in the reflectivity from unity can be included in the optical path efficiency η_s. We find a similar performance comparing to the coherent feedback by an auxiliary cavity. At large quantum cooperativity, the resulting phonon number is higher due to the larger delay which introduces more incoherent signal to the feedback. However, similar to the feedback by an optical cavity, the impact is small at the optimal quantum cooperativity. A direct comparison is plotted in figure 5.5.

We also compare the coherent feedback to the measurement-based feedback. For the measurement based feedback cooling, we adapt the results from [70] with the regime $\kappa_C \gg \omega_{fb} \sim \Omega_M \gg \Gamma_M$. ω_{fb} is the feedback bandwidth. We minimize the phonon number with respect to ω_{fb} and the feedback gain numerically. We use a detection efficiency that matches the single-way optical path efficiency, $\eta_{det} = \eta_s$. We see that, at small quantum cooperativity, the measurement-based feedback cooling is much more efficient. The weak cooling power for the coherent feedback cooling is due to the fact that there is no gain in the coherent feedback system proposed here. On the other hand, in the measurement-based feedback cooling, the gain can be tuned to reach the noise-squashing regime.[52, 119] However, at large cavity photon number, it is possible to achieve a lower phonon occupation

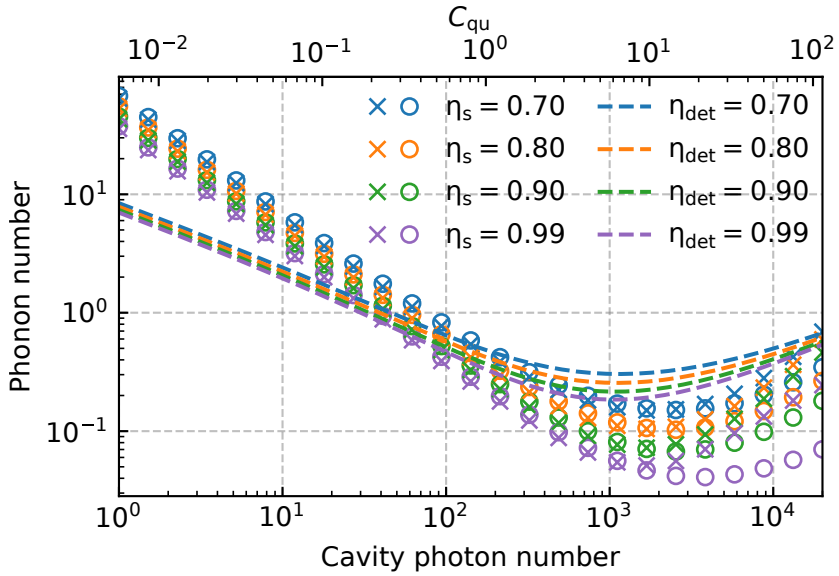

Figure 5.5: A comparison between coherent feedback by mirror (crossings, results from 5.3b), by auxiliary cavities (circles, results from 5.4b), and the from measurement-based feedback (dashed lines, results from [70]). The measurement based feedback cooling has a detection efficiency η_{det} that is equal to η_{s} of the corresponding coherent feedback case.

with the coherent feedback. When viewing from the optomechanical system, for the coherent feedback, the feedback signal coherently mixes with the input-noise. $\hat{u}_{\mathrm{C}}^{\mathrm{in}} = \sqrt{\eta}\hat{u}_{\mathrm{fb}} + \sqrt{1-\eta}\hat{u}_{\mathrm{vac}}$, where η is the efficiency for the feedback signal $\hat{u}_{\mathrm{fb}}$ coupling to the optomechanical cavity. It mixes with the vacuum noise $\hat{u}_{\mathrm{vac}}$. For the measurement-based feedback cooling, however, the feedback signal is classical. Then, $\hat{u}_{\mathrm{C}}^{\mathrm{in}} = \sqrt{\eta}u_{\mathrm{fb}} + \hat{u}_{\mathrm{vac}}$. The input noise is therefore lower in the coherent feedback case, with $0 < 1-\eta < 1$ always satisfied.

5.5.3. Entanglement generation and verification between photons and phonons

Quantum entanglement between photons and phonons has been proposed and demonstrated in optomechanical system with the sideband-resolved regime.[33] When the device is at a low-phonon occupation state, two pulses with duration longer than the mechanical resonance period is sent to the optomechanical system. The first pulse, where the laser is blue-detuned, is used to create the photon-phonon entanglement. A photon in the pulse has a probability to create a phonon and it generates a photon at a lower frequency. The later pulse is red-detuned. A photons has a probability to absorb a phonon, resulting a photon at a higher frequency. It swaps the state of the phonon into the reflected light. By measuring the reflection of the two pulses, it is then possible to infer photon-phonon entanglements if the separation of the two pulses is long enough. The two processes

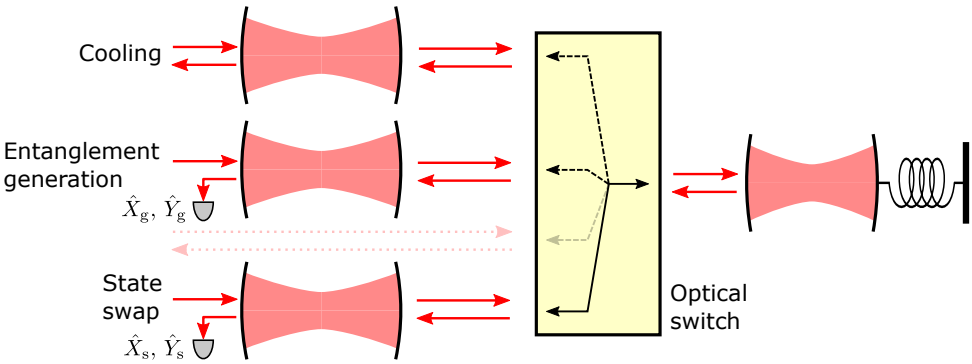

Figure 5.6: The entanglement generation and verification scheme considered in this work. The optomechanical cavity connects to three auxiliary cavities via an optical switch. The three cavities are for cooling, entanglement generation, and state-swap for entanglement verification. By measuring the output of the last two auxiliary cavities, photon-phonon entanglement can be detected. Between the entanglement generation and verification, a gap without the feedback is inserted. Optionally, as considered in this work, light from the laser is coupled into the optomechanical directly to keep a constant cavity photon number.

rely on a narrow linewidth cavity, which suppresses one of the processes during each pulse. On a sideband unresolved system, the suppression is negligible. When creating the entanglement, the state-swap process happens at a similar rate and it losses entanglement. Similarly, in the state-swap phase, it creates entanglement between the photons in the second pulse and phonons and it effectively add decoherence. It is thus challenging to detect optomechanical entanglement with this scheme. Inferring entanglement through continuous measurement inspired by the similar idea has been proposed, with a maximum squeezing of EPR quadratures reaching up to 50% of the vacuum noise.[79] In this section, we argue that it is possible to verify optomechanical through the coherent feedback scheme with auxiliary cavities. A squeezing of the EPR quadratures beyond 50% of the vacuum noise could be achieved by optimizing the mechanical quality factor with a reasonably high efficiency of the optical path.

We consider a scheme shown in figure 5.6, without any delay in the feedback. It expands the coherent feedback scheme in figure 5.1 to a setup with three cavities. With a fast optical switch, it is possible to select the auxiliary cavity coupling to the optomechanical system. Light is sent into the system through port 2 (the port connecting to the outside) of the auxiliary cavities. Firstly, the switch is set to the first cavity, which is used to pre-cool the mechanical resonator into a low thermal occupation state. For simplicity, we set $\kappa_A^{(1)}/2\pi = 400$ kHz, $\kappa_A^{(2)}/2\pi = 100$ kHz, $\Delta_A = -1$ MHz, and $\phi_s = 0$ though out the calculation. We set an interaction time of 0.1 second in our calculation, which is sufficient to reach a steady state. Then, it switches to the second cavity, which is for the entanglement generation. Finally, it switches to the third cavity, performing state-swap for reading the state of the mechanics. We assume a switching time of 100 ns between the entanglement generation and the state-swap phase, during which there is no feedback (shown as

an empty channel with dotted optical lines in figure 5.6). It expands the scheme in [33]. By introducing the dark switching time which is much larger than $1/\kappa_{\mathrm{C}}$, the entanglement generation cavity and the state-swap cavity are effectively isolated. The light carrying information during the entanglement generation cannot be detected by the state-swap measurement. Optomechanical entanglement can thus be verified by measuring the X and Y quadratures of the output of the two cavities.

We calculate the entanglement through solving the linearized dynamics described by equation 5.9, with $D = A_1 = C_1 = 0$. The calculation routine is similar to that in reference [120], but without the use of the rotating wave approximation (RWA). The evolution of the system is of the form

$$\hat{u}(t) = \exp(A_0 t)\hat{u}(t_0) + \int_{t_0}^{t} \mathrm{d}s \exp\left(A_0(t_0 - s)\right) C_0 \hat{u}_{\mathrm{in}}(s). \tag{5.23}$$

For t being in different phases (pre-cooling, entanglement generation, switching, state-swap), t_0 represents the starting of the corresponding phase. With this setting, A_0 and C_0 are constant. The output of the auxiliary cavities, for the entanglement generation and verification, are then defined,

$$\hat{u}_\alpha = u_{\mathrm{A},\alpha}^{\mathrm{in},2} - \sqrt{\kappa_{\mathrm{A},\alpha}} u_{\mathrm{A},\alpha}. \tag{5.24}$$

$\alpha \in \{\mathrm{g}, \mathrm{s}\}$ denotes the components involved in the entanglement generation and the state-swap phase. Further, we define optical temporal modes [33, 79]

$$\hat{r}_\alpha = \int_{t_0}^{t_f} \mathrm{d}t f_\alpha(t) R(\theta_\alpha(t)) \hat{u}_\alpha. \tag{5.25}$$

The integration is carried out only within the corresponding phase, starting from t_0 and ending at t_f. R is the rotation matrix defined in equation 5.5, with $\theta_{\mathrm{g}}(t) = \Omega_{\mathrm{M}} t$ and $\theta_{\mathrm{s}}(t) = -\Omega_{\mathrm{M}} t + \phi_{\mathrm{s}}$. The rotation matrix is necessary since we do not use the RWA in order to handle the sidebnd-unresolved regime. Also, we take the exponential form of for the envelope f_α [33, 79],

$$\begin{aligned} f_{\mathrm{g}}(t) &= \left(\frac{1 - \mathrm{e}^{-2\Gamma_{\mathrm{tm}}\tau_{\mathrm{p}}}}{2\Gamma_{\mathrm{tm}}}\right)^{1/2} \mathrm{e}^{\Gamma_{\mathrm{tm}}(t - t_{\mathrm{g}}^{(\mathrm{f})})}, \\ f_{\mathrm{s}}(t) &= \left(\frac{1 - \mathrm{e}^{-2\Gamma_{\mathrm{tm}}\tau_{\mathrm{p}}}}{2\Gamma_{\mathrm{tm}}}\right)^{1/2} \mathrm{e}^{-\Gamma_{\mathrm{tm}}(t - t_{\mathrm{g}}^{(0)})}. \end{aligned} \tag{5.26}$$

$t_{\mathrm{g}}^{(\mathrm{f})}$ is the end time of the entanglement generation, and $t_{\mathrm{g}}^{(0)}$ is the starting time of the state-swap process. Both have a duration of τ_{p}. Outside the period they are equal to 0. This definition ensures that the temporal mode $\hat{r}$ satisfies the bosonic commutation relation, $[\hat{r}_{\alpha,i},\ \hat{r}_{\beta,j}] = \delta_{\alpha\beta}\epsilon_{ij}$, where $i, j \in \{X, Y\}$ are for the two quadratures included in $\hat{r}$. The covariance matrix of the temporal mode can then be evaluated

$$\sigma_{ij} = \langle \hat{r}_i \hat{r}_j + \hat{r}_j \hat{r}_i \rangle, \tag{5.27}$$

with $\hat{r} = (\hat{r}_{g,X}, \hat{r}_{g,Y}, \hat{r}_{s,X}, \hat{r}_{s,Y})$. In this work, we use the EPR-variance to quantify the entanglement, $\Delta_{\mathrm{EPR}} = (\sigma_{11} + \sigma_{22} + \sigma_{33} + \sigma_{44})/2 + (\sigma_{13} - \sigma_{24})$. [79]

We further note that a switching with dark time might introduce classical noise to the mechanical resonator due to the resulting change in the cavity photon number. It thus reduces the entanglement and it is not captured by the linearized model.[121] It is more relevant to the calculation here, because the mechanical oscillation considered here is significantly less coherent comparing to the typical optomechanical experiments in the sideband-resolved regime.[21, 42] For the case here, a higher interaction strength with a shorter pulse is favorable, as demonstrated below. However, we stress that the switching time considered here is much shorter than the mechanical oscillation period and thus the disturbance would mainly be at very high frequency. The impact to the mechanical resonator is minimized. Furthermore, in this work, we opt to take a more conservative approach. We assume an unchanged average photon numbers inside the optomechanical cavity and it eliminates the effect of the switching. Experimentally, this can be done by introducing another coupling channel, such as another waveguide into the optomechanical system. Alternatively, note that many on-chip optical switches do not block light[122–124], an additional channel on the optical switch that couples to the laser directly can be introduced. It is included in the scheme in figure 5.6, shown as the dotted red lines for the optics and the faded dashed line inside the switch. By controlling the light intensity on this additional channel, it is then possible to achieve a constant cavity photon number. This approach reduces entanglement since the photons during the switching are not measured, corresponding to a loss of information. The photons also interact with the mechanical resonator, creating decoherence. Therefore, we choose a switch with a short switching time. We note that on-chip optical switches with low loss and a much smaller switching time has been demonstrated.[122, 125] For a more optimal configuration, models capturing the full dynamics might be required.[121] Other potential solutions include further reducing the bath temperature or developing mechanical resonator with higher $Q_{\mathrm{M}} \times f_{\mathrm{M}}$. Both reduce decoherence and hence allow longer pulses.

In the scheme considered here, the auxiliary cavities for entanglement generation and verification have the same parameters, except for an opposite detuning. The phases of the optical paths ϕ_{s} for both stages also have opposite signs. We then minimize Δ_{EPR} with respect to $\kappa_{\mathrm{A}}^{(1)}$, $\kappa_{\mathrm{A}}^{(2)}$, Δ_{A}, ϕ_{s}, Γ_{tm} and τ_{p}. Different from the feedback cooling, we include $\kappa_{\mathrm{A}}^{(2)}$ as an optimization parameter since the entanglement is detected from the output light of channel 2. The result is plotted in figure 5.7, with a unity detection efficiency for the light getting out of the feedback system. We consider mechanical resonator with $Q_{\mathrm{M}} = 2 \times 10^7$ and 10^8. They correspond to a thermal decoherence rate, in the unit of mechanical resonance cycles $Q_{\mathrm{M}} f_{\mathrm{M}}/(k_{\mathrm{B}} T/h)$, of 230 and 1100. The details of the optimized parameters are shown in the appendix (section 5.7.3). When increasing the cavity photon number, Δ_{EPR} first drops, and then increases. The increase is probably due to a fast heat-up and cooling rate from the two pulses, resulting a short pulse and large Γ_{M}. Also, in the present of optical loss in the feedback, additional noise would also couple in and introduces decoherence. Nevertheless, for a single-way efficiency of 0.7, 0.8 and

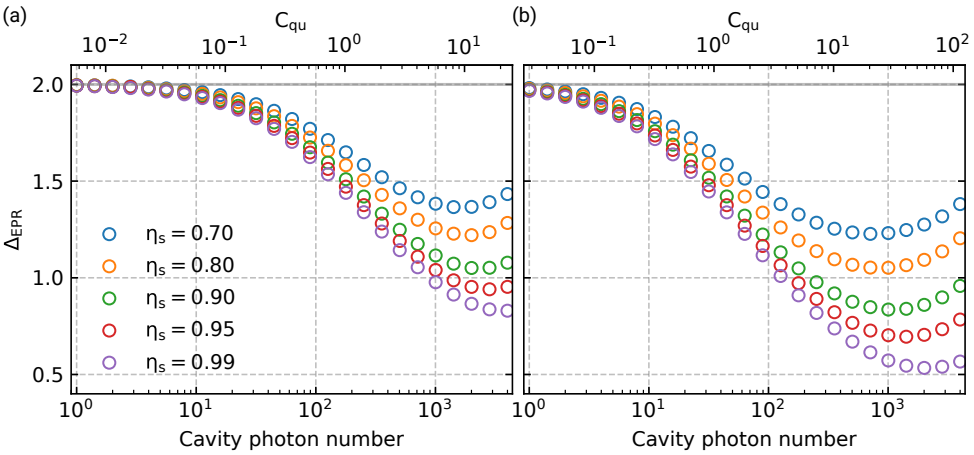

Figure 5.7: Optimized Δ_{EPR} for (a) $Q_{\mathrm{M}} = 2 \times 10^7$ and (b) $Q_{\mathrm{M}} = 10^8$. The gray solid line shows the separability bound $\Delta_{\mathrm{EPR}} = 2$.

5

0.9, it is possible to achieve a Δ_{EPR} of 1.37, 1.22 and 1.05 with $Q_{\mathrm{M}} = 2 \times 10^7$, and 1.23, 1.05 and 0.84 with $Q_{\mathrm{M}} = 10^8$. $\Delta_{\mathrm{EPR}} < 2$ shows that there is entanglement between the temporal modes of the two output light pulses. It then witnesses the entanglement between the photons and the motion of the mechanical resonator. The calculation shows that it is beneficial to achieve low loss over the feedback path and a low thermal decoherence. However, it is still remarkably robust against any dissipation in the system, making it feasible in experiment. In figure 5.8 the optimized linewidth for the auxiliary cavity is shown, with an optimal $\kappa_{\mathrm{A}}^{(2)}/2\pi$ around 500 kHz. We note that a total linewidth of 220 kHz has been reported recently by on-chip disk resonators[114], a fully integrated coherent feedback system might be achievable and it is beneficial in reducing optical loss over the feedback path. A reasonable increase of the mechanical frequency would also make a fully integrated system more feasible.

5.6. Conclusion and outlook

In this work, we propose a coherent feedback scheme with linear, passive optical components. We mainly consider optomechanical systems in the deep sideband-unresolved regime, and some experimentally relevant parameters. We show that an additional optical cavity can effectively bring the optomechanical system into a sideband-resolved regime for a specific set of parameters ($\phi_{\mathrm{s}} = 0$, $\tau_{\mathrm{s}} = 0$, $\Delta_{\mathrm{C}} = 0$). A non-unity feedback efficiency introduces noise to the mechanical resonator. Overall, the effective quantum cooperativity can be enhanced, depending on the path efficiency and the original quantum cooperativity. This analysis shows that it is promising to broaden the usage of a sideband-unresolved system. We then consider using either an optical cavity or a mirror plus an optical path with significant delay as an auxiliary to perform cooling of the mechanical resonator. We show

that ground state cooling is achievable under practical experimental conditions. For feedback cooling with auxiliary optical cavity without delay, the choice of $\phi_s = 0$, $\tau_s = 0$ analyzed in the first part does not yield the optimal result. Further improvements can be done by adjusting these parameters. Finally, based on the protocal to generate and verify entanglement via long pulses[33], we propose an experiment scheme using three auxiliary cavities for cooling, entanglement generation and verification. By switching among the cavities in order and allowing a small time gap without feedback between the later two cavities, we argue that the output light detects photon-phonon entanglement. We quantify the entanglement of the output light by evaluating the EPR-variance of the temporal optical mode. Though it is not necessary the optimal optimal witness to detect entanglement[79, 126] and the scheme considered here is also not optimal, it still shows a significant squeezing comparing to the inseparability bound. Finally, we would like to mention that a fully integrated on-chip coherent feedback structure is within the reach of the state-of-the-art on-chip optical resonators[114, 115] even with the mechanical frequency as low as 1 MHz. Such an integrated structure would drastically reduce the complexity of an experiment and it is beneficial in potential applications.

5.7. Appendix

5.7.1. Default parameters in this work

We consider the following parameters in the calculations though out this chapter if not specified.

Mechanical frequency $\Omega_M/2\pi$	1 MHz
Mechanical quality factor $Q_M = \Omega_M/\Gamma_M$	2×10^7
Energy decay rate of optomechanical cavity κ_C	$2\pi \times 10$ GHz
Detuning of the optomechanical cavity Δ_C	0
Coupling efficiency of optomechanical cavity $\eta_C = \kappa_C^{(e)}/\kappa_C$	0.8
Coupling rate of auxiliary cavity to the feedback $\kappa_A^{(1)}$	$2\pi \times 400$ kHz
Coupling rate of auxiliary cavity to other channels $\kappa_A^{(2)}$	$2\pi \times 100$ kHz
Environment temperature T	4.2 K
Delay (only for the feedback by auxiliary cavity) τ_s	0

They are inspired by the recent developments of high-Q mechanical resonators with high stress Silicon Nitride the integration into an cavity optomechanical device (see chapter 4).

5.7.2. Stability test with delay

As mentioned in the main text, a system with delay possesses infinity poles, and it makes it more challenging to do a rigorous stability testing. In our specific case, where only one delay for the internal system[1] presents, methods have been established.[110, 113] We follow the scheme in the two references, with details

[1] Number of delays of the input noise part is not included in the stability analysis.

described as below. In this part, we work on the Laplace space.

We consider the neutral delayed differential equation 5.9 in the classical regime and without the explicitly driving,

$$\dot{u}(t) + D\dot{u}(t-\tau) = A_0 u(t) + A_1 u(t-\tau). \tag{5.28}$$

By performing laplace transform with the complex variable s,

$$\begin{aligned}(I + De^{-s\tau})su(s) &= (A_0 + A_1 e^{-s\tau})u(s),\\ ((sI - A_0) + (sD - A_1)e^{-s\tau})\,u(s) &= 0.\end{aligned} \tag{5.29}$$

For a system being stable, all the poles of the transfer function corresponding to equation 5.29 should be on the left-half plane. Equivalently, all the poles of the polynomial

$$\det\ ((sI - A_0) + (sD - A_1)e^{-s\tau}) \tag{5.30}$$

should only have zeros on the left-half plane.

5

When continuously changing the delay of the system, the locations of the poles moves. The system might switch from a stable system to an unstable one or vice versa. However, there are only finite number of points on the imaginary axis where the poles can cross for all $\tau > 0$.[110] We first determine these points. For $\max\ |\mathrm{eig}\ D| < 1$, where eig is for the all the eigenvalues and this relation always holds in this work, the poles can be found by first constructing the two matrices,[110]

$$\begin{aligned}E_0 &= \begin{pmatrix} I \otimes I & D \otimes I \\ I \otimes D & I \otimes I \end{pmatrix},\\ J_0 &= \begin{pmatrix} A_0 \otimes I & A_1 \otimes I \\ -I \otimes A_1 & -I \otimes A_0 \end{pmatrix},\end{aligned} \tag{5.31}$$

The matrix I is the identity matrix and I, D A_0 and A_1 have the same dimension. $\otimes$ is the Kronecker product. It is shown in [110] that the poles of the equation 5.28, when exactly on the imaginary axis, are included in the zeros of the polynomial

$$\det\ (sE_0 - J_0). \tag{5.32}$$

All the zeros of the polynomial can be computed by calculating the generalized eigenvalue problem $\mathrm{eig}(J_0, E_0) = \mathrm{eig}\ (E_0^{-1} J_0)$. Those that are not purely imaginary are dropped since they do not correspond to the imaginary poles. Still, not all the eigenvalues are the imaginary zeros of equation (5.30). More importantly, the polynomial 5.32 contains no information about the delay τ. It is due to the periodicity of $e^{s\tau}$ for a purely imaginary $s = -i\omega$. Since all the possible purely imaginary s where the polynomial 5.30 is singular is contained in the zeros of 5.32, it is then straight forward to find all the s and the corresponding set of τ that makes the polynomial 5.30 singular. Substitute s by each of the remaining eigenvalues $\mathrm{eig}(J_0, E_0)$, if there is a set of real τ being the solution of $\det\ ((sI - A_0) + (sD - A_1)e^{-s\tau}) = 0$, the pair $(s, \{\tau\})$ corresponds to imaginary poles of the system 5.29. Note the periodicity of τ, with a period $2\pi/|s|$. By repeating the process for all the remaining

$\mathrm{eig}(J_0, E_0) = \mathrm{eig}\,(E_0^{-1}J_0)$, all the pairs $(s_k, \{\tau\}_k)$ are found. k is an index differentiating different zeros of 5.30.

Finding all the imaginary poles of the system 5.29 does not reveal whether the system is stable. However, it is useful to monitor whether there is a pole crossing the imaginary axis when continuously changing the delay.[113] Since it is straight forward to calculate all the poles of the system with vanishing delay (it can be done by calculating the eigenvalues of $(I + D)^{-1}(A_0 + A_1)$), it is then possible to test whether a system is stable with some arbitrary delay τ by tracing the number of poles crossing the imaginary axis and their direction. For a given finite τ, the number of possible delays where a pole crosses is finite and the values are determined in the previous paragraph. This forms a series of τ_{kl}, where l is for index the element in τ_k. We follow the procedure described in [113] to see how the zeros behaves around τ_{kl} by checking the "root tendency"

$$\mathrm{RT}_{kl} = \mathrm{sgn}\ \mathrm{Re}\left(\frac{\mathrm{d}s}{\mathrm{d}\tau}\right)_{s=s_k,\ \tau=\tau_{kl}} \tag{5.33}$$

It basically calculates the direction of the zeros move when changing τ at the vicinity of τ_{kl}. Since we are only interested in the direction a zero crosses the imaginary axis, only the real part is considered. We can then count how many zeros there are in the right-half plane, starting from $\tau = 0$. For $\mathrm{RT}_{kl} = 1$ or -1, 2 more zeros are added to or subtracted from the right-half plane. We don't consider the case where the zero crosses at $s = 0$. This process requires calculating all the $\tau_{kl} \leq \tau$, where τ is the delay of interest. In the range including τ, if there is no zero of the polynomial 5.30 in the right-half plane, the system is stable.

For a final remark for the stability test, as described in [113], more details have to be considered. These include the requirement that the spectral radius of matrix D is strictly smaller than 1 and the τ-stability for the number of unstable zeros around $\mathrm{e}^{\tau s} = \pm 1$. We refer readers to the original paper [113] for the details. While the first requirement is necessary, we take a conservative test by requiring both to be satisfied in this work.

5.7.3. Supplementary plots to the optomechanical entanglement

The optimized parameters are shown in figure 5.8. At small photon number, the optomechanical interaction is too weak, and changing the parameters does not significantly alter Δ_{EPR}. Thus, the optimizations do not converge well. Trends of the parameters is are more clear for larger photon numbers. For very large photon number, the pulses become short due to the fast heating and cooling. Further, $Q = 2 \times 10^7$ in general require a shorter pulse and larger Γ_{tm} due to the larger thermal decoherence rate. In the optimization, there is a trade-off about $\kappa_{\mathrm{A}}^{(2)}$. For a large $\kappa_{\mathrm{A}}^{(2)}$, the feedback is effectively less efficient, since information leaks from the auxiliary cavity. It, however, increases the detected information and raises the effective overall detection efficiency. The feedback cooling scheme does not have this concern. Both the optimal $\kappa_{\mathrm{A}}^{(1)}/2\pi$ and $\kappa_{\mathrm{A}}^{(2)}/2\pi$ are around 500 kHz,

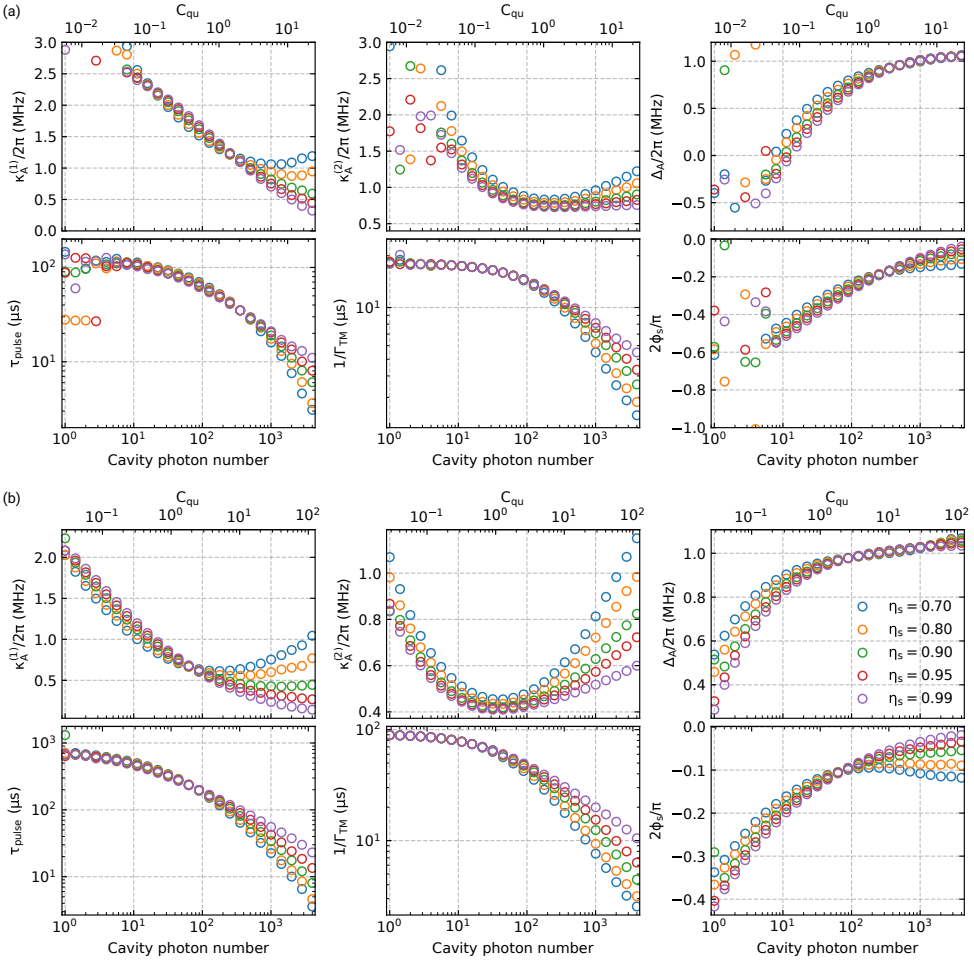

Figure 5.8: Optimized parameters for optomechanical entanglement, with (a) $Q_M = 2 \times 10^7$ and (b) $Q_M = 10^8$.

which is experimentally feasible with a simple Fabry-Pérot cavity. Furthermore, on-chip optical cavities have achieved an intrinsic linewidth that is similar or even smaller[114, 115]. Potentially, a fully integrated coherent feedback with 1 MHz mechanical resonator is feasible.

5.7.4. Unintentional coherent feedback in experiments

In experiments, I have observed that the mechanical resonator occasionally gets heated up even when the laser is red-detuned. An example trace is shown in figure 5.9(a). On the left panel it shows the recorded trace (blue) of the detected signal from a phase quadrature measurement, where the laser is red-detuned. Since the detection is from the signal of a mixture of multiple modes, a filtered signal around

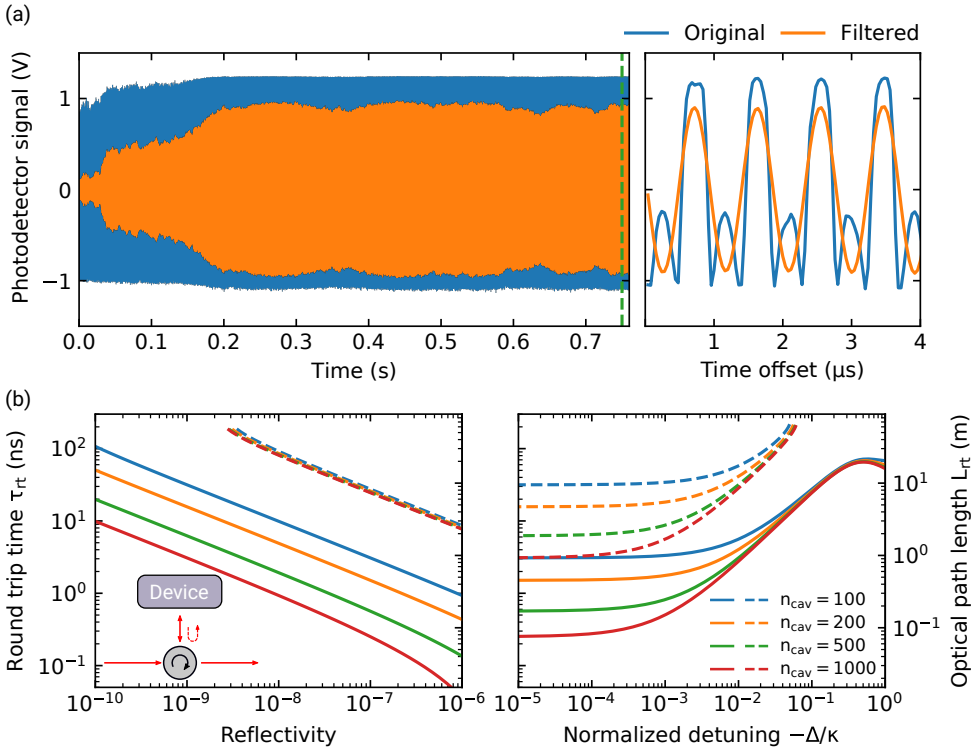

Figure 5.9: (a) A trace showing the increase of the measured signal, with homodyne measurement measuring the phase quadrature and with the laser being red-detuned. It corresponds to a heating process of the mechanical resonator. The blue curve is the measured signal, while the orange shows the filtered signal around the resonance frequency of the fundamental mechanical mode. A zoom in of the trace around the green dashed line is shown in the right plot. Due to the large mechanical resonance amplitude of the fundamental mode which exceed the linear detection regime of the phase measurement, the measured signal is wrapped. The asymmetry is due to the fact that the laser is red detuned. (b) The maximum round trip time and the equivalent free space round trip path length of the back reflection signal, above which instability may occurs for different reflectivity (left) and detuning (right). The solid line on the left figure shows the results for $\Delta = 0$, and the dashed line shows $\delta = -0.1\kappa$. The solid line on the right plot right shows the results for $R = 10^{-7}$, while the dashed line shows $R = 10^{-9}$. The insert on the left plots shows a simplified picture for the back reflection.

the resonance frequency of the fundamental mechanical mode is plotted in orange. The signal increases from small amplitude to large, with a time scale of 0.1 second. On the right I plot a zoom-in of the measured signal around 0.75 second, indicated by the green dashed line. At this point, the measured signal is wrapped at negative voltage, indicating that it is highly excited into a non-linear detection regime. The amplitude of the mechanical oscillation causes a cavity resonance frequency modulation that is comparable or larger than the linewidth κ. The wrapping only happens at negative frequency because the laser is red-detuned. On the positive frequency side, a flat top is also seen. At this point, the filtered signal is no-longer a good indication of the magnitude of the fundamental mode, since it neglects the

higher order terms from the non-linearity. Instability has been reported elsewhere, which was suspected to be the nonlinear dynamics in a system with a large thermal fluctuation.[127] It is, however, not the case here as the cavity frequency shift caused by the thermal fluctuation is still smaller than the optical cavity linewidth.

In my experiment, I attribute it to the back-reflections of the optical components. By manually stretching the fiber between the circulator and the device, the random heating disappears. Also, either by introducing a frequency modulation or turning on coherent control[2] on the laser, the heating issue disappears. In this section, I will show that the back reflection, albeit extremely small, can drive the mechanical resonator into a state with a large oscillation amplitude in my experimental condition. This corresponds to an unstable system in the linearized regime.

The critical part of a typical experimental setup is shown in the insert of figure 5.9(b). The light is sent to an optical circulator, and then it goes into the device. The reflected light from the device is measured. Ideally, all light should travel to another port. It is, however, not the case for a practical device. There are always back reflection from the circulator.[3] In our lab, we have optical circulators with a return loss about or less than 60 db, as shown in the data sheets for individual devices. This corresponds to a back reflection of about $R_{\mathrm{br}} = 10^{-6}$. This forms a coherent feedback scheme, with an effective reflection $R_{\mathrm{A}} = R_{\mathrm{br}}\eta_{\mathrm{rt}}$. The "efficiency" of the feedback, η_{rt}, takes all the additional losses in the round trip and the mismatch in the polarization into account. In an experiment, the loss in optical path is usually minimized in order to increase the detection efficiency. The main source would be from the polarization mismatch, where the polarization of the light changes in the fiber. Then the reflected light in general would not have the exact polarization that can couples back into the cavity efficiently. In principle, a fiber polarization controller can be added to enhance this polarization mismatch in order to minimize the effective reflection R_{A}. However, tuning the polarization is challenging because of the extremely small magnitude of the back reflection. Thus it is not performed in experiments. An optimistic guess of η_{rt} would be of the order of 0.1, leading to an effective R_{A} to be of the order of 10^{-7}. Further, the device is in a vacuum chamber, while the circulator is in air. A long fiber is required to connect them.[4] In the experimental setup, the exact length is not measured, but it is estimated to be around 5 meters. The fiber introduces a delay for the back-reflected signal.

With the coherent feedback scheme with an auxiliary mirror, it is possible to calculate the maximum allowed delay for avoiding having instability of the system. Also, the phase of the reflected light is not a controllable parameter in the experiment. It drifts over time, with a time scale of second. Thus, it is illustrative to look at the shortest maximum allowed delay for all the phases. In the calculation I minimize the maximum allowed delay with respect to the phase. In figure 5.9(b) I show the calculated results, with $\Omega_{\mathrm{M}}/2\pi = 1$ MHz, $Q_{\mathrm{M}} = 2 \times 10^7$. On the left panel

[2] It makes the laser output less coherent. The linewidth of the laser gets broadened.

[3] There are more sources for the back reflection, such as the fiber connectors and the fusion point for splicing the fibers. For simplicity, I only focus on the circulator in this text.

[4] In practice, the length of the fiber cannot be too short in the consideration of the ease of replacing fiber when needed.

I show the effect of R_{A}. Clearly, an extremely small R_{A} would have a significant effect, especially for zero detuning (solid lines), and it is sensitive to the cavity photon number. For red detuning $\Delta = -0.1\kappa$ (dashed lines), a larger round-trip time is allowed. The requirement is still stringent. An effective reflection of 10^{-7} requires a round-trip delay of smaller than 2.6 ns. It corresponds to a free-space optical path of 8 m, which means that it requires a fiber connection between the device and the optical circulator to be shorter than 2.7 m. It is shorter than the length I have in the experiment. A smaller $R_{\mathrm{A}} \lesssim 3 \times 10^{-9}$ does not introduce instability. For $\Delta = 0.1\kappa$, the damping from the optical spring is larger than the intrinsic damping of the mechanical resonator and thus the heating is not very sensitive to the cavity photon number. Note that a large detuning is not very favorable in some potential experiments, such as entanglement generation[79]. For various detunings, I plot the results on the right panel, with the solid line for $R_{\mathrm{A}} = 10^{-7}$ and the dashed line for $R_{\mathrm{A}} = 10^{-9}$.

To conclude this section, due to the unintended coherent feedback from the back-reflection of the optical components, instability is very likely to occur in an experiment. Note that the above analysis only studies the instability within a linearized model. It does not include nonlinearity when the mechanical resonator is driven hard. More importantly, the instability is only an extreme case of heating. Even in the stable regime predicted by the stability analysis, heating can still occur. When the heating power is sufficiently strong but still not strong enough to lead to instability, it can still lead to the regime where the detuning modulation caused by the mechanical resonator is larger then the optical linewidth. Thus, the above analysis may yield more optimistic results comparing to the practical situation.

6

Conclusion and outlook

The work in this thesis is aiming at bringing a macroscopic mechanical resonator in a classical environment towards the quantum regime, based on integrated cavity optomechanical structures. The central tasks are to reduce the coupling of the mechanical resonator to the environment, and to have efficient measurement and control over the mechanical resonator. It means that we want a mechanical resonator with a high $Q_{\mathrm{M}} \times f_{\mathrm{M}}$, and an optomechanical device allows large g^2/κ. In the following, I will conclude the way I took to approach the goal. I will also discuss challenges and potential further improvements.

Optomechanical device with long mechanical string

In chapter 3, this type of devices has been designed and fabricated on high-stress silicon nitride. It involves a mechanical resonator with adiabatically chirped phononic crystals. By designing the geometry of the phononic structure, it would then localize a mechanical mode with high mechanical quality factor. The optical cavity is derived from the zipper cavity[86], with one part connecting to the phononic structure, and the other part attaching to the substrate directly. A substantial improvement is achieved by introducing a fishbone structure to both the photonic and phononic structures. I then perform feedback cooling at room temperature, achieving an average phonon number of 27 from 6×10^6. The limitation was from classical noise outside the structure, which was removed afterward.

This type of devices, however, has its issues.

- The mode-of-interest is not the fundamental mode of the system. There are many modes closed by. Furthermore, they have a similar optomechanical coupling strength G_{OM} to what the mode-of-interest has. The motion of these modes can easily become classical noise. It is especially important if resolving the motion at a very small time scale is needed.
- Many mechanical modes have low frequencies and thus larger thermal fluctuations. They also have a similar G_{OM} to what the mode-of-interest has. They

impose a limit of the optical linewidth κ that it cannot be too small. Otherwise the non-linearity from the optical cavity would be significant.

- A long string leads to a bad thermalization. For practical devices they absorb photons and convert them to heat. The raise of the temperature shifts the optical resonance frequency. At large cavity photon number it would enter the thermal bistability regime. For this type of structure, the "large" cavity photon number is too small to achieve the rate where the photon-phonon interaction is comparable to the thermal decoherence.

- It is hard to achieve a higher $Q_{\mathrm{M}} \times f_{\mathrm{M}}$. It is mostly limited by the width of the structure, which can not be too narrow. It might also suffer from fabrication imperfections, which introduces lots of surface loss, and suffer from all the phononic geometries that introduce large bending at specific locations. Making the structure longer can potentially reduce the overall bending strength and increase the stress at the center, potentially leads to a higher $Q_{\mathrm{M}} \times f_{\mathrm{M}}$. However, apart from the difficulties in fabrication, a longer string is unfavorable considering the aforementioned issues.

To tackle these problems, I have developed a new type of devices.

6

Integrated optomechanical device coupling to out-of-plane mode

The new type of devices is based on the development of a novel and versatile fabrication technique, described in chapter 4. By using a fiber tip transferring microfabricated components, it is possible to place a photonic crystal above a mechanical structure, separated by a small gap. It allows a large optomechanical coupling to the out-of-plane motions of mechanical resonators. Especially, I adapt a mechanical structure possessing high-Q fundamental out-of-plane mode. The mode-of-interest is then the fundamental mode, with all the other modes far away and without modes with larger thermal fluctuations. By implementing clamps to each of the unit cells of the photonic crystal cavity, the thermal conductivity is greatly enhanced. It allows a large intracavity photon number. We performed measurement based feedback cooling at room temperature, achieving a phonon number of 22.

However, fabricating device in this way also comes with costs. Two issues are listed below

- Coupling between the mechanical motion of the photonic crystal and the mechanical resonator. This leads to some reduction of the mechanical quality factor on the mechanical resonator.

- Classical noise introduced by the thermal motion of the photonic crystal.

The first issue can be solved by increasing the distance between the photonic crystal and the mechanical structures, at the cost of a great reduction in the optomechanical coupling. Investigating the source of the coupling is also important, and potentially it leads to ways reducing the coupling. The second can potentially be addressed by cooling down the device into a cryogenic temperature. However,

it counteracts a long-standing goal to bring quantum-limited or quantum-enhanced applications to high temperature, or even to room temperature. For both issues, improvements can also be done on the photonic crystal structure, namely by making it more "rigid" in the frequency range we are interested in. We need a photonic crystal with a much lower mechanical dissipation, higher mechanical frequencies, and higher effective mass. It is nevertheless still challenging. For the photonic structure, it is fully released and it does not have any stress. The quality factor and the frequency is largely limited by the material properties, i.e., the internal damping rate and the Young's modulus. Investigating different materials, potentially with a lower loss, for the photonic crystal might thus be an option. Alternatively, putting a bulk material with low refractive index, such as silicon dioxide, directly on top of the photonic crystal might address this issue. The bulk material typically does not have a high response on the frequency range considered here. Also, the mass is large. By sticking the photonic crystal onto the bulk material, the motion of the photonic crystal would be small and the coupling might be weak. A bulk material, however, might not be compatible to the technique introduced here due to the large thickness and mass. Methods similar to wafer bounding techniques, such as flip-chip,[128] with precision alignments might potentially be employed. It is still technically challenging considering the coupling interface between the photonic crystal and the fiber. It also needs the surface to be flat. Further developments are needed.

Coherent feedback in the sideband-unresolved regime

Now, imagine that a good device already exists. It has a weak coupling to the environment, and it is possible to have an efficient and fast interaction to the mechanical resonator. Such a device is still extremely challenging at room temperature, but it might already be feasible at 4.2 K by marginally improving the device in chapter 4. For such a situation, is there anything still missing? I consider such a question in chapter 5.

In cavity optomechanics, people usually consider an optomechanical system in the sideband-resolved regime. However, for many integrated optomechanical system with really macroscopic mechanical resonator, including everything in this thesis, they are in the sideband-unresolved regime. A fundamental difference between these two regimes is the effect of the cavity response. When light comes, if it interacts with the mechanical resonator weakly which is the typical situation here, it generates two sidebands. In the sideband-resolved regime, one of the sideband generation can be suppressed by the cavity response for a proper detuning. The suppression, however, is negligible in the sideband-unresolved regime. The difference can also be viewed in a feedback picture, where the optical cavity of the optomechancial system is a feedback component[101]. The feedback response is different for difference frequency range of interest. The positive part of a sideband-unresolved system is that the information of the mechanical resonator couples to the outside unfiltered, allowing building an extra feedback. This builds the basic idea of a measurement-based feedback, which is effective in cooling the mechanical resonator. It is also largely limited to cooling due to the destroy of optical coherence through the measurement. In this chapter, I consider feedback

by linear, passive optical components without measurement. I show that it is possible to go beyond the cooling. Indeed, the linearized dynamics can be made to be similar to a sideband-resolved system. Further improvements can be achieved by optimizing all the parameters involved in such a system. With this, it is possible to achieve cooling, which outperforms a simple measurement-based feedback cooling, and phonon-photon entanglement generation and verification.

This work aims at potential experiments. The parameters considering in this work is feasible, and it might even be possible to integrate the full coherent system onto a chip. However, in a real experiments, it is much more than a simplified model plus a few parameters. Here, I list some challenges, and some with potential solutions.

- In a practical system, delay exists and a feedback might heat up some of the modes. On the other hands, the delay can be minimized if it is possible to integrate the whole feedback system on-chip, with the exception of the coherent feedback with mirror and intentional delay line. Also, in coherent feedback cooling, since it is continuous measurement, other modes can still be stabilized by measurement-based feedback cooling. The measurement-based feedback cooling does not have to achieve a very large cooling power, thus most of the light can still be used for the coherent feedback of the main mode. For entanglement generation and verification, it might not be an issue since the interaction time is limited. Additional stabilization is also possible.
- Efficiency. In the calculation, I show that the scheme is reasonably robust against photon loss on the feedback path. An highly efficient feedback is still desirable. This might be achieved by integrating the whole system onto a chip. Otherwise, a free-space setup might also provide improvements to a fiber-based setup.
- Complexity and integration. An optomechanical system with optical feedback would result in a complex setup. An integrated system is thus favorable. It is, however, technical challenging for the devices considered in this work, which have a mechanical resonance frequency of 1 MHz. Although on-chip optical resonator with sub-MHz linewidth have been demonstrated recently[114, 115], their fabrication is still challenging. Furthermore, how to integrate them with an optomechanical structure is still an open question.
- Device quality. A better optomechanical device is always beneficial. This, however, is beyond the scope of this specific work. I would refer readers to the previous chapters.

Summary

In general, to push the field forward, having a good integrated optomechanical device is still the key. In the recent years, such as the works in chapter 3, 4 and references [60, 64, 77, 80, 129], we have seen many promising designs of the mechanical resonators. In this work, I have also made progresses in the integration with an optical cavity, allowing large optomechanical interaction. With

further developments in the integrated optomechanical system, and a more advanced integration technique which potentially allows complex functions on a chip, it is promising to achieve quantum-limited or quantum-enhanced applications with mechanical resonator. This is a long and outstanding goal, and by no mean it can be answered by this single thesis. Still, it makes small improvements, bringing classical mechanical resonators towards the quantum regime in its own way.

A

Devices fabrication

The fabrication of devices process is shown in figure A.1.

(a) High stress thin silicon nitride film is first deposited on Silicon wafer using low pressure chemical vapor deposition (LPCVD) process. By controlling the deposition temperature to be 800 °C, it would result in a internal stress of > 1 GPa in the silicon nitride thin film. The wafer is then diced into chips of $1\text{ cm} \times 1\text{ cm}$.

(b) A thin layer of e-beam resists (AR 6200-13) is spin coated onto the chip. The spinning speed depends on the thickness of the silicon nitride film. For 350 nm film, a spinning speed of 900 rpm is used. A thicker layer of resists guarantees that the resit would not be etched away in the following steps. However, a thicker resists reduces the usable area of a chip. On a larger area of the chip, extended from the boundary of the chip to the inside, the resists is non-uniform. Immediately, the chip is baked on a hot plate at 150 °C for 3 minutes.

(c) The resists are patterned using electron beam (e-beam) lithography. the resists exposed to the electron changes its chemical properties.

(d) The chip is developed in pentyl acetate, xylene, and then IPA for 1 minute, 5 seconds and 1 minute, respectively. The resists used in this work are positive resists. The areas exposed to electron are washed away.

(e) The pattern on the resists is transferred onto the SiN film. This is done by exposing the chip to CHF_3 in a reacting ion etcher. The SiN which is not covered by the resists would be etched away. Note that CHF_3 also etches resists. This determines the minimum resists thickness, and the maximum spinning speeds in step (b).

A

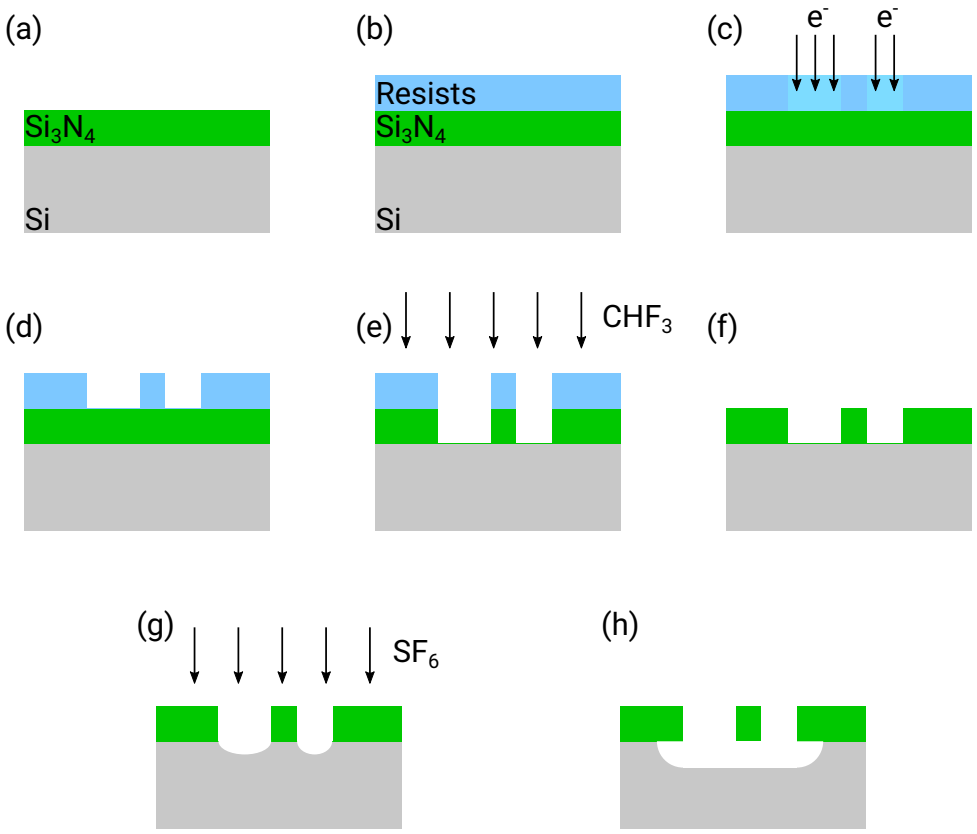

Figure A.1: Fabrication of Silicon Nitride devices.

(f) The resists is then removed by dimethylformamide (DMF). The chip is immersed in the solution, and then it is sonicated with a low power. This removes most of the resists on the chip. Then, piranha solution, a mixture of H_2SO_4 and H_2O_2, is used to clean the chip. H_2SO_4 is pre-heated to above 70 °C. After the mixture, the temperature can go up to ~ 120 °C and it forms lots of bubbles. The chip is put into the solution immediately, and it stays inside for 8 minutes. Piranha solution is a strong oxidizing agent and it removes the residue organics on the chip. However, it also could oxidize silicon, and more importantly, probably silicon nitride. It has been shown that the oxidation of silicon nitride reduce its mechanical quality factor. The oxidation layer is removed by immersing the chip into 1% HF solutions for 1 minute. Since HF also etches siilcon nitride, for the chip where mechanical quality factor is not of concern and with very fine structures, the process time is reduced.

(g) The last step is to etch the silicon underneath the silicon nitride. This is done by a dry etching process, exposing the chip with SF_6 at -120 °C. The etching is isotropic and fast. The etching distance is typically 6 μm with an etching

time of 20 seconds in this work. For the mechanical chip in chapter 5, in order to have a lower overhanging part, the etching time is reduced to 11 seconds.

(h) A chip is finished.

References

[1] D. J. Griffiths and D. F. Schroeter, *Introduction to Quantum Mechanics*, 3rd ed. (Cambridge University Press, Cambridge, 2018).

[2] J. J. Sakurai and J. Napolitano, *Modern Quantum Mechanics*, 2nd ed. (Cambridge University Press, Cambridge, 2017).

[3] E. Rosencher and B. Vinter, *Optoelectronics* (Cambridge University Press, Cambridge, UK, 2002).

[4] S. M. Sze and M. K. Lee, *Semiconductor devices: physics and technology*, 3rd ed. (Wiley, New York, NY, 2012).

[5] B. L. Schmittberger and D. R. Scherer, *A Review of Contemporary Atomic Frequency Standards,* arXiv:2004.09987 [physics] (2020), arXiv: 2004.09987.

[6] A. Mari, G. De Palma, and V. Giovannetti, *Experiments testing macroscopic quantum superpositions must be slow,* Scientific Reports **6**, 22777 (2016).

[7] J. W. Judy, *Microelectromechanical systems (MEMS): fabrication, design and applications,* Smart Materials and Structures **10**, 1115 (2001).

[8] A. G. Krause, M. Winger, T. D. Blasius, Q. Lin, and O. Painter, *A high-resolution microchip optomechanical accelerometer,* Nature Photonics **6**, 768 (2012).

[9] N. Yazdi, F. Ayazi, and K. Najafi, *Micromachined inertial sensors,* Proceedings of the IEEE **86**, 1640 (1998).

[10] S. Tadigadapa and K. Mateti, *Piezoelectric MEMS sensors: state-of-the-art and perspectives,* Measurement Science and Technology **20**, 092001 (2009).

[11] Y. Chen, *Macroscopic quantum mechanics: theory and experimental concepts of optomechanics,* Journal of Physics B: Atomic, Molecular and Optical Physics **46**, 104001 (2013).

[12] A. Bassi, K. Lochan, S. Satin, T. P. Singh, and H. Ulbricht, *Models of wave-function collapse, underlying theories, and experimental tests,* Reviews of Modern Physics **85**, 471 (2013).

[13] M. Forsch, R. Stockill, A. Wallucks, I. Marinkovic, C. Gärtner, R. A. Norte, F. van Otten, A. Fiore, K. Srinivasan, and S. Gröblacher, *Microwave-to-optics conversion using a mechanical oscillator in its quantum ground state,* Nature Physics **16**, 69 (2020).

[14] J. Bochmann, A. Vainsencher, D. D. Awschalom, and A. N. Cleland, *Nanomechanical coupling between microwave and optical photons,* Nature Physics **9**, 712 (2013).

[15] R. W. Andrews, R. W. Peterson, T. P. Purdy, K. Cicak, R. W. Simmonds, C. A. Regal, and K. W. Lehnert, *Bidirectional and efficient conversion between microwave and optical light,* Nature Physics **10**, 321 (2014).

[16] A. A. Clerk, M. H. Devoret, S. M. Girvin, F. Marquardt, and R. J. Schoelkopf, *Introduction to quantum noise, measurement, and amplification,* Reviews of Modern Physics **82**, 1155 (2010).

[17] T. Ono, R. Okamoto, and S. Takeuchi, *An entanglement-enhanced microscope,* Nature Communications **4**, 2426 (2013).

[18] C. Degen, F. Reinhard, and P. Cappellaro, *Quantum sensing,* Reviews of Modern Physics **89**, 035002 (2017).

[19] D. Braun, G. Adesso, F. Benatti, R. Floreanini, U. Marzolino, M. W. Mitchell, and S. Pirandola, *Quantum-enhanced measurements without entanglement,* Reviews of Modern Physics **90**, 035006 (2018).

[20] J. P. Dowling, *Quantum optical metrology – the lowdown on high-N00N states,* Contemporary Physics **49**, 125 (2008).

[21] A. Wallucks, I. Marinkovic, B. Hensen, R. Stockill, and S. Gröblacher, *A quantum memory at telecom wavelengths,* Nature Physics **16**, 772 (2020).

[22] M. Aspelmeyer, T. J. Kippenberg, and F. Marquardt, *Cavity optomechanics,* Reviews of Modern Physics **86**, 1391 (2014).

[23] W. P. Bowen and G. J. Milburn, *Quantum optomechanics* (CRC press, 2015).

[24] B. P. Abbott *et al.* (LIGO Scientific Collaboration and Virgo Collaboration), *Observation of gravitational waves from a binary black hole merger,* Phys. Rev. Lett. **116**, 061102 (2016).

[25] M. Schlosshauer, *Quantum decoherence,* Physics Reports Quantum decoherence, **831**, 1 (2019).

[26] D. F. Walls and G. J. Milburn, *Quantum Optics* (Springer-Verlag Berlin Heidelberg, 2008).

[27] V. Giovannetti and D. Vitali, *Phase-noise measurement in a cavity with a movable mirror undergoing quantum Brownian motion,* Physical Review A **63**, 023812 (2001).

[28] M. R. Vanner, I. Pikovski, G. D. Cole, M. S. Kim, C. Brukner, K. Hammerer, G. J. Milburn, and M. Aspelmeyer, *Pulsed quantum optomechanics,* Proceedings of the National Academy of Sciences **108**, 16182 (2011).

[29] J. S. Bennett, K. Khosla, L. S. Madsen, M. R. Vanner, H. Rubinsztein-Dunlop, and W. P. Bowen, *A quantum optomechanical interface beyond the resolved sideband limit,* New Journal of Physics **18**, 053030 (2016).

[30] K. E. Khosla, G. A. Brawley, M. R. Vanner, and W. P. Bowen, *Quantum optomechanics beyond the quantum coherent oscillation regime,* Optica **4**, 1382 (2017).

[31] J. Clarke, P. Sahium, K. E. Khosla, I. Pikovski, M. S. Kim, and M. R. Vanner, *Generating mechanical and optomechanical entanglement via pulsed interaction and measurement,* New Journal of Physics **22**, 063001 (2020).

[32] D. J. Wilson, V. Sudhir, N. Piro, R. Schilling, A. Ghadimi, and T. J. Kippenberg, *Measurement-based control of a mechanical oscillator at its thermal decoherence rate,* Nature **524**, 325 (2015).

[33] S. G. Hofer, W. Wieczorek, M. Aspelmeyer, and K. Hammerer, *Quantum entanglement and teleportation in pulsed cavity optomechanics,* Physical Review A **84**, 052327 (2011).

[34] B. L. Schumaker, *Noise in homodyne detection,* Optics Letters **9**, 189 (1984).

[35] S. A. Fedorov, N. J. Engelsen, A. H. Ghadimi, M. J. Bereyhi, R. Schilling, D. J. Wilson, and T. J. Kippenberg, *Generalized dissipation dilution in strained mechanical resonators,* Physical Review B **99**, 054107 (2019).

[36] D. R. Southworth, R. A. Barton, S. S. Verbridge, B. Ilic, A. D. Fefferman, H. G. Craighead, and J. M. Parpia, *Stress and Silicon Nitride: A Crack in the Universal Dissipation of Glasses,* Physical Review Letters **102**, 225503 (2019).

[37] Q. P. Unterreithmeier, T. Faust, and J. P. Kotthaus, *Damping of Nanomechanical Resonators,* Physical Review Letters **105**, 027205 (2010).

[38] M. Imboden and P. Mohanty, *Dissipation in nanoelectromechanical systems,* Physics Reports Dissipation in nano-electromechanical systems, **534**, 89 (2014).

[39] L. Villanueva and S. Schmid, *Evidence of Surface Loss as Ubiquitous Limiting Damping Mechanism in SiN Micro- and Nanomechanical Resonators,* Physical Review Letters **113**, 227201 (2014).

[40] J. Guo, R. Norte, and S. Gröblacher, *Feedback Cooling of a Room Temperature Mechanical Oscillator close to its Motional Ground State,* Physical Review Letters **123**, 223602 (2019).

[41] A. D. O'Connell, M. Hofheinz, M. Ansmann, R. C. Bialczak, M. Lenander, E. Lucero, M. Neeley, D. Sank, H. Wang, M. Weides, J. Wenner, J. M. Martinis, and A. N. Cleland, *Quantum ground state and single-phonon control of a mechanical resonator,* Nature **464**, 697 (2010).

[42] T. A. Palomaki, J. D. Teufel, R. W. Simmonds, and K. W. Lehnert, *Entangling Mechanical Motion with Microwave Fields,* Science **342**, 710 (2013).

[43] S. Hong, R. Riedinger, I. Marinkovic, A. Wallucks, S. G. Hofer, R. A. Norte, M. Aspelmeyer, and S. Gröblacher, *Hanbury Brown and Twiss interferometry of single phonons from an optomechanical resonator,* Science **358**, 203 (2017).

[44] R. Riedinger, A. Wallucks, I. Marinkovic, C. Löschnauer, M. Aspelmeyer, S. Hong, and S. Gröblacher, *Remote quantum entanglement between two micromechanical oscillators,* Nature **556**, 473 (2018).

[45] C. F. Ockeloen-Korppi, E. Damskägg, J.-M. Pirkkalainen, M. Asjad, A. A. Clerk, F. Massel, M. J. Woolley, and M. A. Sillanpää, *Stabilized entanglement of massive mechanical oscillators,* Nature **556**, 478 (2018).

[46] I. Marinkovic, A. Wallucks, R. Riedinger, S. Hong, M. Aspelmeyer, and S. Gröblacher, *Optomechanical Bell Test,* Physical Review Letters **121**, 220404 (2018).

[47] R. A. Norte, M. Forsch, A. Wallucks, I. Marinkovic, and S. Gröblacher, *Platform for Measurements of the Casimir Force between Two Superconductors,* Physical Review Letters **121**, 030405 (2018).

[48] J. Chan, T. P. M. Alegre, A. H. Safavi-Naeini, J. T. Hill, A. Krause, S. Gröblacher, M. Aspelmeyer, and O. Painter, *Laser cooling of a nanomechanical oscillator into its quantum ground state,* Nature **478**, 89 (2011).

[49] J. D. Teufel, T. Donner, D. Li, J. W. Harlow, M. S. Allman, K. Cicak, A. J. Sirois, J. D. Whittaker, K. W. Lehnert, and R. W. Simmonds, *Sideband cooling of micromechanical motion to the quantum ground state,* Nature **475**, 359 (2011).

[50] M. Underwood, D. Mason, D. Lee, H. Xu, L. Jiang, A. B. Shkarin, K. Børkje, S. M. Girvin, and J. G. E. Harris, *Measurement of the motional sidebands of a nanogram-scale oscillator in the quantum regime,* Physical Review A **92**, 061801 (2015).

[51] R. W. Peterson, T. P. Purdy, N. S. Kampel, R. W. Andrews, P.-L. Yu, K. W. Lehnert, and C. A. Regal, *Laser Cooling of a Micromechanical Membrane to the Quantum Backaction Limit,* Physical Review Letters **116**, 063601 (2016).

[52] M. Rossi, D. Mason, J. Chen, Y. Tsaturyan, and A. Schliesser, *Measurement-based quantum control of mechanical motion,* Nature **563**, 53 (2018).

[53] F. Marquardt, J. P. Chen, A. A. Clerk, and S. M. Girvin, *Quantum Theory of Cavity-Assisted Sideband Cooling of Mechanical Motion,* Physical Review Letters **99**, 093902 (2007).

[54] U. Delic, M. Reisenbauer, D. Grass, N. Kiesel, V. Vuletic, and M. Aspelmeyer, *Cavity Cooling of a Levitated Nanosphere by Coherent Scattering,* Physical Review Letters **122**, 123602 (2019).

[55] F. Tebbenjohanns, M. Frimmer, A. Militaru, V. Jain, and L. Novotny, *Cold Damping of an Optically Levitated Nanoparticle to Microkelvin Temperatures,* Physical Review Letters **122**, 223601 (2019).

[56] G. P. Conangla, F. Ricci, M. T. Cuairan, A. W. Schell, N. Meyer, and R. Quidant, *Optimal Feedback Cooling of a Charged Levitated Nanoparticle with Adaptive Control,* Physical Review Letters **122**, 223602 (2019).

[57] F. Tebbenjohanns, M. Frimmer, V. Jain, D. Windey, and L. Novotny, *Motional Sideband Asymmetry of a Nanoparticle Optically Levitated in Free Space,* Physical Review Letters **124**, 013603 (2020).

[58] R. Norte, J. Moura, and S. Gröblacher, *Mechanical Resonators for Quantum Optomechanics Experiments at Room Temperature,* Physical Review Letters **116**, 147202 (2016).

[59] C. Reinhardt, T. Müller, A. Bourassa, and J. C. Sankey, *Ultralow-Noise SiN Trampoline Resonators for Sensing and Optomechanics,* Physical Review X **6**, 021001 (2016).

[60] Y. Tsaturyan, A. Barg, E. S. Polzik, and A. Schliesser, *Ultracoherent nanomechanical resonators via soft clamping and dissipation dilution,* Nature Nanotechnology **12**, 776 (2017).

[61] Y. T. Liu and K. S. Thorne, *Thermoelastic noise and homogeneous thermal noise in finite sized gravitational-wave test masses,* Physical Review D **62**, 122002 (2000).

[62] G. M. Harry, H. Armandula, E. Black, D. R. M. Crooks, G. Cagnoli, J. Hough, P. Murray, S. Reid, S. Rowan, P. Sneddon, M. M. Fejer, R. Route, and S. D. Penn, *Thermal noise from optical coatings in gravitational wave detectors,* Applied Optics **45**, 1569 (2006).

[63] A. G. Krause, T. D. Blasius, and O. Painter, *Optical read out and feedback cooling of a nanostring optomechanical cavity,* arXiv preprint arXiv:1506.01249 (2015).

[64] A. H. Ghadimi, S. A. Fedorov, N. J. Engelsen, M. J. Bereyhi, R. Schilling, D. J. Wilson, and T. J. Kippenberg, *Elastic strain engineering for ultralow mechanical dissipation,* Science **360**, 764 (2018).

[65] A. H. Ghadimi, *Ultra-coherent nano-mechanical resonators for quantum optomechanics at room temperature*, Ph.D. thesis, École polytechnique fédérale de Lausanne (2018).

[66] D. Kleckner and D. Bouwmeester, *Sub-kelvin optical cooling of a micromechanical resonator,* Nature **444**, 75 (2006).

[67] S. Gröblacher, J. T. Hill, A. H. Safavi-Naeini, J. Chan, and O. Painter, *Highly efficient coupling from an optical fiber to a nanoscale silicon optomechanical cavity,* Applied Physics Letters **103**, 181104 (2013).

[68] J. Chan, *Laser cooling of an optomechanical crystal resonator to its quantum ground state of motion*, Ph.D. thesis, California Institute of Technology (2012).

[69] S. G. Johnson, M. Ibanescu, M. A. Skorobogatiy, O. Weisberg, J. D. Joannopoulos, and Y. Fink, *Perturbation theory for Maxwell's equations with shifting material boundaries,* Physical Review E **65**, 066611 (2002).

[70] C. Genes, D. Vitali, P. Tombesi, S. Gigan, and M. Aspelmeyer, *Ground-state cooling of a micromechanical oscillator: Comparing cold damping and cavity-assisted cooling schemes,* Physical Review A **77**, 033804 (2008).

[71] P. E. Allain, L. Schwab, C. Mismer, M. Gely, E. Mairiaux, M. Hermouet, B. Walter, G. Leo, S. Hentz, M. Faucher, G. Jourdan, B. Legrand, and I. Favero, *Optomechanical resonating probe for very high frequency sensing of atomic forces,* Nanoscale **12**, 2939 (2020).

[72] W. J. Westerveld, M. Mahmud-Ul-Hasan, R. Shnaiderman, V. Ntziachristos, X. Rottenberg, S. Severi, and V. Rochus, *Sensitive, small, broadband and scalable optomechanical ultrasound sensor in silicon photonics,* Nature Photonics **15**, 341 (2021).

[73] K. Stannigel, P. Rabl, A. S. Sørensen, P. Zoller, and M. D. Lukin, *Optomechanical Transducers for Long-Distance Quantum Communication,* Physical Review Letters **105**, 220501 (2010).

[74] N. Fiaschi, B. Hensen, A. Wallucks, R. Benevides, J. Li, T. P. M. Alegre, and S. Gröblacher, *Optomechanical quantum teleportation,* arXiv:2104.02080 [cond-mat, physics:physics, physics:quant-ph] (2021), arXiv: 2104.02080.

[75] M. Bahrami, M. Paternostro, A. Bassi, and H. Ulbricht, *Proposal for a Noninterferometric Test of Collapse Models in Optomechanical Systems,* Physical Review Letters **112**, 210404 (2014).

[76] M. Carlesso and S. Donadi, *Collapse Models: Main Properties and the State of Art of the Experimental Tests,* in *Advances in Open Systems and Fundamental Tests of Quantum Mechanics*, Springer Proceedings in Physics, edited by B. Vacchini, H.-P. Breuer, and A. Bassi (Springer International Publishing, 2019) pp. 1–13.

[77] S. Fedorov, A. Beccari, N. Engelsen, and T. Kippenberg, *Fractal-like mechanical resonators with a soft-clamped fundamental mode,* Physical Review Letters **124**, 025502 (2020).

[78] C. Whittle, E. D. Hall, S. Dwyer, N. Mavalvala, V. Sudhir, R. Abbott, A. Ananyeva, C. Austin, L. Barsotti, J. Betzwieser, C. D. Blair, A. F. Brooks, D. D. Brown, A. Buikema, C. Cahillane, J. C. Driggers, A. Effler, A. Fernandez-Galiana, P. Fritschel, V. V. Frolov, T. Hardwick, M. Kasprzack, K. Kawabe, N. Kijbunchoo, J. S. Kissel, G. L. Mansell, F. Matichard, L. McCuller, T. McRae, A. Mullavey, A. Pele, R. M. S. Schofield, D. Sigg, M. Tse, G. Vajente, D. C. Vander-Hyde, H. Yu, H. Yu, C. Adams, R. X. Adhikari, S. Appert, K. Arai, J. S. Areeda, Y. Asali, S. M. Aston, A. M. Baer, M. Ball, S. W. Ballmer, S. Banagiri, D. Barker, J. Bartlett, B. K. Berger, D. Bhattacharjee, G. Billingsley, S. Biscans, R. M. Blair, N. Bode, P. Booker, R. Bork, A. Bramley, K. C. Cannon, X. Chen, A. A. Ciobanu, F. Clara, C. M. Compton, S. J. Cooper, K. R. Corley, S. T. Countryman, P. B. Covas, D. C. Coyne, L. E. H. Datrier, D. Davis, C. Di Fronzo, K. L. Dooley, P. Dupej, T. Etzel, M. Evans, T. M. Evans, J. Feicht, P. Fulda, M. Fyffe, J. A. Giaime, K. D. Giardina, P. Godwin, E. Goetz, S. Gras, C. Gray, R. Gray, A. C. Green, E. K. Gustafson, R. Gustafson, J. Hanks, J. Hanson, R. K. Hasskew, M. C. Heintze, A. F. Helmling-Cornell, N. A. Holland, J. D. Jones, S. Kandhasamy, S. Karki, P. J. King, R. Kumar, M. Landry, B. B. Lane, B. Lantz, M. Laxen, Y. K. Lecoeuche, J. Leviton, J. Liu, M. Lormand, A. P. Lundgren, R. Macas, M. MacInnis, D. M. Macleod, S. Márka, Z. Márka, D. V. Martynov, K. Mason, T. J. Massinger, R. McCarthy, D. E. McClelland, S. McCormick, J. McIver, G. Mendell, K. Merfeld, E. L. Merilh, F. Meylahn, T. Mistry, R. Mittleman, G. Moreno, C. M. Mow-Lowry, S. Mozzon, T. J. N. Nelson, P. Nguyen, L. K. Nuttall, J. Oberling, R. J. Oram, C. Osthelder, D. J. Ottaway, H. Overmier, J. R. Palamos, W. Parker, E. Payne, R. Penhorwood, C. J. Perez, M. Pirello, H. Radkins, K. E. Ramirez, J. W. Richardson, K. Riles, N. A. Robertson, J. G. Rollins, C. L. Romel, J. H. Romie, M. P. Ross, K. Ryan, T. Sadecki, E. J. Sanchez, L. E. Sanchez, T. R. Saravanan, R. L. Savage, D. Schaetz, R. Schnabel, E. Schwartz, D. Sellers, T. Shaffer, B. J. J. Slagmolen, J. R. Smith, S. Soni, B. Sorazu, A. P. Spencer, K. A. Strain, L. Sun, M. J. Szczepańczyk, M. Thomas, P. Thomas, K. A. Thorne, K. Toland, C. I. Torrie, G. Traylor, A. L. Urban, G. Valdes, P. J. Veitch, K. Venkateswara, G. Venugopalan, A. D. Viets, T. Vo, C. Vorvick, M. Wade, R. L. Ward, J. Warner, B. Weaver, R. Weiss, B. Willke, C. C. Wipf, L. Xiao, H. Yamamoto, L. Zhang, M. E. Zucker, and J. Zweizig, *Approaching the motional ground state of a 10-kg object,* Science **372**, 1333 (2021).

[79] C. Gut, K. Winkler, J. Hoelscher-Obermaier, S. G. Hofer, R. M. Nia, N. Walk, A. Steffens, J. Eisert, W. Wieczorek, J. A. Slater, M. Aspelmeyer, and K. Hammerer, *Stationary optomechanical entanglement between a mechanical oscillator and its measurement apparatus,* Physical Review Research **2**, 033244 (2020).

[80] A. Beccari, M. J. Bereyhi, R. Groth, S. A. Fedorov, A. Arabmoheghi, N. J. Engelsen, and T. J. Kippenberg, *Hierarchical tensile structures with ultralow mechanical dissipation,* arXiv:2103.09785 [cond-mat, physics:physics, physics:quant-ph] (2021), arXiv: 2103.09785.

[81] v. Zobenica, R. W. van der Heijden, M. Petruzzella, F. Pagliano, R. Leijssen, T. Xia, L. Midolo, M. Cotrufo, Y. Cho, F. W. M. van Otten, E. Verhagen, and A. Fiore, *Integrated nano-opto-electro-mechanical sensor for spectrometry and nanometrology,* Nature Communications **8**, 2216 (2017).

[82] T. Liu, F. Pagliano, R. van Veldhoven, V. Pogoretskiy, Y. Jiao, and A. Fiore, *Integrated nano-optomechanical displacement sensor with ultrawide optical bandwidth,* Nature Communications **11**, 2407 (2020).

[83] A. W. Elshaari, W. Pernice, K. Srinivasan, O. Benson, and V. Zwiller, *Hybrid integrated quantum photonic circuits,* Nature Photonics **14**, 285 (2020).

[84] I. Marinković, M. Drimmer, B. Hensen, and S. Gröblacher, *Hybrid integration of silicon photonic devices on lithium niobate for optomechanical wavelength conversion,* Nano Letters **21**, 529 (2021).

[85] P. R. Scheeper, J. A. Voorthuyzen, W. Olthuis, and P. Bergveld, *Investigation of attractive forces between PECVD silicon nitride microstructures and an oxidized silicon substrate,* Sensors and Actuators A: Physical **30**, 231 (1992).

[86] M. Eichenfield, R. Camacho, J. Chan, K. J. Vahala, and O. Painter, *A picogram- and nanometre-scale photonic-crystal optomechanical cavity,* Nature **459**, 550 (2009).

[87] J. Wang, K. P. Nayak, and J. Keloth, *Photothermal tuning and stabilization of a photonic crystal nanofiber cavity,* Opt. Lett. **44**, 3996 (2019).

[88] X. Jiang and L. Yang, *Optothermal dynamics in whispering-gallery microresonators,* Light: Science & Applications **9**, 24 (2020).

[89] P. R. Saulson, *Thermal noise in mechanical experiments,* Physical Review D **42**, 2437 (1990).

[90] S. A. Fedorov, V. Sudhir, R. Schilling, H. Schütz, D. J. Wilson, and T. J. Kippenberg, *Evidence for structural damping in a high-stress silicon nitride nanobeam and its implications for quantum optomechanics,* Physics Letters A Special Issue in memory of Professor V.B. Braginsky, **382**, 2251 (2018).

[91] Y. Tao, J. M. Boss, B. A. Moores, and C. L. Degen, *Single-crystal diamond nanomechanical resonators with quality factors exceeding one million,* Nature Communications **5**, 3638 (2014).

[92] J. Yang, T. Ono, and M. Esashi, *Surface effects and high quality factors in ultrathin single-crystal silicon cantilevers,* Applied Physics Letters **77**, 3860 (2000).

[93] G. D. Cole, I. Wilson-Rae, K. Werbach, M. R. Vanner, and M. Aspelmeyer, *Phonon-tunnelling dissipation in mechanical resonators,* Nature Communications **2**, 231 (2011).

[94] C. Cartis, J. Fiala, B. Marteau, and L. Roberts, *Improving the flexibility and robustness of model-based derivative-free optimization solvers,* ACM Trans. Math. Softw. **45** (2019), 10.1145/3338517.

[95] O. Černotík and K. Hammerer, *Measurement-induced long-distance entanglement of superconducting qubits using optomechanical transducers,* Phys. Rev. A **94**, 012340 (2016).

[96] G. Arnold, M. Wulf, S. Barzanjeh, E. S. Redchenko, A. Rueda, W. J. Hease, F. Hassani, and J. M. Fink, *Converting microwave and telecom photons with a silicon photonic nanomechanical interface,* Nature Communications **11**, 4460 (2020).

[97] R. Leijssen and E. Verhagen, *Strong optomechanical interactions in a sliced photonic crystal nanobeam,* Scientific Reports **5**, 15974 (2015).

[98] J. T. Muhonen, G. R. La Gala, R. Leijssen, and E. Verhagen, *State Preparation and Tomography of a Nanomechanical Resonator with Fast Light Pulses,* Physical Review Letters **123**, 113601 (2019).

[99] M. R. James, H. I. Nurdin, and I. R. Petersen, *$infty$ Control of Linear Quantum Stochastic Systems,* IEEE Transactions on Automatic Control **53**, 1787 (2008).

[100] M. Yanagisawa, *Quantum Feedback Control for Deterministic Entangled Photon Generation,* Physical Review Letters **97**, 190201 (2006).

[101] R. Hamerly and H. Mabuchi, *Advantages of Coherent Feedback for Cooling Quantum Oscillators,* Physical Review Letters **109**, 173602 (2012).

[102] N. Yamamoto, *Coherent versus Measurement Feedback: Linear Systems Theory for Quantum Information,* Physical Review X **4**, 041029 (2014).

[103] J. Combes, J. Kerckhoff, and M. Sarovar, *The SLH framework for modeling quantum input-output networks,* Advances in Physics: X **2**, 784 (2017).

[104] T. M. Karg, B. Gouraud, P. Treutlein, and K. Hammerer, *Remote Hamiltonian interactions mediated by light,* Physical Review A **99**, 063829 (2019).

[105] A. Harwood, M. Brunelli, and A. Serafini, *Cavity optomechanics assisted by optical coherent feedback,* Physical Review A **103**, 023509 (2021).

[106] J. Li, G. Li, S. Zippilli, D. Vitali, and T. Zhang, *Enhanced entanglement of two different mechanical resonators via coherent feedback,* Physical Review A **95**, 043819 (2017).

[107] Y.-C. Liu, Y.-F. Xiao, X. Luan, Q. Gong, and C. W. Wong, *Coupled cavities for motional ground-state cooling and strong optomechanical coupling,* Physical Review A **91**, 033818 (2015).

[108] J.-S. Feng, L. Tan, H.-Q. Gu, and W.-M. Liu, *Auxiliary-cavity-assisted ground-state cooling of an optically levitated nanosphere in the unresolved-sideband regime,* Physical Review A **96**, 063818 (2017).

[109] J. S. Bennett, L. S. Madsen, M. Baker, H. Rubinsztein-Dunlop, and W. P. Bowen, *Coherent control and feedback cooling in a remotely coupled hybrid atom–optomechanical system,* New Journal of Physics **16**, 083036 (2014).

[110] J. Louisell, *A matrix method for determining the imaginary axis eigenvalues of a delay system,* IEEE Transactions on Automatic Control **46**, 2008 (2001).

[111] G. Teschl, *Ordinary differential equations and dynamical systems*, Graduate Studies in Mathematics No. Volume 140 (American Mathematical Society, 2012).

[112] C. Sommer and C. Genes, *Partial Optomechanical Refrigeration via Multimode Cold-Damping Feedback,* Physical Review Letters **123**, 203605 (2019).

[113] N. Olgac and R. Sipahi, *A practical method for analyzing the stability of neutral type LTI-time delayed systems,* Automatica **40**, 847 (2004).

[114] L. Wu, H. Wang, Q. Yang, Q.-x. Ji, Q.-x. Ji, B. Shen, C. Bao, M. Gao, and K. Vahala, *Greater than one billion Q factor for on-chip microresonators,* Optics Letters **45**, 5129 (2020).

[115] M. W. Puckett, K. Liu, N. Chauhan, Q. Zhao, N. Jin, H. Cheng, J. Wu, R. O. Behunin, P. T. Rakich, K. D. Nelson, and D. J. Blumenthal, *422 Million intrinsic quality factor planar integrated all-waveguide resonator with sub-MHz linewidth,* Nature Communications **12**, 934 (2021).

[116] A. P. Higginbotham, P. S. Burns, M. D. Urmey, R. W. Peterson, N. S. Kampel, B. M. Brubaker, G. Smith, K. W. Lehnert, and C. A. Regal, *Harnessing electro-optic correlations in an efficient mechanical converter,* Nature Physics **14**, 1038 (2018).

[117] C. Sommer, A. Ghosh, and C. Genes, *Multimode cold-damping optomechanics with delayed feedback,* Physical Review Research **2**, 033299 (2020).

[118] U. Delic, M. Reisenbauer, K. Dare, D. Grass, V. Vuletic, N. Kiesel, and M. Aspelmeyer, *Cooling of a levitated nanoparticle to the motional quantum ground state,* Science **367**, 892 (2020).

[119] C. Schäfermeier, H. Kerdoncuff, U. B. Hoff, H. Fu, A. Huck, J. Bilek, G. I. Harris, W. P. Bowen, T. Gehring, and U. L. Andersen, *Quantum enhanced feedback cooling of a mechanical oscillator using nonclassical light,* Nature Communications **7**, 13628 (2016).

[120] A. A. Rakhubovsky and R. Filip, *Robust entanglement with a thermal mechanical oscillator,* Physical Review A **91**, 062317 (2015).

[121] R. Y. Teh, S. Kiesewetter, M. D. Reid, and P. D. Drummond, *Simulation of an optomechanical quantum memory in the nonlinear regime,* Physical Review A **96**, 013854 (2017).

[122] S. Abdalla, S. Ng, P. Barrios, D. Celo, A. Delage, S. El-Mougy, I. Golub, J.-J. He, S. Janz, R. McKinnon, P. Poole, S. Raymond, T. Smy, and B. Syrett, *Carrier injection-based digital optical switch with reconfigurable output waveguide arms,* IEEE Photonics Technology Letters **16**, 1038 (2004).

[123] S. Chen, Y. Shi, S. He, and D. Dai, *Low-loss and broadband 2×2 silicon thermo-optic Mach–Zehnder switch with bent directional couplers,* Optics Letters **41**, 836 (2016).

[124] W. Bogaerts, D. Pérez, J. Capmany, D. A. B. Miller, J. Poon, D. Englund, F. Morichetti, and A. Melloni, *Programmable photonic circuits,* Nature **586**, 207 (2020).

[125] C. Sun, W. Wu, Y. Yu, G. Chen, X. Zhang, X. Chen, D. J. Thomson, and G. T. Reed, *De-multiplexing free on-chip low-loss multimode switch enabling reconfigurable inter-mode and inter-path routing,* Nanophotonics **7**, 1571 (2018).

[126] P. Hyllus and J. Eisert, *Optimal entanglement witnesses for continuous-variable systems,* New Journal of Physics **8**, 51 (2006).

[127] R. Leijssen, G. R. La Gala, L. Freisem, J. T. Muhonen, and E. Verhagen, *Nonlinear cavity optomechanics with nanomechanical thermal fluctuations,* Nature Communications **8**, ncomms16024 (2017).

[128] D. Rosenberg, D. Kim, R. Das, D. Yost, S. Gustavsson, D. Hover, P. Krantz, A. Melville, L. Racz, G. O. Samach, S. J. Weber, F. Yan, J. L. Yoder, A. J. Kerman, and W. D. Oliver, *3D integrated superconducting qubits,* npj Quantum Information **3**, 1 (2017).

[129] D. Høj, F. Wang, W. Gao, U. B. Hoff, O. Sigmund, and U. L. Andersen, *Ultra-coherent nanomechanical resonators based on inverse design,* arXiv:2103.15601 [cond-mat, physics:physics, physics:quant-ph] (2021), arXiv: 2103.15601.

Acknowledgements

The work in this thesis is made possible thanks to the help of many people. At this final part, I would like to express my gratitude to those I have interacted with.

Firstly, I would like to thank my supervisor, Simon Gröblacher. Thank you for accepting me first as a master student and then as a PhD student in the group. It was a great experience learning from you and having other interactions with you. I also really enjoy the nice research environment managed by you, in which I really grow and develop. Besides, I would like to thank Herre van der Zant, my co-promoter. Though we do not have much interaction, I really appreciate your advices and suggestions in our meetings.

I still remember the time when I started my PhD, which was almost four years ago. Richard Norte taught me a lot about device fabrication. It was also really a great effort to test different recipes and enable a reliable fabrication method. On the experimental side, I would like to especially thank João Moura. I have gotten lots of help from you, and I have learned a lot. I would also like to thank Igor Marinković. He was also my daily supervisor in my master project, during which I have learned simulating integrated optical cavities. The skills become important in my PhD work. The knowledge in the simulation, the microfabrication and in the experiment forms the basis of the work.

As time passes, I get more matured and independent in the project. It does not mean that I started to work alone. Rather, I have more and more interaction with other people, and the topics become broderned. At the same time, the size of the group was growing. At this point, it is really impossible to list all the specific helps or contributions from everyone. I would like to thank everyone has been in the group, Andreas Wallucks, Claus Gärtner, Maarten Leeuwenhoek, Moritz Forsch, Clemens Schäfermeier, Robert Stockill, Bas Hensen, Matthijs de Jong, Rodrigo da Silva Benevides, Niccolo Fiaschi, Jie Li, Stefanos Andreou, Amirparsa Zivari, Nina Codreanu, and Yu Zhang. I hope that I have (at least almost) correctly listed your name in the order of the time I met you. Of course I also thank Richard, João and Igor. I really enjoy many interesting and fruitful discussions with you, including the science and many different experimental and microfabrication techniques. Many suggestions have become part of the fabrication or the measurement. I also would like to thank you for buddying me in the cleanroom, and for pulling or help pulling HF fibers. Specifically, I would also acknowledge Igor for initiating the idea of "slapping". Besides, Moritz was my mentor in the cleanroom, though we were working on very different devices. Thank you for your effort in training me in the cleanroom. I would also like to thank Jie for lots of precious discussions about the theories in optomechanics. Also, many thanks to Rob, who also gave lots of useful comments and feedback to this thesis. João, and then Matthijs, work in the same lab as I do. We had lots of interesting discussions, and thank you for keeping the

lab clean, ordered and tidy. There are also many people joining the group at a later state that we have not had much time to interact yet, at this moment. I sincerely wish you all the best in the future, Yong Yu, Alexander Korsch, Liu Chen, Jin Chang, Gaia Da Prato and Xiong Yao.

During this work, I am happy that I have met three master students that I interacted a lot with, Ulderico Filippozzi, Max Drimmer and Isacco Gobbi. I appreciate your efforts related to the work. Ulderico helped with building photodetectors, and Max made lots of contribution to the slapping setup. Isacco helped on further improving the slapping setup, and on expanding our knowledge of an optical cavity with coupling waveguide.

Beyond the group, I would like to thank other people. On the theory side, I have had valuable discussions and collaborations with Corentin Gut. Thank you for your huge efforts and a large amount of time on working on some of our data, while I know that a practical experiment is complicated and no experiment is guaranteed to be succeeded. I also appreciate the discussions with Ralf Riedinger and Sungkun Hong for improving the experimental setup. I also have lots of interesting talks with Andrea Cupertino and Minxing Xu, and I also thank you for buddying me in the cleanroom.

I would also like to thank all the technical and supporting stuffs who guarantee the success of this project, Maria Roodenburg, Tino Kool, Ronald Bode, and all the cleanroom stuffs. I appreciate the tremendous efforts of keeping the building, the labs, and the cleanroom open, at least partially, for research during the COVID-19 pandemic.

During my PhD and, sometime equally or more importantly, before my PhD, I have met a lot more people who lead to the success of the work in the thesis. Though it might be in a more indirect and implicit way, such as education or emotional support, I would like to thank all these people.

Finally, as the most important part, I would like to thank my parents. It is your support, from the very beginning, that enables everything.

In memory of my father.

Curriculum Vitæ

Jingkun GUO

18 October, 1993 — Born in Guangdong, China.

Education

2008–2011 — High school
Shenzhen Second Senior High School, Guangdong, China

2011–2015 — B.Sc. in Electronic and Information Science and Technology
Peking University, Beijing, China
Thesis: Electronic Transport in Semiconductor Nanowires
Promotor: Dr. N. Kang

2015–2017 — M.Sc. in Applied Physics
Delft University of Technology, the Netherlands
Thesis: A study of optomechanics
Promotor: Prof.dr. S. Gröblacher

2017–2021 — Ph.D. in Applied Physics
Delft University of Technology, the Netherlands
Thesis: Bringing classical mechanical resonators towards the quantum regime: A journey on developing integrated optomechanical devices and exploring experiments at high temperature
Promotor: Prof.dr. S. Gröblacher
Prof.dr.ir. H.S.J. van der Zant

List of Publications

7. **J. Guo**, R.A. Norte and S. Gröblacher, *Feedback cooling of a room temperature mechanical oscillator close to its motional groundstate*, Phys. Rev. Lett. **123**, 223602 (2019).

6. J. P. Moura*, R.A. Norte*, **J. Guo**, C. Schäfermeier and S. Gröblacher, *Centimeter-scale suspended photonic crystal mirrors*, Opt. Express **26**, 1895-1909 (2018).

5. **J. Guo**, R.A. Norte and S. Gröblacher, *Integrated optical force sensors using focusing photonic crystal arrays*, Opt. Express **25**, 9196 (2017).

4. L. Sen, G. Huang **J. Guo**, N. Kang, P. Caroff and H. Xu, *Ballistic transport and quantum interference in InSb nanowire devices*, Chinese Phys. B **26**, 027305 (2017).

3. J. Xu, Z. Lei, **J. Guo**, H. Wang, U. Reibetanz and S. Xu, *Trapping and Driving Individual Charged Micro-particles in Fluid with an Electrostatic Device*, Nano-Micro Lett. **8**, 270 (2016).

2. C. Xu*, L. Wang*, Z. Liu, L. Chen, **J. Guo**, N. Kang, X. Ma, H. Cheng and W. Ren, *Large-area high-quality 2D ultrathin Mo2C superconducting crystals*, Nat. Mater. **14**, 1135 (2015).

1. L. Wang, **J. Guo**, N. Kang, D. Pan, S. Li, D. Fan, J. Zhao and H. Xu, *Phase-coherent transport and spin relaxation in InAs nanowires grown by molecule beam epitaxy*, Appl. Phys. Lett. **106**, 173105 (2015).

* These authors contributed equally.